UNIVERSITY OF CALIFORNIA, MERCED

Fiber-based dual-beam optical trapping platform for stretching lipid vesicles

A dissertation submitted in partial satisfaction of the requirements for the degree Doctor of Philosophy

in

Biological Engineering and Small-scale Technologies

by

Tessa Monique Piñón

Committee in charge:

Professor Valerie Leppert, Chair

Professor Jing Xu

Professor Jennifer Lu

2013

The Dissertation of Tessa Monique Piñón is approved, and is acceptable in quality and form for publication on microfilm and electronically:

Chair

University of California, Merced

2013

ACKNOWLEDGMENTS

I would like to express my gratitude for the guidance and support from my research advisors, Dr. Jay Sharping and Dr. Linda Hirst, throughout the course of this project. I would also like to thank all my university friends and labmates for their encouragement and humor through it all. Special thanks to my buddies Alicia, Heather, Ashley, and current and former labmates: Robin Roces, Al Castelli, Jeremy Sanborn, and Kevin Mendoza for helping in the construction and brainstorming in the trapping design; thanks to Nancy Duque for helping with the refractive index measurements; thanks to Pradeep Uppamoochikkal and Kai Lor for their insight with the lipid aspects of the project; Justin Hudjic for the SEM images of heat-etched channels; and Leily Kiani, Thompson Lu, and Christiane Touma for their all-round help, friendship, and lab support.

I also feel so grateful for my family and friends who gave me continuous love and support throughout the difficult times. Much gratitude goes to my father, Robert, my sisters and brother-in-laws, David and Denise Carrejo, and Tony and Jennifer Carrillo, who have all encouraged me and always kept the humor going. Lastly, words cannot explain the amount of encouragement my mother, Alicia, gave until the very end. I know she would be extremely proud.

Also, many thanks to the Chin lab for their laboratory space and use of supplies, University of California, Merced Start-Up funds, and Dr. Hirst's National Science Foundation CAREER (DMR-BMAT #0852791).

Lastly, I would like to thank the United States Navy for supporting me through the last few months of my Doctoral work as an Active Duty Collegiate/Officer Selectee. I look forward to the new adventures and opportunities ahead.

TABLE OF CONTENTS

LIST OF FIGURES

TESSA M. PIÑÓN

EDUCATION

2013	**Ph.D. Candidate**, Biological Engineering & Small-Scale Technologies University of California, Merced
2009	**M.S.** in Biological Engineering & Small-Scale Technologies University of California, Merced Thesis title: "Dual-beam optical fiber trapping platform for biophotonics"
2007	**B.S.** in Physics (Biophysics emphasis); minor in mathematics St. Mary's University, San Antonio, TX

WORK EXPERIENCE

Sept. 2012-Present	**U.S. Navy, Officer Selectee/Active Duty Collegiate,** Surface Warfare (Nuclear Aircraft Carriers)
2007-2013	**Graduate Student Researcher**, University of California, Merced -Actively developing optical fiber trapping setups for lipid vesicle mechanical studies using infrared continuous-wave diode lasers
Winter 2010	**U.S. Department of Defense, Defense Threat Reduction Agency (DTRA)** RD-BA (Basic and Applied Sciences) Directorate, Fort Belvoir, Virginia -STEP student intern
Summer 2006	**Research intern**, University of Washington, Seattle Dept. of Bioengineering, NSF REU Engineered Biomaterials (UWEB) Program -Research involved isolating and characterizing the binding receptor of *Staphylococcus epidermidis*, an opportunistic pathogen
Summer 2005	**Research intern**, University of California, San Francisco Dept. of Cellular and Molecular Pharmacology, Summer Research Training Program -Investigation entailed studying nucleation kinetics of *Drosophila* Spir, an actin nucleator involved in cell motility
Summer 2004	**Research intern**, Texas A&M University, College Station Dept. of Biochemistry and Biophysics, student internship program sponsored by Office of Naval Research (ONR) -Experimental work involved understanding roles and timing mechanisms of phage lambda holing and anti-holin in promoting *E.coli* bacterial cell lysis

TEACHING EXPERIENCE

Fall & Spr. 2012	Teaching Assistant, Physics: kinematics for biology undergraduate majors
Fall 2011	Teaching Assistant, Introductory Biology laboratory for undergraduates
Fall 2009	Teaching Assistant, "Introduction to Scientific Data Analysis," undergraduate course
2007-2009	Teaching Assistant, Physics: kinematics and electromagnetism undergraduate courses

ACADEMIC AWARDS

2008	**Alternate candidate,** Ford Diversity Predoctoral Fellowship
2007	**Presidential Award**, St. Mary's University -Faculty-selected distinguished graduating senior of undergraduate class for outstanding leadership and service
2006	**Scholarship**, Armed Forces Communications and Electronics Association, San Antonio Alamo Chapter
2005	**Conference travel grant**, American Biomedical Research Conference for Minority Students (ABRCMS), Atlanta, GA.

PATENT

2011	Sharping, Jay E. and **Tessa M. Piñón**. Optical-fiber based light force particle trapping and microfluidic apparatus, system and method. U.S. Provisional patent application filed April 8, 2011. U.S. Patent Application Serial No.: 61/472,336. Assignee: Regents of the University of California (Oakland, CA).

PUBLICATIONS

Piñón, TM, A Castelli, LS Hirst, JE Sharping (*in review*). "A Fiber-Optic Trap-on-a-Chip Platform for Probing Low Refractive Index Contrast Biomaterials." Applied Optics.

Piñón, TM, LS Hirst, JE Sharping (2012). "Optical Trapping and Stretching of Lipid Vesicles." CLEO: Applications and Technology. p. ATh1M.4

Piñón, TM, LS Hirst, JE Sharping (2011). "Fiber-based dual-beam optical trapping system for studying lipid vesicle mechanics." Optical Society of America (OSA): Optical Trapping Applications, p. OTTuB2.

Piñón, TM, K Katzenmeyer, J Callihan, and JD Bryers (2008). "Expression, Purification and Characterization of a Recombinant *Staphylococcus epidermidis* Fibronectin-Binding Protein." University of Washington, Seattle. Journal of Undergraduate Research in Bioengineering (JURIBE).

SEMINAR PRESENTATION

-Piñón, T. (2011, Oct.). *Why Do Giant Unilamellar Vesicles Wait Before Being Stretched?*, Brown Bag Lunch seminar talk, School of Natural Sciences, University of California, Merced.

CONFERENCE PRESENTATIONS

-Piñón, T. (2012, May.). *Dual-Beam Optical Fiber Trapping System for Studying Lipid Vesicle Mechanics*. Poster presentation, Biophotonics Summer School, University of Illinois, Urbana-Champaign.

-Piñón, T. (2012, Jan.). *Dual-Beam Optical Fiber Trapping System for Studying Lipid Vesicle Mechanics*. Poster presentation, Biophotonics Industry Forum: Center for Biophotonics Science & Technology (CBST), University of California, San Francisco.

-Piñón, T. (2011, July). *Dual-Beam Optical Fiber Trapping System for Studying Lipid Vesicle Mechanics*. Poster presentation, Center for Biophotonics Science & Technology (CBST) retreat. Lake Tahoe, CA.

-Piñón, T. (2011, Apr.). *Fiber-Based Dual-Beam Optical Trapping System for Studying Lipid Vesicle Mechanics*. Oral presentation. Optical Society of America (OSA): Optical Trapping Applications conference, Monterey, CA.

-Piñón, T. (2011, Mar.). *Studies of Lipid Vesicle Mechanics Using an Optical Fiber Dual-Beam Trap*. Oral presentation, American Physical Society (APS) March Meeting, Dallas, TX.

-Piñón, T. (2010, June). *Dual-beam Optical Fiber Trapping System for Studying Lipid Vesicle Mechanics*. Oral presentation, UC Systemwide Bioengineering Symposium. University of California, Davis.

-Piñón, T. (2010, April). *Dual-beam Optical Fiber Trapping System for Studying Lipid Vesicle Mechanics.*Poster presentation, Research week at University of California, Merced.

-Piñón, T. (2009, July). *Dual-Beam Optical Fiber Trapping Platform for Biophotonics Applications*. Poster presentation, Center for Biophotonics Science & Technology (CBST) retreat. Lake Tahoe, CA.

-Piñón, T. (2005, Nov). Identifying *Regions of Drosophila Spir Essential for Actin Nucleation*. Poster presentation at national Annual Biomedical Research Conference for Minority Students (ABRCMS). Atlanta, GA.

-Piñón, T. (2004, Nov). *Tracking Phage Lambda Holin Behavior with Cysteine Mutagenesis.* Oral presentation given at national Annual Biomedical Research Conference for Minority Students (ABRCMS). Dallas, TX.

SUMMER INSTITUTE

4th Biophotonics Summer School, University of Illinois, Urbana-Champaign, May 21-June 1, 2012.

PROFESSIONAL MEMBERSHIPS

Optical Society of America
American Physical Society

ABSTRACT

Fiber-based dual-beam optical trapping platform for stretching lipid vesicles
Tessa Monique Piñón,
Co-advised by Professor Linda S. Hirst and Professor Jay Sharping

Submitted in partial satisfaction of the requirements for the degree Doctor of Philosophy
Biological Engineering and Small-scale Technologies,
University of California, Merced

Dual-beam fiber trapping is a versatile technique for manipulating micron-sized particles, biological assemblies, and living cells. Here, we fabricate fiber-based trapping platforms from plexiglass chips of polycarbonate and cast acrylic. Single-mode fibers from 980 nm fiber-pigtailed laser diodes are arranged in a counter-propagating configuration and situated into alignment. Fiber alignment is verified via coupling efficiency experiments whereby measured efficiency profiles assure proper alignment for trapping.

The initial stages of this project involved fabrication and testing of these trapping platforms. We calibrate the range of forces exerted on trapped polystyrene microspheres in water by suddenly offsetting one of the laser power outputs. The sudden offset causes a trapped microsphere to undergo a small displacement from the trap center. The displaced particle as a function of time follows a characteristic curve of over-damped harmonic motion. We then extrapolate the related spring constants which is proportional to the scattering force acting along the beam axis. Measured spring constants are in the range of 104-145 nN/m which are in agreement with expected values.

Subsequently, we demonstrate for the first time, stable trapping and stretching of low contrast giant lipid vesicles in solution. Trapped vesicles encapsulate poly(ethylene) glycol solution and are trapped with femtonewton range forces. We analyze the lipid membrane response to a range of optical stresses that initiate membrane stretching. At increasingly higher powers, we observe elongation of a vesicle along the beam axis (vesicle major axis) and contraction in the transverse direction (vesicle minor axis). The peak stress exerted along the beam axis is calculated for each incident power. Lipid vesicles stretch in a linear fashion for relative deformations up to 25%, correlating to applied peak stresses ranging from 7-60 mN/m^2. Nonlinear deformations are observed at even higher applied optical stress. These experiments demonstrate the capabilities for trapping a variety of low-contrast, soft biomaterials.

CHAPTER 1

Introduction

1.1 Advancements in Optical Trapping

The technique of optical trapping has advanced during the past four decades, and a few different optical trap configurations have been actualized during this time period. In 1970 Arthur Ashkin demonstrates the first single, focused optical trap and a dual beam optical trap comprised of two opposing laser beams focused with lenses [Ashkin 1970]. Ashkin reports successful trapping of latex microspheres in water within a glass cell, in addition to particles trapped in a gas. Suspended microspheres around the trapping region were reported to be drawn in, then accelerated to a stable equilibrium point, eventually coming to rest. This radiation pressure exerted from laser light induces mechanical forces acting on a freely suspended dielectric micro-particle in air, and even water [Ashkin 1986]. In general, a higher index ratio for the particle's interior refractive index to exterior medium (e.g. water) index yields better trap stability. Ashkin's successful trapping and initial observations have greatly motivated fundamental insights about radiation pressure in solid and liquid dielectrics [Ashkin 1973] and the presence of stable electrical potential wells in the trapping region, which have implications ranging from atomic trapping [Ashkin 1970, Ashkin 1986] to biological uses [Ashkin 1986, Ashkin 1987].

Since Ashkin's first realization of a single optical tweezer beam and two focused beams for trapping micron-sized particles, other research groups have expanded upon these initial works. A couple decades later, Constable, *et al.* demonstrate the first dual-beam optical fiber trapping set-up comprised of two well-aligned, opposing fibers with diverging Gaussian beams exiting the fiber ends [Constable 1993]. Polystyrene microspheres of diameters ranging from 0.1 μm to 10 μm were trapped using single-mode fibers aligned and assembled using simple, inexpensive laboratory materials. Their trapping configuration utilizes two pigtailed diode lasers, one of wavelength 1.3 μm and the other with wavelength 0.831 μm [Constable 1993]. Depictions of the trapping configurations discussed above are shown in Figure 1.1.

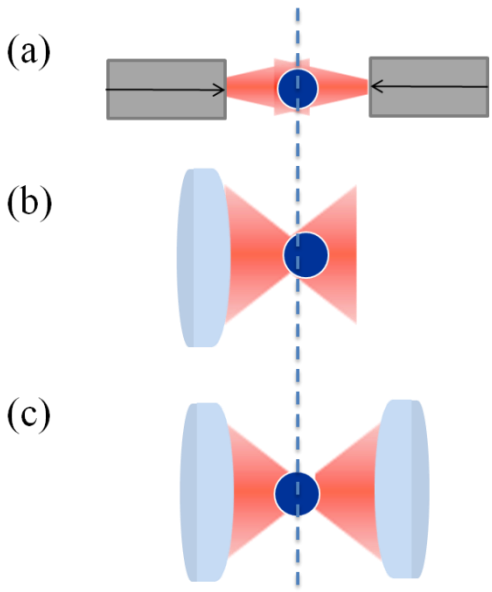

Fig. 1.1 Schematic of the three most common types of optical traps. (a) Dual-beam optical fiber trap with overlapping diverging Gaussian beams emerging from the counter-propagating fibers. The trapped particle sits in the center of the trapping region (denoted by the dotted line). (b) Typical optical tweezer (single beam trap) with a very tightly focused beam. The beam waist is the region of strongest intensity and a high gradient force. A trapped particle sits slightly away from the beam waist due to the scattering force in direction of beam propagation. (c) Dual-beam focused trap with two opposing beams that are tightly focused. The trapped particle sits in the beam waist. (Illustrations drawn by T. Piñón)

More recent studies with the fiber dual-beam have explored the dynamics of trapped microspheres that analyze the transverse and axial trapping force efficiencies and stability [Sidick 1997]. Other research groups have devised mathematical models that explain optical interactions when several particles are trapped simultaneously. For a dual-beam Gaussian trap, self-organization of particles have been observed when particles are situated in a linear array between two opposing optical fibers, as well as a spontaneous onset of oscillations for a critical number of polystyrene microspheres [Gordon 2008].

One additional physical phenomena that has been explored include particle self-sustained particle oscillation when the counterpropagating trapping fibers are slightly misaligned in the transverse direction [Gordon 2008 and Kawano 2008]. Observations of such particle oscillations are shown in my Master's thesis [Pinon 2009]. In short, transversely misaligned beams cause incident optical forces to impart a torque about the center of the object. Similar optically-controlled rotation within a fiber dual-beam optical trap has also been applied to biology, with demonstrated rotation and translation of trapped smooth muscle cells [Black 2012] and human red blood cells, leukemia cells, and

clusters of human epithelial cancer cells [Kreysing 2008]. These and other applications of dual-beam trapping in biomedical research have implications in tomographic microscopy.

1.2 The Dual-Beam Trap as an "Optical Stretcher" and "Optical Squeezer"

Unlike other deformation-inducing techniques that locally deform biological materials to extract viscoelastic behavior, the dual-beam trap has the advantage of trapping (and stretching) the entire volume of a biological cell, or as demonstrated in this Dissertation, artificial spherical lipid vesicles. Thus, the fiber-based dual-beam trap was coined as the "Optical Stretcher" by Jochen Guck [Guck 2000, Guck 2001]. With increased incident trapping power, the bulk volume of the trapped soft dielectric, cell, or vesicle experiences stress forces that are normal to a given surface element [Guck 2001, Guck 2005, Bareil 2006, Bareil 2007, Ekpenyong 2009]. The optical forces acting on a trapped particle depend on the refractive index contrast between the particle and the exterior solution [Guck 2001, Ichikawa 2001]. In general, a higher index ratio for the particle's interior refractive index to exterior medium index yields better trap stability. Dual-beam traps, it turns out, can produce deforming stresses up to 400 times greater than optical tweezers, with significantly lower light intensity due to unfocused beams [Guck 2000]. These aspects of the dual-beam trap offer significant advantages for trapping biological entities sensitive to local heating.

An interesting variation of the "Optical Stretcher" is the "Optical Squeezer." In comparison to the more conventional "Optical Stretcher," the "Optical Squeezer" stably traps low refractive index ultrasound contrast agent microbubbles using annular-shaped trapping beams [Skelton 2012 and Skelton 2012]. Skelton, *et al.* [2012] observed optical stress-induced *inward deformations* ("squeezing") of the microbubble whereby the elastic properties of the shell material can be quantified.

1.3 The Fiber-Based Dual-Beam Trap as a Tool in Biology

Much attention has been drawn to the vast biological applications of fiber-based optical trapping for single-cells due to the large non contact trapping area that makes this technique ideal for probing a single biological cell or even a small cell aggregate [Guck 2000, Guck 2001,Guck 2005]. Fiber-based dual-beam trapping configurations offer distinguishable advantages in comparison to other optical trapping techniques such as optical tweezers. In contrast to optical tweezers, dual-beam traps consist of both scattering and gradient optical forces to manipulate the entire volume of a particle. Additionally, since optical tweezers trap with a three-dimensional gradient force, one must use a tightly focused beam which results in increased optical intensity in the trapping region. Optical forces can be hundreds of times greater in dual-beam configurations than optical tweezers with significantly lower light intensity [Guck 2000].

Fiber traps are also appealing for integration with microfluidic flow channels within a small fabricated chip whereby the enclosed microfluidic environment can be

carefully controlled. One methodology that may be coupled with dual-beam trapping includes Raman spectroscopy in which microfluidic systems may pass cells through the trap region for optical spectra analysis [Jess 2006 and Jess 2007]. This technique is potentially useful for medical diagnostics by attaining Raman spectra ("biochemical fingerprints") from a population of assorted normal and tumour cell lines fairly rapidly and without the need for a cell marker or any mechanical attachment [Jess 2007]. The potential of high cellular throughput suggests the ability to effectively sort cells into desirable microfluidic channels after cellular analysis [Lincoln 2004, Lincoln 2007, and other Lincoln 2007, Cran-McGreehin 2006].

Most notably, the fiber-based dual-beam trap has been used in biology as a label-free technique for identifying bulk cellular cytoskeletal changes which could be indicative of malignant changes [Guck 2005, Remmerbach 2009]. While the majority of cellular research has focused on biochemical mechanisms governing many biological processes, much less is known about the role of cell mechanical properties that play a role in cell migration and cell differentiation [Lautenschlager 2009 and Titushkin 2007].

The technique of dual-beam trapping has shown promise for mechanically phenotyping individual cells for the goal of faster, targeted screening processes. These trapping experiments have been applied to biomedical diagnostics by stretching red blood cells [Guck 2001, Bareil 2006, Bareil 2007, Ekpenyong 2009], murine fibroblasts [Guck 2001 and Guck 2005], human breast epithelial cells [Guck 2005], murine osteogenic cells [Ekpenyong 2009], and oral squamous cell carcinomas [Remmerbach 2009] along the beam axis. Interestingly, malignant cell lines showed significantly different mechanical behavior from their healthy counterparts. For example, malignant oral squamous cells were found to be more easily deformable, by a 3-fold deformability measure [Remmerbach 2009]. These cellular mechanical changes are attributed to a change in the cytoskeleton from an ordered and stiff structure to a more irregular, less rigid conformation [Remmerbach 2009].

Other research groups have taken strides for devising user-friendly and inexpensive lab-on-a-chip [Lee 2010] analysis devices that integrate optical trapping for cell sorting [Grover 2001, Eriksson 2010]. Bellini, *et al.*, [2010] report on their fabrication of an integrated dual-beam trap and fused silica glass optofluidic chip for single cell analysis by stretching red blood cells. Such lab-on-a-chip devices have the advantage of maintaining stable fiber alignment once the fibers are fixed within the chip channel, and can be further modified for more advanced sensing and automated sorting functions.

1.4 Surveying Elastic Properties of Soft Biomaterials

A variety of methods have been employed to measure mechanical responses of lipid vesicles, including focused-beam optical tweezers systems [Shitamichi 2009, Ichikawa 2001, Bendix 2011]. Additionally, the work of Cherney, *et al.* [2004] investigates the influence of laser tweezer forces on unilamellar vesicles and integrated

the use of confocal Raman microscopy [Cherney 2004]. Cherney, *et al.* [2004] demonstrate the use of milliwatt trapping laser power to deform membranes from its original spherical shape and evaluate the trapping energy and forces associated with the tweezed lipid membrane and the solution external to the vesicle.

Another technique, atomic force microscopy can provide information about local viscoelasticity of cells [A-Hassan 1998], but may resultant force curves may include artifacts from extra soft samples such as lipid bilayers. Additional point-methods that have been applied to cell-sized lipid vesicles (≈10 μm) are micropipette aspiration [Fygenson 1997, Evans 1987, Needham 2000].

Unique to the techniques discussed above, fiber-based dual-beam optical trapping affords a non-invasive method for surveying a range of applied forces applied to the lipid membrane without the need for bulky optical systems or incorporation of latex beads as is the case for optical tweezer-based lipid membrane tethering. Dual-beam trapping provides sufficient sensitivity to probe the large response function of lipid membranes. To our knowledge, our use of fiber dual-beam trapping for optically holding and stretching the entire volume of lipid vesicles is the first of its kind. Another group, Solmaz [2012], has since also demonstrated optical stretching of GUVs with a fiber-based dual-beam trap. The dual-beam trap is a suitable tool for meeting the continual need of developing methods that can apply various stresses on biological entities in a controlled and precise fashion, especially for delicate, soft biomaterials such as lipid vesicles.

1.5 Implications for Isolating Lipid Vesicle Mechanical Properties

The lipid bilayer is the most basic permeability barrier that confines a biological cell, separating the cell from its exterior environment and compartmentalizes organelles from the cytoplasm. The lipid bilayer is fundamental in many intra- and intercellular signaling processes [Dopico 2007 and Voet 2006]. Vesiculation and budded tubules serve as trafficking compartments that transfer cellular cargo from donor vesicle and can fuse with neighboring vesicles [McMahon 2005]. Since the lipid bilayer is a key component of a membrane, cell-sized artificial giant unilamellar vesicles (GUVs) serve as good models for investigating cell membrane shape dynamics from a physical perspective [Luisi 2000].

In this project, our focus centers on the deformation behavior of artificial lipid vesicles in response to optical stress from a dual-beam trap. We aim to gain insight into the mechanical dynamics of the cellular membrane by optically characterizing these fluid lipid bilayers via optical stretching. The use of artificial biomembranes permits one to isolate mechanical contributions from the lipid membrane in the absence of other cellular components such as organelles and the cytoskeleton, which is a mechanically stiff and dynamic structure. Physical theories have been developed to describe a range of membrane conformations that have an essential role in cellular processes including endocytosis, exocytosis, and cytokinesis and that depend on mechanical properties of the membrane [Svetina 2002, McMahon 2005, Lipowsky 1991]. It is known that

asymmetries in the bilayer can result in spontaneous curvatures of vesicles that conform into ellipsoids, discoids, pear-shapes, cup-shapes, and buds [Markvoort 2006].

One future goal for this thesis project is to investigate how optical deformation of artificial giant unilamellar vesicles (GUVs) could provide more quantitative insights into more complex molecular mechanisms [Phillips 2009].While simple vesicles lack the complex structural networks and organelles of biological cells, they can be adapted to incorporate entities of native cells such as voltage-gated ion channel proteins [Reeves 2008] or be engineered to contain a mixture of raft-forming lipids [Hirst 2011, Baumgart 2005]. Glass injection micropipets could be used to incorporate very small volumes of reagents such as salts, detergents, or polymers in or on giant vesicles [Menger 1998].

Furthermore, emerging biological research suggests the lipid membrane itself plays a surprisingly active role in cellular functions due to membrane conformation changes [Phillips 2009]. Elucidating fundamental lipid membrane mechanical properties could ultimately lead to better understanding the role between complex protein-membrane mediated conformations, interactions, and proper cellular function [Phillips 2009 and McMahon 2005]. One unique example of the interplay between lipid properties and protein function includes "force-sensing" mechanosensitive channels that perceive membrane tension and respond to applied tension by opening nanoscale protein pores [Haswell 2011]. Variations in lipid membrane thickness or entities that induce membrane curvature directly impact the tension necessary for opening or gating mechanosensitive channels [Haswell 2011]. Nevertheless, one study highlights that protein-free synthetic vesicles may still undergo budding and vesicle fission that are driven by spontaneous membrane curvature [Dobereiner 1993] coupled to local lipid composition [Baumgart 2005]. The study of Dobereiner, *et al.* [1993] was one of the earliest that provided evidence for physical mechanisms of the lipid bilayer that drive the creation of budding and fission [Dobereiner 1993].

1.6 Relevance of Biomembrane Shape Conformations

From a physical point of view, it has been of interest to realize several deformation-inducing techniques for probing membrane viscoelastic behavior. Such methods include micropipette aspiration, in which the membrane is pulled with suction [Dimova 2006], and atomic force microscopy techniques that locally indent the cell membrane. Additionally, optical tweezer systems have been used to probe the mechanical properties of artificial GUVs relating applied force to extension curves. Tweezer-driven systems trap one or more beads within the vesicle and optically maneuver them such that the membrane is stretched outward as a long protrusion [Shitamichi 2009 and Fygenson 1997], mimicking the tubular shapes of neurons, cellular protrusions, or other membrane conformational changes relevant to cellular processes [Fygenson 1997, Svetina 2002]. Membrane deformation is observed in membrane trafficking [Lee 2008], with internal cargo macromolecules that may bud or form tubules that eventually detach from the membrane surface [Sens 2008].

Additional studies have moved past qualitative explorations of membrane morphologies, and have aimed for qualitative analysis of the thermal energy costs associated with driving a specific configuration [Bar-Ziv 1998, Markvoort 2006, Dobereiner 1997, Miao 1994]. The elastic behavior of closed membranes may not only be mimicked with deformation methods, but it has been demonstrated that external forces applied such as tension, pressure, and spontaneous curvature can be accurately computed from the induced shape transformation with optical tweezers [Lee 2008]. Another experiment involving exerting tension on vesicles using optical tweezers have shown that light-force interactions can induce pearling shape transitions of the vesicle [Bar-Ziv 1998].

1.7 The Fabrication and Application of a Trapping Platform

My Master's thesis [Pinon 2009] motivated further research for realizing a fully functional fiber trap system for trapping single lipid vesicles on a low-cost trapping platform reported in this Dissertation. After fabrication of trapping platform prototypes, the performance of each prototype was evaluated to understand trapping mechanics, and design improvements continued so that stable and efficient trapping were achieved. Subsequent studies aimed to characterize trapping forces of the system to evaluate the range of incident optical forces for latter experiments. System calibrations were conducted by trapping dielectric micron-sized polystyrene beads to note the amount of control over the trapping forces as well as assess the amount of noise in the dual-beam trapping system. These preliminary steps were fundamental to complete before we characterized mechanical responses of optically stretched lipid vesicles to be discussed in the proceeding Chapter 4.

This project explores femtonewton trapping forces for low refractive index contrast vesicles, which is an order of magnitude less than the more prevalently studied piconewton forces arising from trapping higher contrast particles. Stable trapping of vesicles encapsulating poly(ethylene glycol) polymer solution is observed with trapping forces as low as 15 fN. The applied optical stress results in vesicle deformations, such as stretching, which occurs with increased incident trapping power. We note that vesicle deformations exhibit ranges of linear and non-linear responses for applied peak stresses of ~7-60 mN/m^2. Our studies provide a foundation for exploring the dynamics of trapped lipid vesicles undergoing shape transformations such as budding and vesiculation.

CHAPTER 2

Optical Trapping System Design and Calibration Measurements

2.1 Introduction

This project describes the fabrication and particle trapping performance of our dual-beam scheme. In this configuration two cleaved, well-aligned single-mode fibers are situated in a counter-propagating fashion with a small gap between the fiber ends (the trapping region). Particles are trapped by a combination of scattering and gradient forces from a near-infrared 974 nm laser. Excellent alignment of fibers is essential for stable performance.

We aim to fabricate a fiber-optic based trapping system on plexiglass chips of polycarbonate and cast acrylic. A current trend in microfluidics is leaning toward flexible and rapid processing techniques for low-cost integrated chips. Our open faced trap-on-a-platform chips permit imaging of trapped micro-particles in real time with common-use microscopy systems.

Here, three fiber trapping configurations are described, highlighting the different methods for fiber alignment and trapping. The first trapping scheme involves a free-space design in which fibers are aligned with micrometer stages; the second scheme of a compact plexiglass chip with a machine-milled wedge groove for aligning the fibers within the channel and using "guide-fibers." An alternative method to the machine-milled wedge groove chip is a heat-etched channel fabrication method that was first employed in earlier developments of this trapping project exhibited in my Master's thesis [Pinon 2009].

Extensions of these initial experiments involving optical trapping polystyrene microspheres include trapping low-refractive index contrast lipid vesicles. Thus, we first set out to quantify the performance of the fiber-pair trapping system by trapping polystyrene microspheres. A trapped bead may be displaced from the center of the trapping region when one laser power is suddenly increased (or decreased). Tracking the motion of displaced beads suspended in water permits us to characterize trapping forces and relative spring constants. A thorough understanding of these fundamental trapping forces is critical for quantifying the behavior of trapped and stretched single vesicles to be discussed in later in Chapter 4.

2.2 Basic Trapping Theory

The dual-beam trapping configuration consists of two opposing single-mode optical fibers. The emerging beams exhibit a Gaussian profile, such that the light from each fiber diverges at angle θ with increased distance from the beam waist, ω_o, where Z is the distance from the fiber end [Hecht 2002]. As shown in Fig 2.1, the Rayleigh range, Z_R, is defined as the distance along a propagating Gaussian beam where the radius increases by a factor of $\sqrt{2}$ and the beam cross-sectional area is doubled [Hecht 2002].

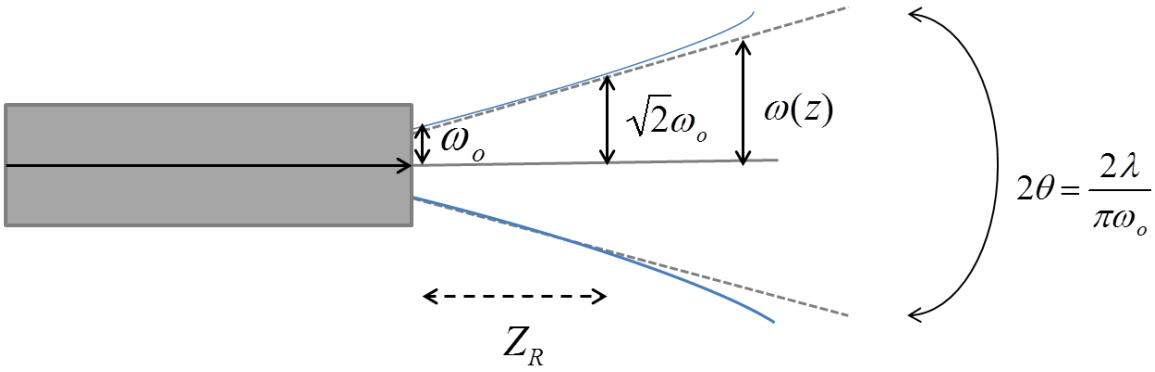

Fig 2.1 Illustration depicting a Gaussian laser beam emerging from an optical fiber. The beam exits the single-mode fiber with wavelength λ propagating along the z-axis. The beam diverges with angle θ along the beam path. The transverse direction from the z-axis has a Gaussian intensity gradient profile, with the greatest intensity *I(r)* occurring at the beam waist, ω_o, the initial point at which the beam emerges from the fiber tip. (Illustration drawn by T. Piñón)

The optical trapping technique utilizes radiation pressure from one or more focused laser beams on a microscopic particle (typical diameter range ≈ 4-18 μm) [Ashkin 1987, Constable 1993]. Here, we demonstrate a fiber-based laser trap, as depicted in Figure 2.2, comprised of two, well-aligned single mode fibers. A small gap between the fibers provided an optical trapping region, where the two diverging beams overlap. This type of optical trap exerts two categories of forces upon trapped objects such as dielectric spheres or biological cells [Ashkin 1987, Constable 1993, Grover 2001, Guck 2005, Lincoln 2007].

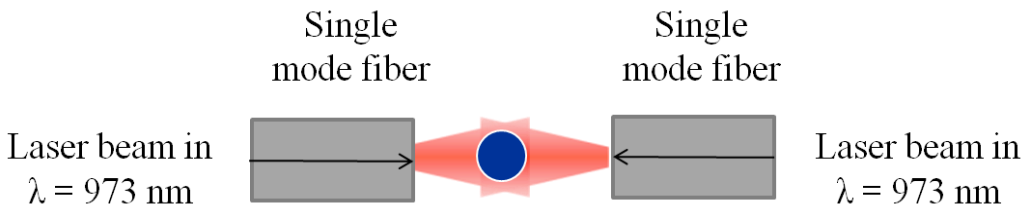

Fig 2.2. Illustration of the basic dual-beam trap configuration consisting of two counter-propagating divergent laser beams (λ = 974 nm). The two beams overlap within a small space between the opposing beams (not drawn to scale). This region of beam overlap provides a stable trapping region for micron-sized particles. (Illustration drawn by T. Piñón)

We utilize single-mode fibers for wavelengths of 980 nm (compatible with the trapping wavelength) with a mode field radius of 2.1 μm and numerical aperture of 0.21, as per manufacturing specifications (Fiber Instrument Sales). For a simulated trap in pure water and a fiber separation of 40 μm, each beam has a radius of ≈3.2 μm, yielding a trapping area approximately 32 μm^2. Yet at a fiber separation of 125 μm, each beam has a radius of ≈10 μm, with a trapping area about 314 μm^2. This suggests an approximate 10 fold increase of trapping area, meaning the trap can potentially hold larger particles since incident light will encompass most of the particle's surface area. Figure 2.3 models the two diverging and overlapping beams, showing beam profiles in air in comparison to water. As expected, beam divergence is larger when in air rather than in water.

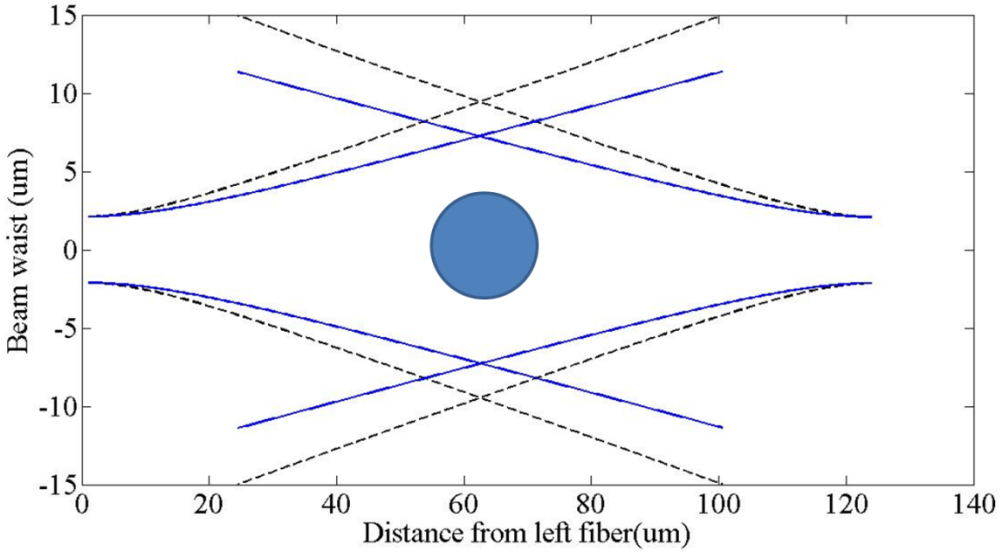

Fig 2.3. Depiction of trapping region comprised of two divergent, overlapping beams (left and right) for a fiber separation of 125 μm using HI980 fibers with ω_o = 2.1 μm. The beams overlap at ~62.5 μm (the distance from the left fiber tip), constituting the position for a stably trapped particle (here, illustrated particle diameter ≈ 6 μm). (Dotted black): beam boundaries in air (n = 1); (solid blue): beam boundaries in water ($n_{measured}$ ≈ 1.327, Chapter 3). (Matlab plot by T. Piñón)

Stably trapped particles are trapped with a combination of two optical forces: scattering forces and gradient forces (Figure 2.4). The *scattering force* acts in the direction of beam propagation, pushing the particle away from the light source. The scattering force arises from reflection off the surface of the trapped object, yielding a change in momentum of photons incident on the particle surface. [Constable 1993, Grover 2001, Guck 2005, Kawano 2008]. The *gradient force* is the other force acting on a trapped object and arises from refraction through the dielectric micro-particle. The gradient force acts in the radial direction of the Gaussian trap beams [Constable 1993, Grover 2001, Guck 2005, Kawano 2008], and has a tendency to pull the particle towards the region of higher beam intensity [Constable 1993, Guck 2005].

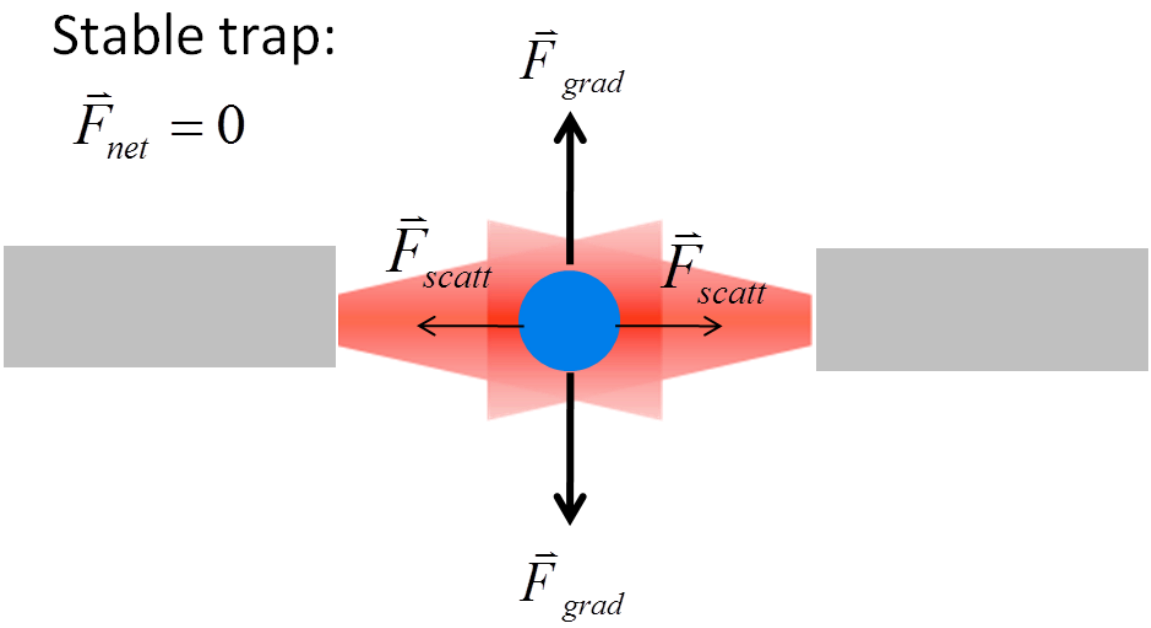

Fig 2.4. Schematic showing the scattering and gradient forces acting on a stably trapped spherical particle. The opposing scattering and gradient forces cancel one another at the trap center, yielding $F_{net} = 0$ for a stably trapped particle. (Illustration drawn by T. Piñón)

The gradient force is proportional to the Gaussian beam intensity gradient in the electric field [Ashkin 1986]. The net gradient force is of greater magnitude than scattering forces [Lincoln 2007]. Unlike the scattering force, gradient forces are additive, whereas the opposing scattering forces cancel one another for a stable trap [Lincoln 2007].

Photons with a given momentum are refracted through the dielectric object with an optical index of refraction greater than that of the exterior medium [Guck 2005]. For this reason, a polystyrene microsphere (of refractive index $n \approx 1.58$) trapped in water ($n = 1.327$), acts as a focusing lens for the incident beams [Ashkin 1970]. This change of momentum in the refracted photon path causes an equal and opposite change in the object's momentum, imparting a force equal to the net rate of change of momentum of refracted photons [Guck 2005]. Thus, as shown in Figure 2.5, the trapping forces at play impart both "pushing" (scattering force) and "pulling" (gradient) forces, resulting in the net effect of a stable trapping region in the center of the two opposing laser beams. A slightly displaced particle will experience a restoring force back to the trap center due to the electromagnetic gradient nature of the beams.

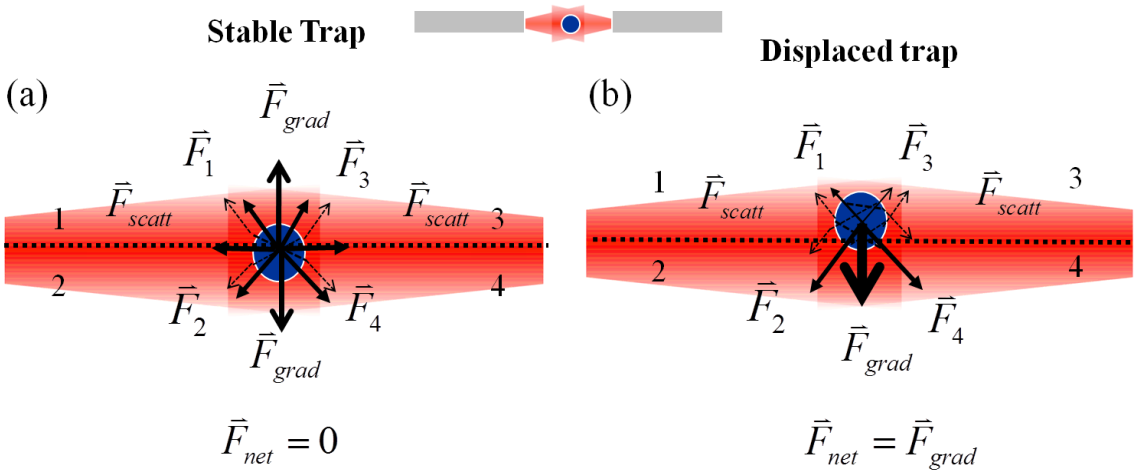

Fig 2.5. (a) Illustration of two Gaussian, divergent beams of the dual-beam trap exhibiting an intensity gradient in the radial direction from the beam waist. For a trapped particle with a refractive index contrast (relative to exterior medium), the momentum of incident photons changes when optical rays are refracted through the particle and reflected from the particle surface. These photon-particle interactions give rise to and $F_{gradient}$ and $F_{scattering}$, respectively. A stable trap is achieved when the sum of all incident forces equals zero (F_{net} = 0) and when small displacements lead to a restoring force. (b) In the case of a trapped bead pulled away from the trap center, by conservation of momentum, $F_{gradient}$, pulls the bead back to the trap center. Thus, the bead experiences a change in the magnitude of its momentum, rebounding in the opposite direction to the trap center. (Illustrations drawn by T. Piñón)

Shown in Figure 2.6 is a force quiver plot that illustrates relative magnitudes for scattering force vectors in the trapping vicinity (gradient force vectors not shown). It is interesting to note the “pushing” trajectory that is strongest near the fiber core, with the scattering force readily dropping off at increased distance away from each fiber. When the net scattering (and gradient force) equal zero, the trapped particle sits at an equilibrium point in the trap center.

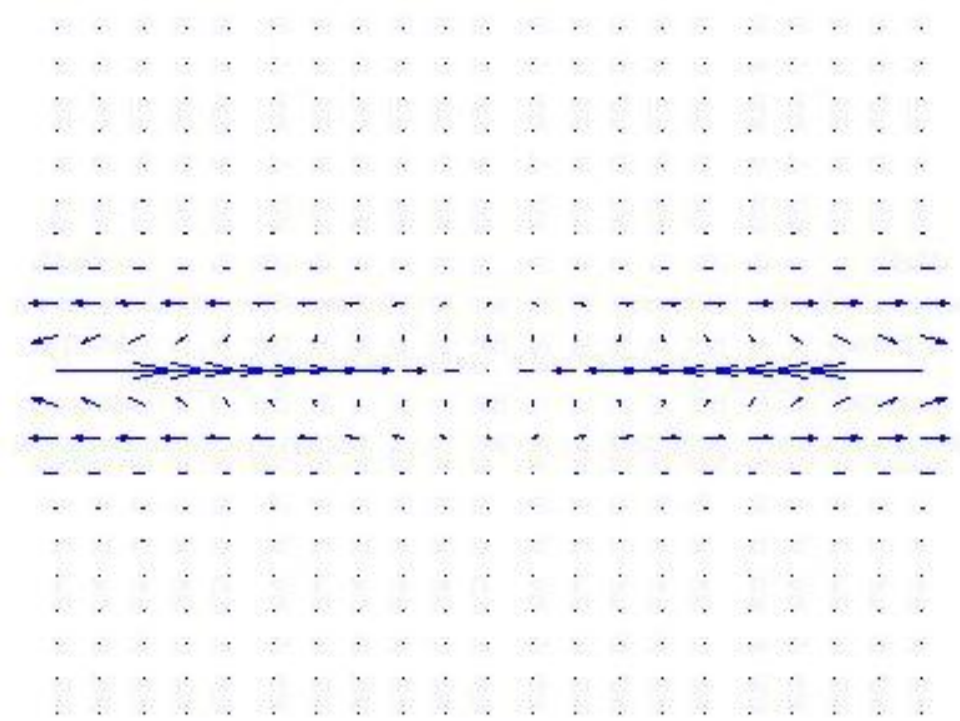

Fig 2.6. Force quiver plot depicting relative scattering force magnitudes near the optical trapping region. Optical fibers (not illustrated) are incident from left and right sides of the simulation. Parameters here simulate the refractive index contrast of a polystyrene microsphere in water, balanced laser powers of 50 mW, and fiber separation of 100 μm. (Matlab plot by J. Sharping)

2.3 Scattering Phenomena

Here we discuss a qualitative explanation for scattering theory in the optical trap. An incident electromagnetic field incident on a dielectric particle (e.g. polystyrene microsphere, lipid vesicle, or biological cell) excites electric dipole moments, giving rise to electronic polarizability [Bohren and Huffman 2004, Thomas 2006]. These dipole moments oscillate at an equivalent frequency of the incident electromagnetic field, and emit secondary radiation wavelets in all directions (all angles of θ) [Bohren and Huffman 2004]. In this process, emitted wavelets undergo phase shift behavior that is influenced by parameters such as particle material, size and shape, as well as scattering direction. The spherical symmetry of a polystyrene sphere infers the scattered field is independent of incident light polarization state [Bohren and Huffman 2004].

In the early 1900s, the first analyses detailing absorption and scattering theory by small spherical particles were carried out, with several scientists working on this problem: Gustav Mie, Lorenz, and Peter Debye [Bohren and Huffman 2004]. The

availability of computers today allows more convenient means to compute complex physical interactions of an electromagnetic wave with a sphere of arbitrary radius and refractive index. Detailed explanations of these calculations are beyond the scope of this thesis, although a Matlab program for calculating Mie scattering coefficients will be discussed. Mie scattering theory is a general solution to Maxwell's equations for spherical particles of arbitrary size and refractive index [Thomas 2006], and accounts for phase shifts arising from light interactions with a higher contrast particle [Van de Hulst 1981]. After careful study of various scattering regimes and their conditions, it is concluded that Mie theory most closely approximates the scattering behavior for microsphere particle sizes much greater than the trapping wavelength (λ = 980 nm in this project). As discussed by Van de Hulst, there are six boundary regions in the "*m*-x (refractive index-size parameter) domain" that inherently approximate scattering behavior [Van de Hulst 1981]. The Mie scattering regime generally holds true for a range of particle sizes from 1/10 to 10 times the incident wavelength [Barth 1984], or roughly when the size parameter, $x = 2\pi a/\lambda$ (where a = particle radius and λ is the incident wavelength) is much greater than 1. More discussion about scattering regimes may be found in my Master's thesis [Pinon 2009].

Elaborating on the concept of light exhibiting momentum and energy in the direction of propagation, incident photons act as a continuous stream exerting radiation pressure that is proportional to the force on a trapped particle [Van de Hulst 1981, Bohren and Huffman 2004]. The incident light has a given intensity, I_o, on an isotropic particle of cross sectional area $G = \pi a^2$. The force acting on the particle is then expressed as:

$$I_o(G/c)Q_{pr}, \qquad \text{(Eqn 2.1)}$$

where c is the speed of light [Van de Hulst 1981]. The coefficient, $Q_{pr,}$ is defined as the efficiency factor for radiation pressure which is a ratio defining the transfer of momentum to the particle from the initial electromagnetic radiation momentum [Van de Hulst 1981, Bohren and Huffman 2004].

Briefly, complete transmission of incident light (i.e. no particle) yields $Q_{pr} = 0$, whereas total absorption is equivalent to $Q_{pr} = 1$ [Burns 1979]. The value of Q_{pr} is most relevant to this project involving force calibration calculations in subsequent sections. For non-absorbing spheres, Q_{pr} = 1-g, where g is the asymmetry parameter defined as $\langle cos\theta \rangle$, which is a weighted average of all scattering angles θ due to elastic scattering [Bohren and Huffman 2004, Van de Hulst 1981, Irvine 1965]. The asymmetry parameter characterizes forward-to-backward scattering from a particle. In the case of isotropic scattering (i.e. uniform scattering in all directions), $\langle cos\theta \rangle = 0$ [Bohren and Huffman 2004, Shah 1991]. A dominant forward scattering ($\theta = 0°$) insinuates a positive asymmetry parameter, whereas a dominant back scattering ($\theta = 180°$) defines a negative

asymmetry parameter value [Bohren and Huffman 2004]. An additional overview of other Mie scattering values and scattering regimes may be found in [Pinon 2009].

As shown in Figure 2.7, a small spherical particle of geometrical cross section, *G*, will scatter incident light that is equivalent to GQ_{sca} and may partially absorb light on area GQ_{abs}. Q_{sca} and Q_{abs} are scattering and absorption coefficients, respectively [Burns 1979, Van de Hulst 1981]. These coefficients depend on radiation wavelength and relate to energy scattered and absorbed by the particle.

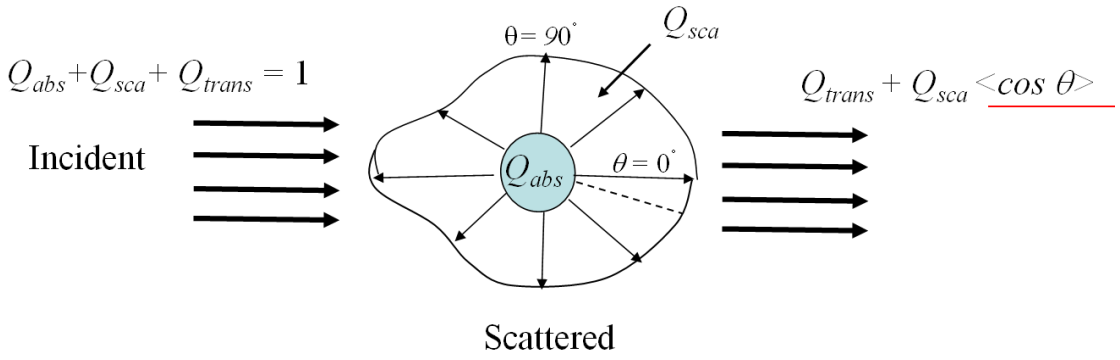

Fig 2.7. Illustration of scattering efficiency factors. Incident energy is expressed as one normalized unit, such that $Q_{abs} + Q_{sca} + Q_{trans} = 1$. Factor Q_{abs} relates to absorption by the particle, Q_{sca} is scattering coefficient, and Q_{trans} is the radiation transmitted. $\langle cos\theta \rangle$ is the asymmetry factor, relating to the weighted average of scattered radiation emitted in a particular angular distribution. (Adapted from Burns, *et al.* 1979)

2.4 Refractive Index Contrast Considerations

We must also consider the refractive index contrast of the particle (We must also consider the refractive index contrast of the particle (n_1) relative to the surrounding medium (n). The refractive index ratio, m (also referred to n_1/n in some literature) gives this relative contrast. We consider the polystyrene microspheres in trapping experiments to be non-absorbing (dielectric) material, meaning the sphere is not electrically conductive and hence, the refractive index ratio, m, of the material is a real constant as discussed by Van de Hulst [1981]. Figure 2.8 demonstrates the relation between Q_{pr} and m, the relative refractive index. As observed, there is a direct correlation between radiation pressure and m, suggesting we would expect stronger trapping forces for higher values of m.

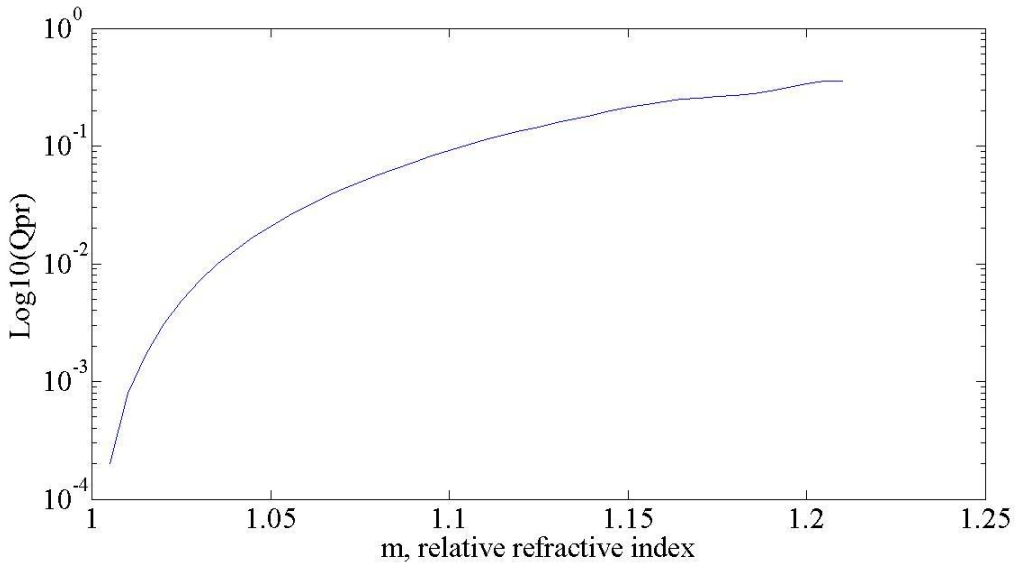

Fig 2.8. Theoretical plot illustrating Qpr as a function of m (relative refractive index contrast, where n_1/n. Mätzler's Mie scattering MATLAB program was utilized to calculate the radiation pressure coefficient, Q_{pr}. (Matlab plot by T. Piñón)

Although we conducted minor modifications to Mätzler's original set of programs for usability, we have verified the validity of these programs by arbitrarily reproducing different extinction curves based on Mie's formulae found in Irvine's article [1965] and Van de Hulst's textbook. By comparing the extinction curve plots, we can see that Mätzler's program accurately calculates efficiency factors as shown in my Master's thesis [Pinon 2009]. These MATLAB programs contain supplementary material that summarizes some of the most referenced textbooks in particle scattering theory, including those of Van de Hulst [1981] and Bohren and Huffman [2004]. Furthermore, Mätzler's code includes comments that often reference page numbers in Bohren and Huffman's textbook.

2.5 Trapping Force Mechanics

We calibrate the optical forces of our beam trap following Constable's approximation for calculating the spring constant and scattering forces [1993]. For a dielectric sphere of given area trapped with two opposing beams, the spring constant (κ) is expressed as:

$$\kappa = 16\pi^2 aS\left[\frac{P_1 Q_{pr,1}\omega_{0,1}{}^2}{\lambda_1{}^2(S^2+4d_1{}^2)^2}+\frac{P_2 Q_{pr,2}\omega_{0,2}{}^2}{\lambda_2{}^2(S^2+4d_2{}^2)^2}\right] \qquad \text{(Eqn 2.2)}$$

where $a = 2R^2/c$ (the incident geometrical cross-sectional area of the sphere), and R = sphere radius (R = 3.01 μm); c = velocity of light in a vacuum; P = incident power; $d^{-1} = \lambda/(\pi\omega_0{}^2)$, where λ = incident laser wavelength (980 nm) and ω_o = Gaussian beam waist (2.1 μm and 4.1 μm for two fiber types used); S = fiber separation (typical range 50 μm to 145 μm); Q_{pr} = radiation pressure coefficient which was calculated from C. Mätzler's "MATLAB Functions for Mie Scattering and Absorption" program (2002) [Mätzler 2002].

The total scattering force (F_s) is calculated from the following expression:

$$F_s = \frac{aP_1 Q_{pr,1}/\omega_{0,1}{}^2}{1+d_1{}^{-2}(S/2+z)^2}-\frac{aP_2 Q_{pr,2}/\omega_{0,2}{}^2}{1+d_2{}^{-2}(S/2-z)^2} \qquad \text{(Eqn 2.3)}$$

where z is the distance from the center region between the fibers (i.e. z = 0 corresponds to the center point). It is expected that when both output powers are equal to each other the net scattering force is 0, since the opposing force vectors balance one another. All other parameters in the scattering force expression are previously defined above for the spring constant calculation net scattering force is 0, since the opposing force vectors balance one another. All other parameters in the scattering force expression are previously defined above for the spring constant calculation.

An optically trapped object exemplifies Hooke's Law ($F = -\kappa\Delta x$), similar to a spring in classical kinematics, where F is the restoring force due to the displacement of a particle from its equilibrium position, Δx. The spring constant, κ, is a measure of trap stiffness. A trapped microsphere at rest with Δx = 0 (static equilibrium) will remain at rest (net scattering force = 0). When one of the laser power outputs is changed, the shape and location of the optical trap changes. At that instant there exists an unbalanced force on the trapped microsphere given by Hooke's law where Δx is equal to the shift in the equilibrium position of the optical trap, and the particle undergoes a small displacement.

For example, increasing the output power emerging from the laser on the left results in the equilibrium position of the trap shifting to the right. The stiffness of the trap changes as well. The particle experiences a restoring force that is proportional to the displacement.

A trapped polystyrene microsphere propelled through water with laser force is modeled as a highly overdamped system [Constable 1993]. The equation embodying this motion is:

$$\Sigma F = m\ddot{x} - c\dot{x} - \kappa x, \qquad \text{(Eqn 2.4)}$$

where the drag coefficient, c, is defined by Stoke's Law for a sphere: $c = 6\pi\mu r$ where μ is the dynamic viscosity of water and r is the radius of the sphere. A displaced particle initially undergoes acceleration and the velocity reaches 0 when it reaches new equilibrium in the mechanical potential. Over damping conditions are satisfied when the damping parameter c is larger than the angular frequency,

$$\omega_o = \sqrt{\frac{\kappa}{m}} \qquad \text{(Eqn 2.5)}$$

where κ is the spring constant and m is particle mass [Fowles and Cassidy 2005].

Equivalently, the parameter $\sqrt{\gamma^2 - \omega_o^{\,2}} > 0$, where $\gamma = c/2m$ is satisfied for an overdamped system [Fowles & Cassidy 2005]. The time constant, τ, is determined from the exponential fit of a microsphere's position versus time plot when it is displaced from equilibrium. The spring constant, κ, is then determined from the following equation:

$$\kappa = \frac{6\pi\mu r}{\tau} \qquad \text{(Eqn 2.6)}$$

2.6 Fiber Alignment Theory and Coupling Loss

Before conducting trapping experiments using either the heat-etched trapping platform or guide-fiber platform, we verify coupling from the source fiber through the receiver fibers to ensure excellent alignment which is essential for stable trapping. Fiber misalignments result in loss of power transmitted into the receiving fiber, and negatively impact trapping performance. The coupling efficiency (η) relates to fractional power lost,

and is given by the ratio of transmission fiber power (P_1) and receiving fiber power (P_2):

$$\eta = \frac{P_2}{P_1} \qquad \text{(Eqn 2.7)}$$

The fraction of power lost may be calculated as 1-η.

We model the transmission using a Gaussian beam approximation that includes our experimental parameters [Allard 1990]. The field distribution within the fibers is estimated by the Gaussian function [Allard 1990]:

$$E(r) = E_o e^{-r^2/w^2} \qquad \text{(Eqn 2.8)}$$

In the case for well-aligned, separated fibers with matching mode fields, the efficiency is expressed as:

$$\eta = \frac{1}{Z^2 + 1} \qquad \text{(Eqn 2.9)}$$

where

$$Z = \frac{z\lambda}{2\pi n_o \omega^2} \qquad \text{(Eqn 2.10)}$$

with wavelength (λ), n_o = 1 (when aligning in air), z is fiber separation, which yields an efficiency expression that reflects beam trailing off radially with respect to the mode field radius. The coupling efficiency model approximates for transverse fiber displacement (d) and angular misalignment (ψ) with no mode field radius mismatch (i.e. $\omega_{o1} = \omega_{o2}$). Three fiber misalignment types are illustrated in Figure 2.9.

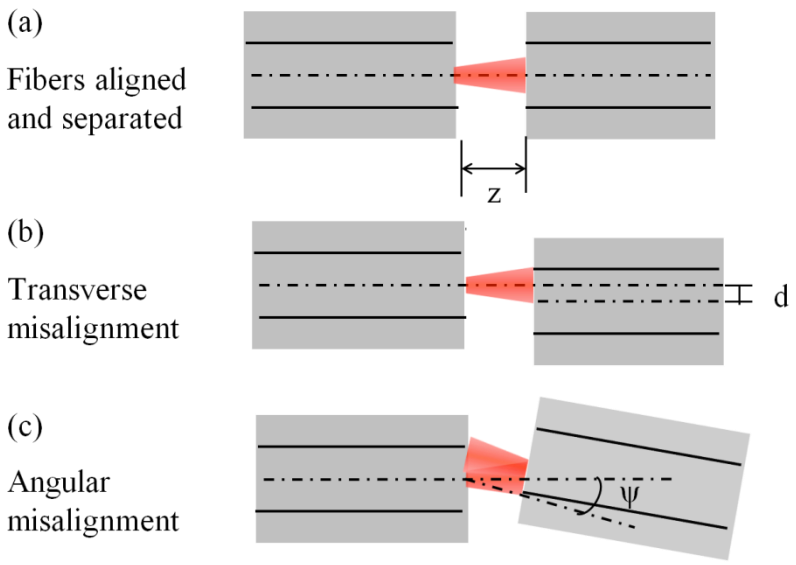

Fig 2.9. Illustrations of fiber misalignment types for Gaussian laser beams. (a) Fibers slightly separated yet aligned, allowing sufficient coupling from the transmitting fiber (left) into the receiving fiber (right). (b) Transverse misalignment whereby fiber cores are transversely offset from one another by distance *d*. Coupling is often poor. (c) Angular misalignment whereby one or both fibers are tilted by some angle, ψ. Again, coupling is negatively affected depending on severity of angular offset. (Adapted from Allard 1990)

METHODS

2.7 Set Up for Trapping Force Calibrations

Here we calibrate the forces applied by our dual fiber optical trap with uncoated polystyrene microspheres (r = 3.01 μm, Bangs Laboratories, Inc.) suspended in water. Polystyrene bead concentration used is ~2-5 wt%. Calibration experiments with polystyrene spheres were performed using the free space optical trap design, in addition to the wedge-groove polycarbonate chip, as discussed below.

The two trapping lasers are fiber-pigtailed, continuous wave diodes (Bookham, Inc. LC95, measured center λ = 974 nm). Force calibration experiments trapping microspheres used two bare, single-mode fibers (Corning HI 980-6 Specialty single-mode fiber, Fiber Instrument Sales), having a beam waist equal to the mode-field diameter of ω_0 = 2.1 μm).

When using the free space optical trap design, we can improve efficiency and accuracy of the fiber alignment process by integrating optical couplers (50% coupling ratio, AC Photonics, Inc., Santa Clara) into the system. The optical couplers are arc fusion spliced (Fujikura 40s). As shown Figure 2.10, the transmitted power from one fiber to the receiving fiber can be maximized by monitoring the power on port “b” of

each coupler while continuing to tweak alignment. A systematic procedure for achieving excellent alignment is crucial for stable traps, and minimizing unwanted off-axis forces.

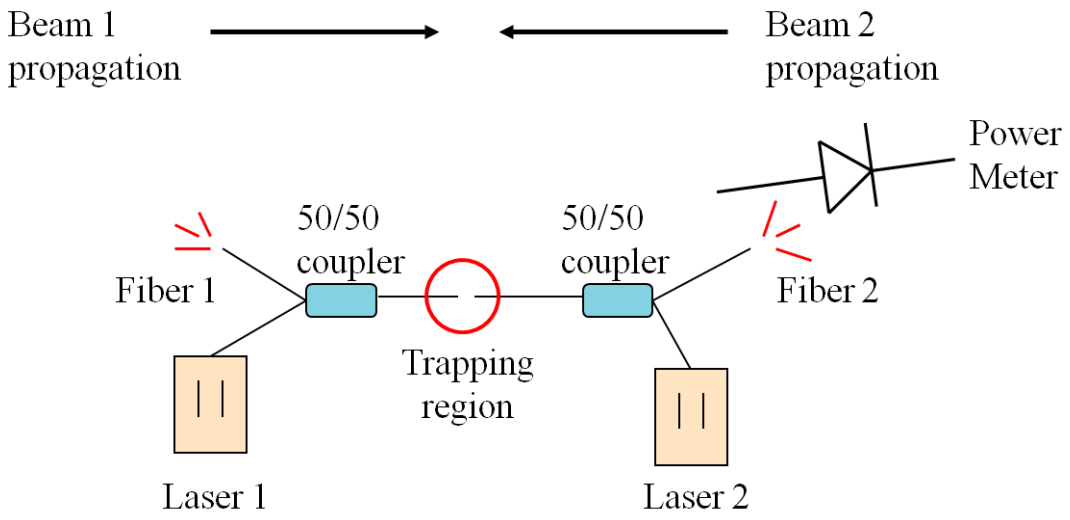

Fig 2.10. Schematic of trapping configuration utilized for bead calibration experiments. Two bare fibers are separately pig-tailed to two 974 nm pump diode lasers. Power transmitted and coupled into the receiving fiber may be monitored by measuring the throughput coupling with a diode power meter. Microscope imaging (not shown) is carried out above the trapping region. (Illustration drawn by T. Piñón)

2.8 Fiber Alignment Procedure

We have developed an alignment process to verify proper fiber alignment for fabricated plexiglass chips. As we have observed, excellent fiber alignment is crucial for trap stability. In the alignment technique, the fibers are first translated and butt-coupled until maximum coupled power is achieved. The power was monitored as a function of fiber separation as translation stages are used to incrementally pull the fibers apart.

In the beginning phases of this project, power efficiency measurements were performed by aligning trapping fibers with independent translation stages XYZ translation stage and one multi-axis translational stage (NanoMax TS 6-Axis Flexure, Thorlabs, Newton, NJ) that permits transverse and angular positioning capabilities.

Later, we applied a similar alignment technique when we assembled our trap-on-a-chip prototypes. Curves exhibiting power as a function of separation are conducted for each assembled chip, and we plot the power decay profiles. These power measurements are useful for determining if the assembled chip has a proper power decay profile, suggesting minimal translational or rotational misalignments. Such misalignments may

induce oscillatory particle motion in the trapping region due to the offset forces [Kawano 2008], resulting in poor trapping performance.

We have applied the previously mentioned fiber alignment method for both plexigass cast acrylic and polycarbonate transparent chips (sections a and b discussed below), providing a trap-on-a-chip scheme.

a. Wedge-groove fiber guide system in polycarbonate chip

Fibers are mounted within a wedge-shaped channel cut at a ~15^{o} angle with a high-speed, steel endmill (Niagara Cutter, HSS S203 square end) in polycarbonate Makrolon® plexiglass (Sheffield Plastics). To minimize surface imperfections from machining that may negatively impact fiber alignment, two additional parallel "guide" fibers are used in the alignment process. Unjacketed alignment fibers are situated alongside each other and right against the wedge channel. These fibers are then affixed with hot melted candle wax (temp = 120^{o}C). The trapping fibers are then positioned between the guide fibers using mechanical clamps and translation stages. Power coupling is measured by first butt-coupling the trapping fibers, then incrementally pulling one fiber apart by ≈ 12.5 μm with the translation stage, while keeping the other trap fiber fixed. We take note of the exponential coupling efficiency drop with increased fiber separation (experiment performed in air). Once the trapping fibers are aligned, hot wax (heated to 120^{o}C on a hotplate) is again applied to fix the configuration and the clamps are removed (see Figure 2.11 for set up). The resulting plexiglass chip has fiber pigtails extending from each edge.

Subsequently, the chip is removed from the alignment hub and is ready for use. We then fusion-splice the trapping fibers to the rest of the laser system. These trap-on-a-chip prototypes permit live trap viewing with standard microscopes, and are also compatible with biological-grade microscope systems equipped with a high magnification water-immersion objective.

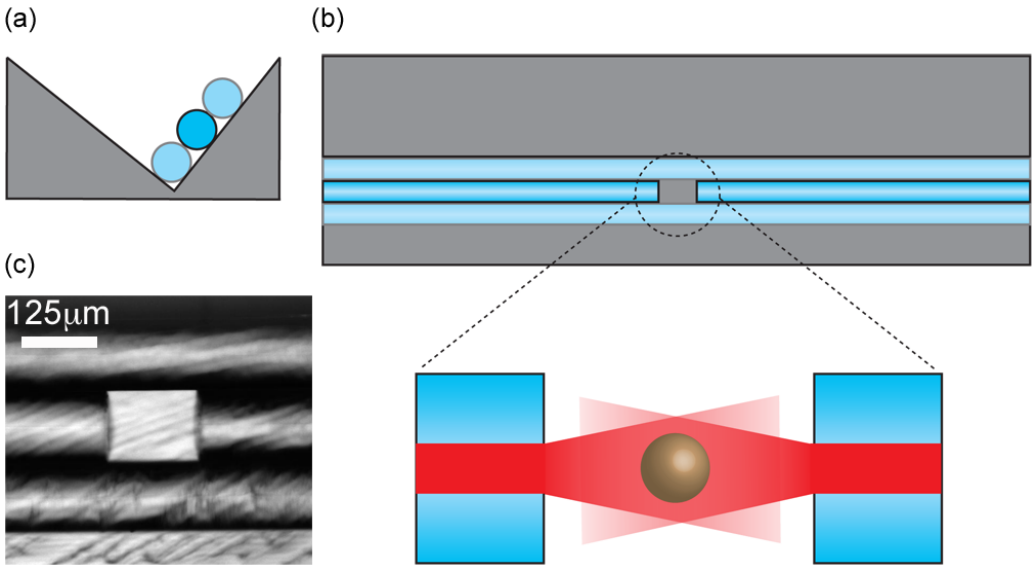

Fig 2.11. Side (a) and top view (b) schematics of the trapping platform with two optical fibers positioned between two "guide" fibers. The trapping region is located in the small space between the separated trapping fibers (125-135 μm). Also shown in (c) a brightfield optical microscope image of the fiber bundle at the trapping region. (Illustrations drawn by L.S. Hirst)

b. Heat-etched fiber guide in cast acrylic chip

Here, we sought to improve our previous heat-etched channel fabrication process as described in my Master's thesis [Pinon 2009], making this new system more portable and affords improved reproducibility for creating heat-etched channels. In this design (Figure 2.12a), uniform fiber alignment channels are burned ("heat-etched") into transparent acrylic "plexiglass" chips (Lowe's) using high-resistive nichrome wires (36 gauge, Jacobs Online, Moxee, WA) with approximately identical diameter as an optical fiber (~125 μm). Heated wires are ~7.0 cm in length for etching in chips ~5.5cm x 5cm. The wire is tied to a small extension spring and pulled tight across electrical leads from a power supply (BK Precision, model 1672 Triple Output). The chip to be etched is placed under the heater wire and a dummy acrylic chip is placed on top, sandwiching the wire between the two chips. A 370 g hanging weight set is then placed on top of the chips for the duration of heating (90 seconds at 0.62A). The resulting chip with a heat-etched channel is shown in Figure 2.12b. As discussed in my Master's thesis [Pinon 2009], a similar heating process can be used to create multiple channels in one chip, permitting four simultaneous optical traps on a single platform.

(a)

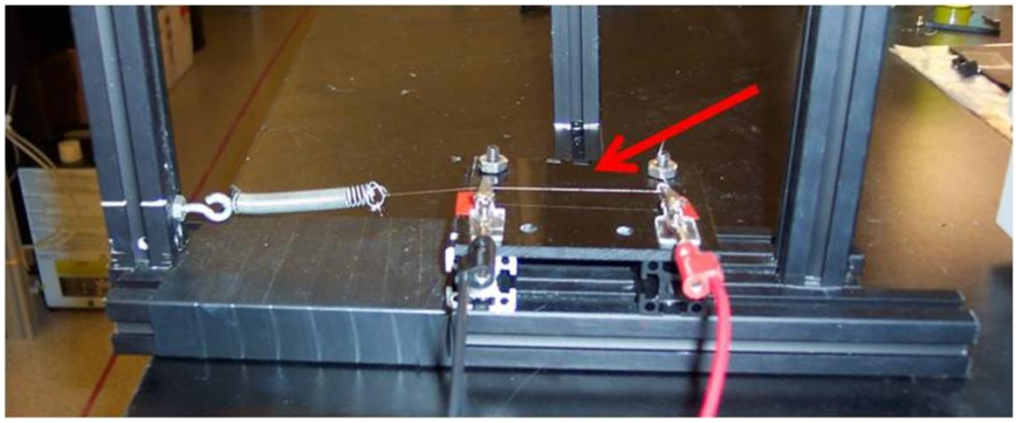

(b)

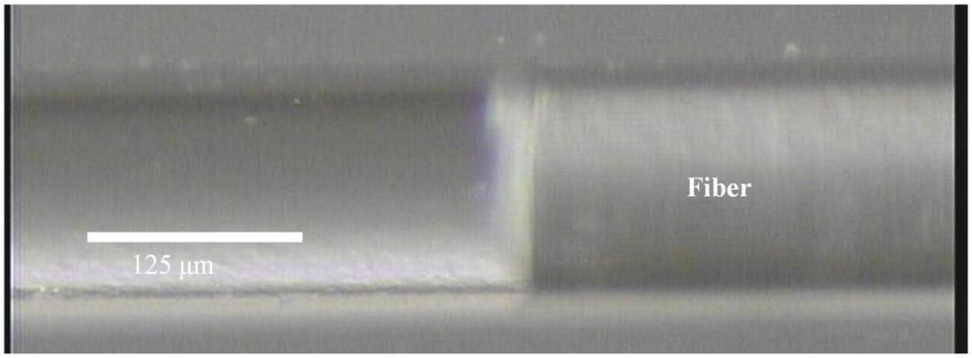

Fig 2.12. (a) Engineered system for heat-etching channels in cast acrylic chips. The configuration consists of aluminum structural bars for support, and an extension spring that provides constant tension to the heated nichrome wire stretched across the chip. (b) Brightfield microscope image showing a bare fiber sitting in a heat-etched channel.

Once the fiber channel on the chip is heat-etched, we can align the two trap fibers using a similar method described in part (a) using mechanical clamps and translation stages. The two trap fibers are then affixed with hot wax (heated to 120^{o}C on a hotplate) and are ready to be fusion-spliced onto the rest of the fiber-coupled laser setup (see Figure 2.13).

Fig 2.13. Fully assembled acrylic plexiglass chip with well-aligned optical fibers sitting in a heat-etched channel and fixed in place using hot wax.

c. Free-space alignment with XYZ translation stages

In this configuration, optical trapping of polystyrene microspheres is conducted using light emerging from two bare single-mode optical fibers (Corning HI980, Fiber Instrument Sales) with each fiber held in place by a fiber clamp on one XYZ translation stage and one multi-axis translational stage (NanoMax TS 3-Axis Flexure, Thorlabs, Newton, NJ) (Figure 2.14a). After fibers are well-aligned, coupling efficiency measurements are conducted to ensure proper coupling profiles (efficiencies are taken in air).

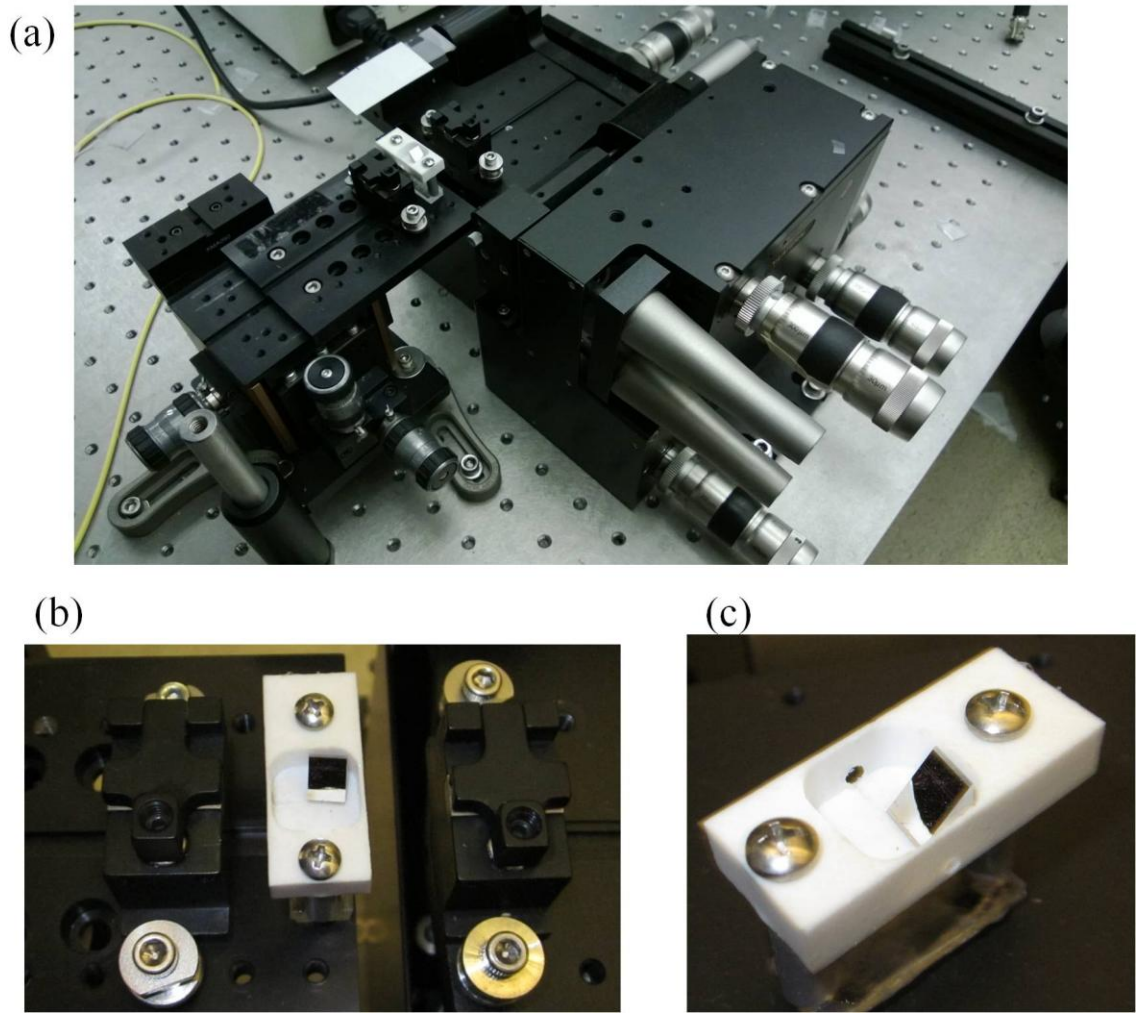

Fig 2.14. (a) Picture of dual-beam trapping system aligned with two XYZ translation stages, with stage on (right) permitting angular alignment adjustments. Bare optical fibers (Corning HI980) are separately fusion-spliced to two 974 nm fiber-coupled diode lasers, and clamped down. (b) Microspheres are trapped in water solution within a machine Teflon well (courtesy of Al Castelli, undergraduate at the time of work). Fibers are inserted through small holes on the both sides of the well that are just large enough for small fiber alignment tweaks. (c) A small right-angle prism sits in the Teflon well permitting the ability to observe trapping (and alignment) in two dimensions—side and transverse views.

2.9 Trap Calibration Experiments

For calibration measurements, we abruptly change the power for one of the trapping beams and track the position of the microsphere as a function of time. Laser power from one laser is suddenly changed (from balanced powers) every 6 seconds using the system interface software, LabVIEW (National Instruments). This power change

causes the trapped microbead to be slightly displaced from the trap center. Power is then restored to match the opposing beam power, causing the bead to return to the trap center. The bead expresses overdamped motion as it moves back and forth from the trapping center. We track microsphere position as a function of time with a MATLAB tracker program. Particle position as a function of time is fitted to an exponential function, and from the function we calculate the time constant, τ. Subsequently, the spring constant, κ, is calculated using the expected relationship for an overdamped system:

$$\kappa = \frac{6\pi\mu r}{\tau} \qquad \text{(Eqn 2.11)}$$

where $\mu = 0.95 \times 10^{-3}$ N·s/m^2 is the estimated dynamic viscosity of water at 23^{o}C [Kestin 1978].

2.10 Video Acquisition Improvements

Previously, as discussed in my Master's thesis [Pinon 2009], particle tracking limitations were limited by a slower camera frame rate of 30 fps (frames per second). Since then, we have upgraded our camera system, permitting a broader range of particle velocities to be tracked per time.

Trapped microspheres are imaged using transmission brightfield optical microscopy (Thales Optem, Inc., model Zoom 125) with a 10x/0.28 N. A. objective. Videos of trapped spheres are captured at 180 frames per second in partial-scan mode using a digital color CCD camera (Toshiba IK-TF5) integrated with the microscope. Images and videos were captured using a Euresys Domino Harmony camera acquisition board and Norpix StreamPix5 digital recording software.

In conducting trapping experiments, sometimes it was difficult to determine whether one or two microspheres are trapped. A trapped microsphere scatters incident laser light that is sensitive to our CCD camera, showing as a red "halo" around the particle. Sometimes more than one particle may get trapped, causing an intense blurred or smeared appearance. Uncertainty in the number of trapped particles can be eliminated by using an optical filter (type: SPF 900, CVI Melles Griot), which serves as a long-pass wavelength filter. This method was beneficial for verifying that only one microsphere is in the trap. It is presumed that having several trapped microspheres will introduce uncertainty in spring constant calculations. Saturating a brightly scattering particle with light from a halogen lamp appears to minimize the appearance of the halo ring and therefore decreases inaccuracies in locating the true particle position.

Particle displacement was initiated by suddenly changing power from one laser "channel." We determined a suitable power change frequency to be every 6 seconds,

allowing the displaced particle to fully complete each exponential cycle to and from the trap center. To verify that the laser powers were truly being modulated in a periodic square-wave fashion, we observed the power modulation on an oscilloscope (LeCroy WaveSurfer® model: Xs Series) with a fast photodiode (Electro-Optics Technology, Inc., ET-2030 Silicon PIN Detector). Oscilloscope traces confirm that the diode lasers exhibit the expected minimal amount of background noise. The oscilloscope traces also confirm that both diode laser powers were modulated instantaneously, as seen by the vertical edges of pulse trains. This implies a trapped microsphere does exhibit exponential, overdamped due to the viscous drag forces of water acting on the suddenly displaced microsphere.

The effectiveness of the MATLAB tracking program strongly depends on the illumination of the trapped particle, microscope focus, particle size, and most importantly, the velocity of the moving sphere. Our particle tracking limitations were once limited by camera frame rate of 30 fps, but have eliminated this limitation with an upgraded camera system, permitting proper tracking of particles as a function of time with the ability to capture up to 180 fps. Depending on particle size and magnitude of sphere displacement, the shortest time constant that can accurately be tracked with our new CCD camera system may be 10-12 times smaller in comparison to our former system (0.13s to 0.17s).

Video clips of microsphere oscillations within the trap were recorded in AVI format (45 to 60 seconds long). The particle tracking program, written by Blair and Dufresne [2008], tracks particle position (in pixels) as a function of time in seconds. We previously reported in my Master's thesis [Pinon 2009] that particle tracking is achievable with sub-pixel resolution (1 pixel $\approx$ 1 μm), and representative graphs show trapped microsphere motion at constant laser powers (before laser power is changed). Acquired data of microsphere motion is then fitted to an exponential function which reflects the system's overdamped behavior. These data points allow us to explore the underlying trapping mechanics by calculating spring constants and restoring optical forces.

The MATLAB particle tracking program is capable of reading AVI and MPG format video clips. The main MATLAB tracking program calls eight other program files, with each file having a different in the tracking process. The program package is comprised of carefully selected image processing parameter filters that track particles in real time, calculating the bright centroid (cntrd.m) of the particle every time a frame is registered by the camera. As summarized in Figure 2.15, the program converts the acquired video into an array that first analyzes the negative of each image. Subsequently, it looks at the red part of the image (the trapped microsphere), and then reverts it back to a positive image again. The bandpass filter program (bpass.m) suppresses background noise and image variations in order to locate the particle of interest. Then the program scans for a peak bright spot (pkfnd.m) for an object about 11 pixels wide, until the centroid (cntrd.m) of the microsphere is found. The results are saved as data arrays. The imaging processing platform is flexible, allowing tracking parameters to be easily modified.

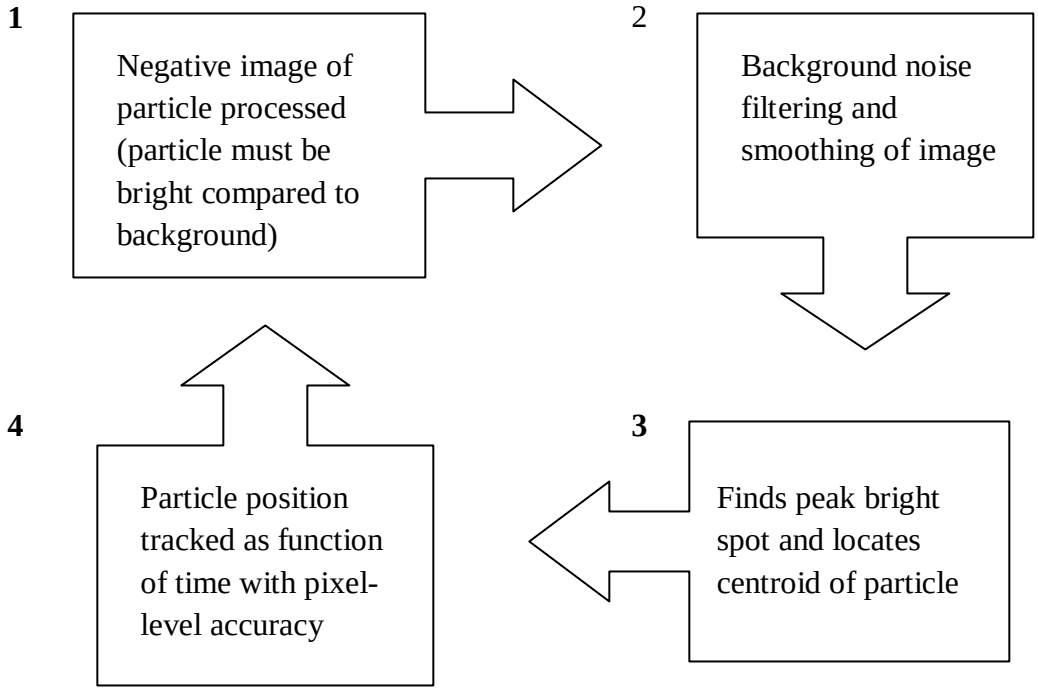

Fig 2.15. Summary of MATLAB particle tracking process from an uploaded .avi format video clip. The program employs a series of algorithms to locate particle position as a function of time for the entire length of the video. (Figure by T. Piñón)

RESULTS

2.11 Testing Chip Prototypes: Measurements of Coupling Efficiency

This section reports on the development of three prototypes used for optical fiber trapping suspended polystyrene beads in water. Here we focus on the chip fabrication process, assembling the trap fibers within the trapping region and subsequently verifying suitable fiber alignment. Using a "guide-fiber" system, wherein the trapping fibers are aligned.

We also sought to characterize alignment efficiency of fabricated trap-on-a-chip prototypes. By carefully executing the fiber alignment technique elaborated previously for chip assembly, coupled throughput power is monitored as we increase fiber separation by increments of ≈ 12.7 μm, until a separation of ≈125 μm is achieved. The coupling efficiency for a fabricated chip is compared to measured efficiency using XYZ and 6-axis optical alignment stages (See Figure 2.16). Both methods shown here use fibers of core radius = 2.1 μm

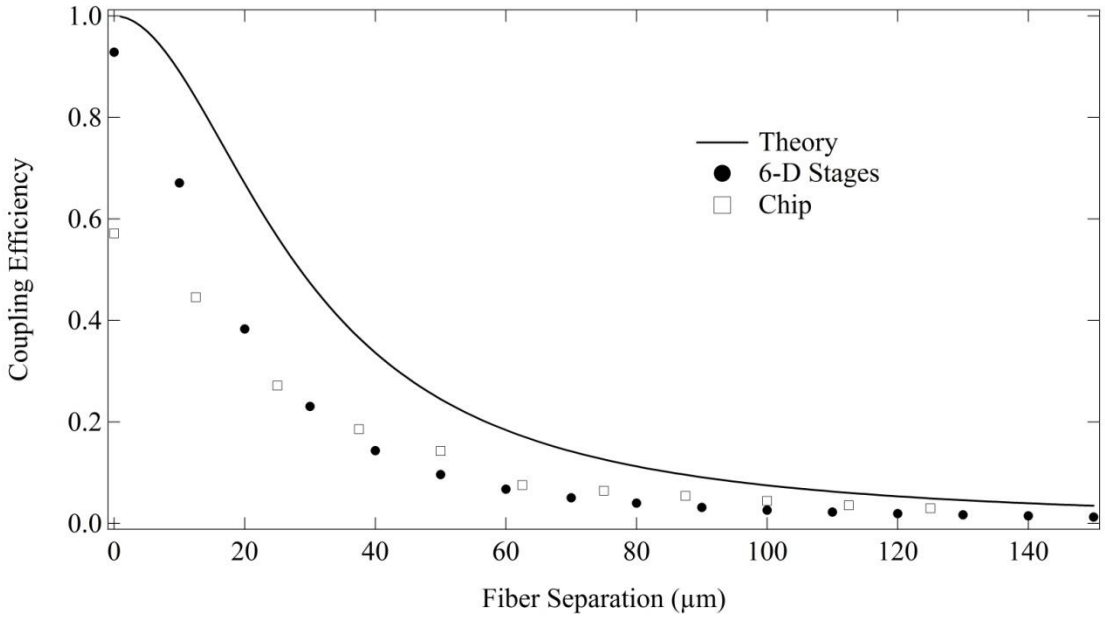

Fig 2.16. Plot showing representative coupling efficiencies as a function of fiber separation for single-mode trapping fibers (ω_0 = 2.1μm). The theoretical curve is based on transmission of Gaussian beams between perfectly aligned fibers (Equations 2.8-2.10) [Allard 1990]. (IGOR Pro plot by T. Piñón)

We then compare two fiber types: Corning HI980 fiber (beam waist ω_0 = 2.1 μm) and SMF 28e (beam waist ω_0 = 4.1 μm) to evaluate differences in efficiency profiles. As seen in Figure 2.17, in comparison to the SMF28e fiber type, the HI980 exhibits a more pronounced exponential drop in efficiency for increased separation. On the contrary, the SMF28e fiber exhibits a more gradual drop in power efficiency due to its larger core size, and also a more gradual beam divergence.

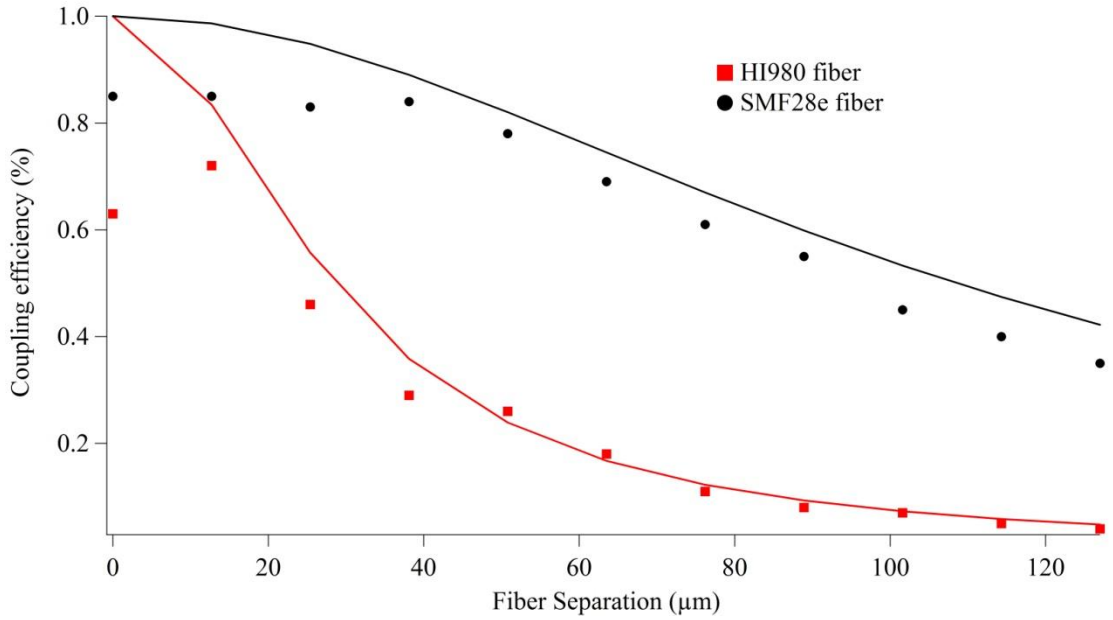

Fig 2.17. Plot showing coupling efficiency profiles for HI980 fiber and SMF 28e fiber. Measured efficiency data points are recorded at increments of separation ≈ 12.7 μm for both fiber types. Fiber core size is the largest factor that influences efficiency profile shape and relative drop in coupling for a given separation. (IGOR Pro plot by T. Piñón)

2.12 Trapping Calibration Results

The theoretical plot (Figure 2.18) depicts the range of spring constants (κ) as a function of fiber separation for two fiber types utilized in trapped bead experiments ((red curve): Corning HI980 fiber, $\omega_0 \approx 2.1$ μm and (black curve) SMF28e, $\omega_0 \approx 4.1$ μm). Additional theoretical plots of spring constants as a function of fiber separation with SMF28e fibers are depicted in my Master's thesis [Pinon 2009]. I use those initial results with SMF28e fibers as a foundation for our continued experiments with HI980 fibers.

The calculations here account for the trap wavelength of $\lambda = 974$ nm and balanced power of 15 mW from each fiber (left and right) in the dual-beam trap configuration. 15 mW is a midrange power setting utilized in our experiments involving trapped microspheres.

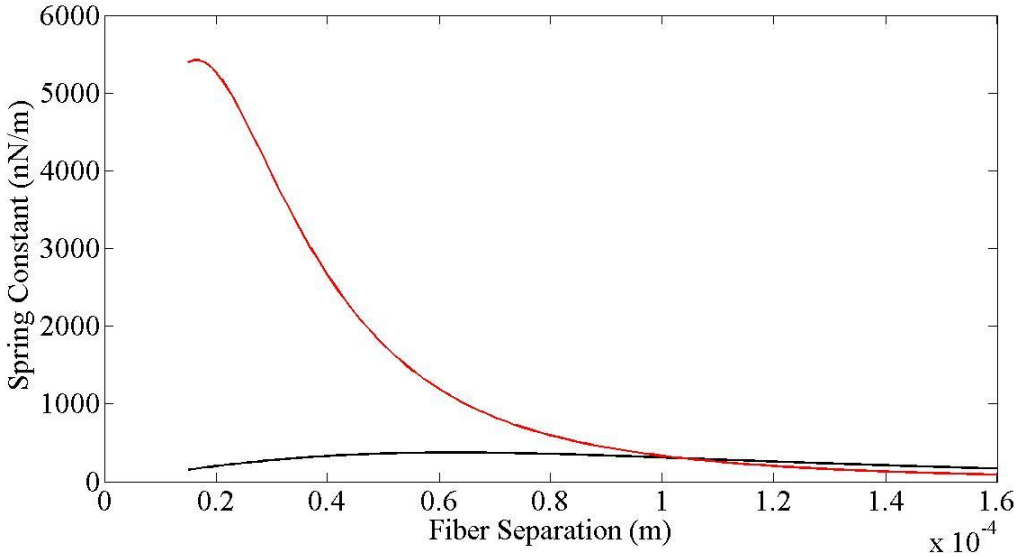

Fig 2.18. Theoretical plots highlighting the range of spring constants achievable for a range of fiber separation at a power setting of 15 mW (incident from each beam) for a trapped polystyrene microsphere in water (diam ≈ 6μm). (Red curve): Corning HI980 fiber, $\omega_0 \approx 2.1$ μm and (Black curve) SMF28e, $\omega_0 \approx 4.1$ μm). (Matlab plot by T. Piñón)

To further characterize the dual-beam trap, we estimate the net scattering forces acting on a trapped microsphere and map the potential energy wells present in the trapping region for the two fiber types (Figure 2.19). Depictions of both force quantities and potential energy values are dimensionless, and are solely meant to illustrate their relative profile shapes rather than yield specific values. These plots are based on trapping with balanced laser powers and fiber separation of 125 μm.

As shown in Figure 2.19a, the net scattering force at 62.5 μm is zero for a microsphere in the center of the trap. Also, it can be shown that intensity drops off exponentially with increased distance from the fiber end, due to the Gaussian nature of the trapping beams. In contrast to the SMF28e fiber, the projected scattering force for the HI980 fiber has a greater exponential drop in force than the SMF28e, giving the HI980 a flatter scattering force profile. This can be attributed to the smaller core of the HI980 and wider beam divergence angle, which translates into a more dramatic decrease in intensity for the distance range of 45 μm to 80 μm. Unlike the SMF28e fibers that yield a more gradual force decrease as a function of distance from ~30 μm to 95 μm. Thus, the differences in intensity profile for the two fiber types are directly associated with the scattering force imparted on a trapped particle.

Figure 2.19b illustrates calculated mechanical potential energies, showing slight profile shape differences for each fiber type. For reasons just described above, the potential energy profile for the HI980 fiber has a more shallow appearance while the SMF28e yields a deeper energy well. Furthermore, it appears that using SMF28e fibers

for trapping may be more favorable for trapping particles with a broader size range and low-contrast particles that are more difficult to trap due to better trap stability (experiments in progress for future publication). However, the use of HI980 fibers are more preferable if larger trapping forces are required for the desired experimental application (i.e. low-contrast optical stretching of soft materials such as lipid vesicles, Chapter 4).

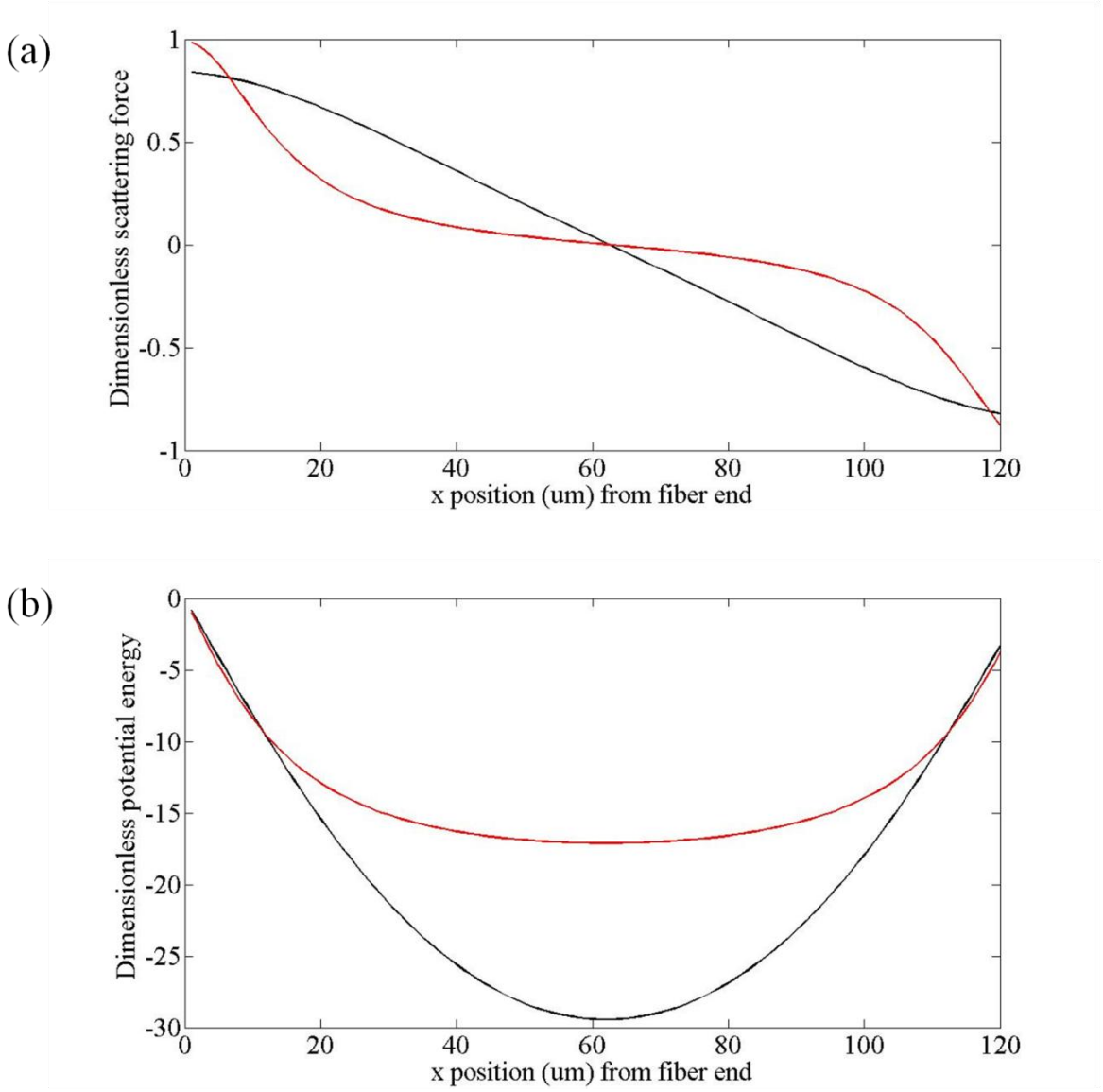

Fig 2.19. (a) Theoretical plot of net scattering force as a function of distance from the left fiber in a dual-beam trap configuration. Fiber of mode field radius $\omega_0 \approx 2.1$ μm Corning HI980 nm fiber (shown in red) is contrasted with SMF28e fiber of radius $\omega_0 \approx 4.1$ μm. (b) Theoretical plot depicting the potential energy for the dual-beam trap, also as a function of distance from the left fiber tip (red curve refers to $\omega_0 \approx 2.1$ μm fiber type, and black curve depicts $\omega_0 \approx 4.1$ μm fiber type). A stable, trapped particle will sit at the bottom of the potential well. (Matlab plots by T. Piñón)

After gathering data curves using the upgraded camera system, we successfully trapped 6 μm diameter microspheres suspended in water and the behavior of trapped

microspheres was evaluated. Optical trapping forces are calibrated by suddenly increasing (or decreasing) one laser from balanced incident power setting. In response to the power change, the microsphere rapidly changes its z-direction position. The water provides a highly overdamped environment, causing the microsphere motion to exponentially decrease and approach zero velocity. Balanced powers are then restored, causing the microsphere to return to the center of the trapping region. We track the position of microspheres moving through water as a function of time with the MATLAB tracking program. An example of a trapped microsphere is captured in Figure 2.20.

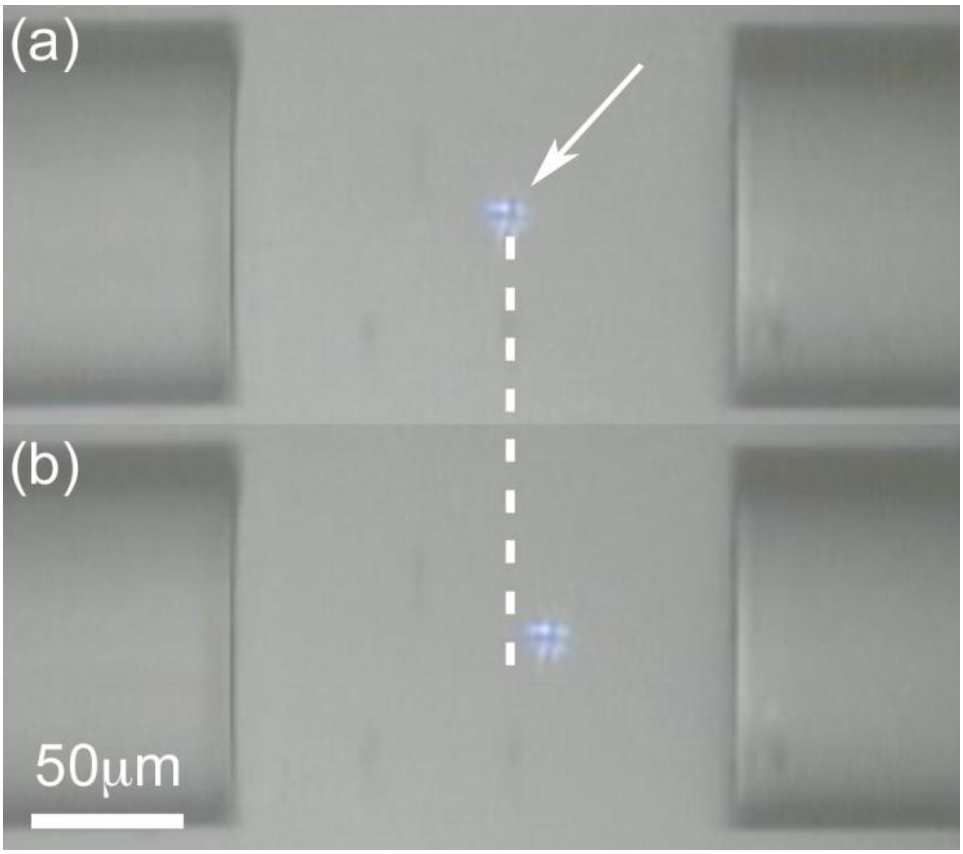

Fig 2.20. Brightfield microscope images of (a) an optical trapped 6 μm polystyrene bead in water initially trapped at 20 mW and (b) a bead displaced from the trap center along the z-axis (beam axis) when one laser is suddenly offset to 30 mW.

We acquired videos up to ~45 seconds long to capture a series of microsphere displacement plots to compare consistency from curve to curve. A representative set of exponential curves is shown in Figure 2.21. At time ≈ 17-23 seconds, the microsphere returns to the trap center when one laser is decreased from 25 mW to 15 mW, re-balancing the power output with the opposing laser. The other curves demonstrate sphere motion when the powers are offset from one another. An exponential offset curve fitting

calculates the time constant for each curve, and from which the spring constant is then determined.

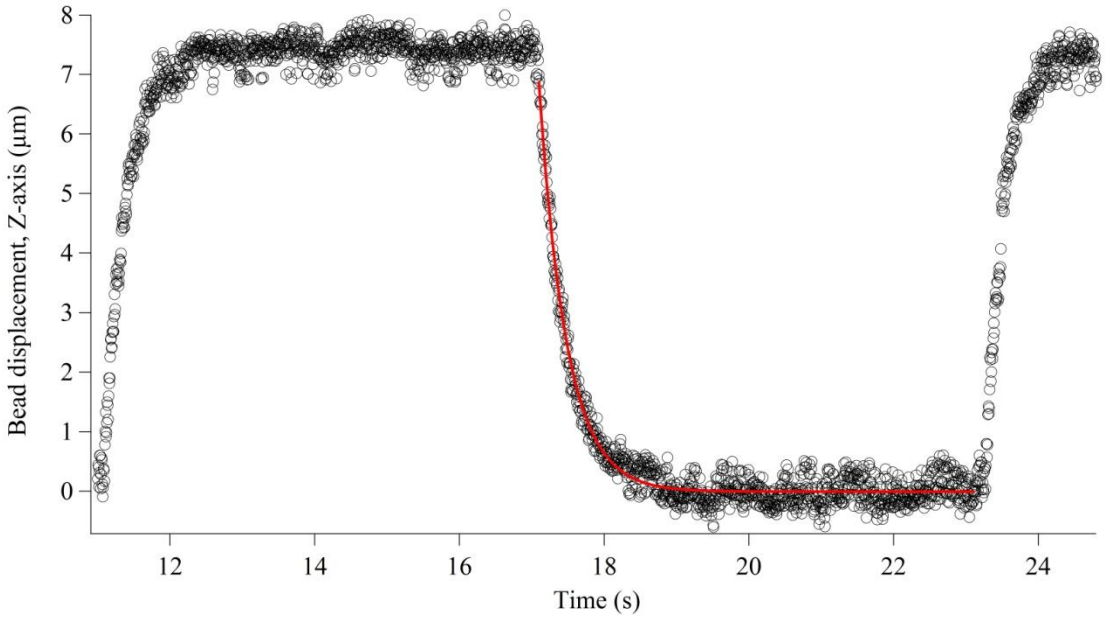

Fig 2.21. Representative MATLAB particle tracking program plot of a displaced microsphere (diam = 6 μm) position versus time. One laser power was systematically modulated from 15 mW to 25 mW then back to 15 mW every six seconds. At time ≈17-23 seconds, the microsphere has returned back to the trap center (where both lasers are balanced at 15 mW). The increasing exponential curves are for the situation of offset lasers, causing the microsphere to be displaced from the trap center.

In addition to verifying consistency for curves within the same trial run, we also compared displacement curves for different power settings. As shown in Figure 2.22, our particle tracking system has the ability to resolve relatively small differences in spring constants for a narrow window of incident trapping powers (10-30 mW). These data sets had experimental errors ranging from 0.7% to 11% when compared to their respective theoretical spring constants.

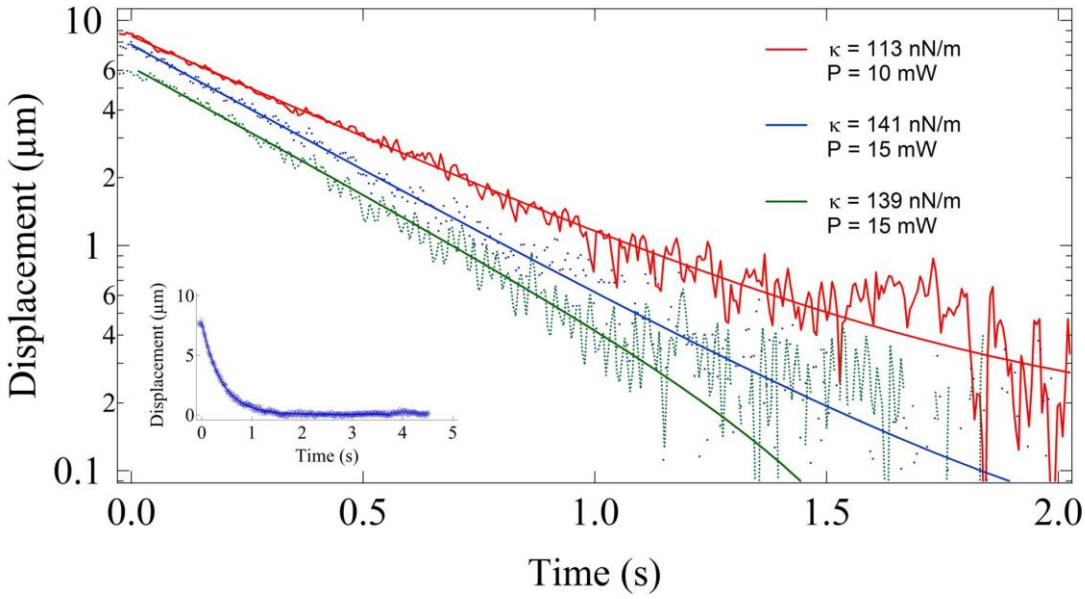

Fig 2.22. A log/lin plot of bead displacement as a function of time after a sudden laser power asymmetry and subsequent rebalancing where the beads fall back into the trap center. Inset is a typical displacement plot on linear axes.

The results resented in Figure 2.22 demonstrate that the displaced particle motion does exhibit overdamped behavior, giving spring constants in the range of 104-145 nN/m and are in good agreement with theoretically expected values from [Constable 1993]. Measured time constants (τ) for displaced 6 μm spheres returning to the trap center (when the laser powers become balanced) ranged from 0.52 to 0.37s for all experimental trials. These measurements were carried out with fiber separations ranging from 125-135 μm, yielding resultant scattering forces of 30-49 pN. We chose to explore lower-range scattering forces to test the limitations of the trap at powers just higher than the minimum power required to maintain a stable trapped microsphere.

We also find, through observation, that trap behavior is more sensitive at lower powers when fibers are slightly misaligned. Higher incident powers seem to artificially make the trap appear more stable, but when trap power is decreased, the particle typically oscillates more noticeably within the trap. Thus, exploring these lower-range forces and yielding spring constants close to the expected values confirms the plausibility of our trap-on-a-chip platforms for exhibiting excellent alignment. In some trials, the curves are unusually steep and do not have acceptable exponential curve fits. One explanation for this is scattered light from the microsphere interferes with the tracking program's ability to accurately locate the particle's center.

In general, there have been vast improvements to our imaging capability since the inception of this project. Our new camera system has a 6-fold higher frame rate than our

older system, allowing us to track moving particles with exponential smaller time constants than before.

In comparing the stability of traps with our earliest data using XYZ translation stages (and before testing the coupling efficiency as a function of fiber separation), we now see a noticeable improvement in x-axis stability for the fiber-guide plexiglass chip system. One way we evaluate the stability of a trapped microsphere is to assess the MATLAB program's tracking of microsphere motion in the x-axis (transverse axis) direction. Acceptable traps have minimal noise fluctuations of +/- 0.5 μm.

Figure 2.23 shows the normalized x-axis displacement as a function of time for microspheres trapped using XYZ translation fiber alignment method and the "fiber-guide" on-chip system. Interestingly, when conducting the microsphere displacement experiments with the former XYZ translation technique, we would occasionally notice immediate fluctuations in x-axis microsphere motion when one laser power is suddenly changed. However, while the z-axis exponential curves were in good agreement with calculated theory (6-9%) the plots did show slight fluctuations in microsphere position after respective power changes were completed. In general, we observed less noise when the trap-on-a-chip design was evaluated, reducing sudden fluctuations in microsphere motion immediately after any power change. This suggests our trap-on-a-chip design has marked improvement in fiber alignment for this configuration.

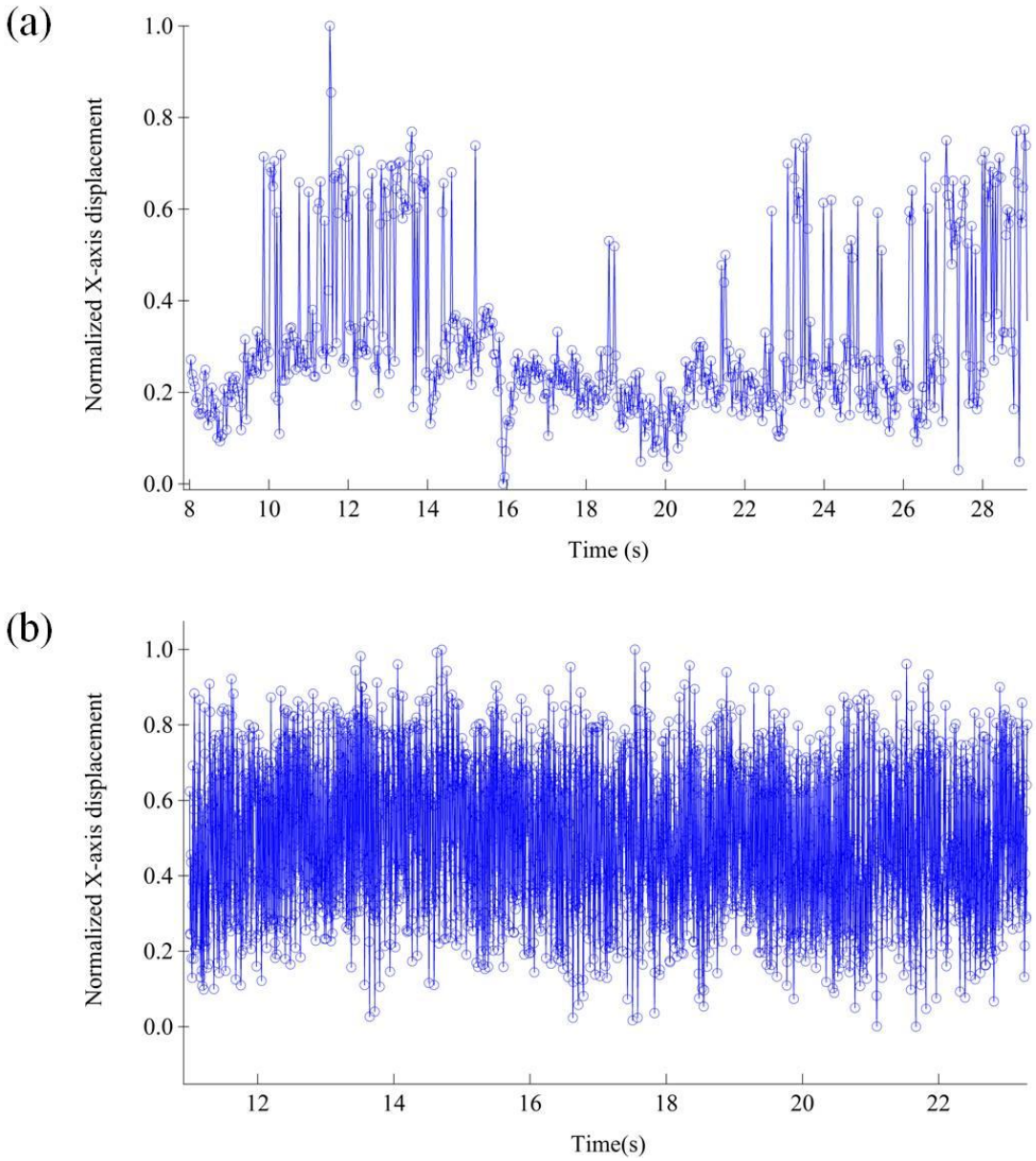

Fig 2.23. MATLAB particle tracking program plots of noise in the transverse (x-axis) direction for a displaced microsphere (d = 6 μm). (a) Plot of normalized x-axis displacement as a function of time for microsphere trapped with early XYZ translation method. Camera acquisition rate ≈ 30 frames per second. (b) Plot of normalized x-axis displacement as a function of time for a 6 μm microsphere trapped on the fiber-guide plexiglass prototype. Data points were acquired with the newer camera system with acquisition rate ≈ 180 frames per second.

The microscope-CCD camera configuration is sensitive to exterior motion vibrations in the room and audio noise. Although the microscope was mechanically stabilized, some vibrations could still induce some error during video acquisition that may cause fluctuations in apparent microsphere position.

CONCLUSION

In this section, we demonstrate the use of a dual-beam optical fiber trap for manipulating microspheres in water. Microspheres are trapped using three techniques, including plexiglass trap-on-a-chip prototypes fabricated with off the shelf materials. We evaluate the trap alignment efficiency for each setup: 1) trapping using XYZ translational stages, 2) fiber-guide technique for aligning trap fibers in wedge-groove, and 3) heat-etch channel method whereby trapping fibers are aligned along a hemisphere-like groove.

A major limitation in trap design has been perfecting fiber alignment. It appears that slight, misalignments > 1 μm in the transverse and 2-3^{o} degrees in angular misalignments offset the electric gradient across the trapping region, affecting trap stability. With the goal of scaling down our trapping configuration from the XYZ translation stages, we successfully implemented two trap-on-a-chip designs that exhibit acceptable alignment. Here, we elaborate on the fiber alignment procedure we undertake to verify excellent alignment by measuring coupling throughput from the transmitting fiber into the opposing, "receiving" fiber as a function of fiber separation.

In comparison trapping with XYZ translation stages, the trap-on-a-chip scheme offers two marked advantages. The first advantage is the design is much more compact than large, bulky stages fixed onto optical tables. The trap-on-a-chip prototypes are conveniently portable, compact, and utilize mostly consumable materials. Most importantly, these chips may be easily used with traditional biological microscope systems, allowing real time observations and video acquisitions of trapped particles. Since dual-beam optical traps are well-suited for integration with microfluidic chips, we see much promise in continuing trapping studies in a closed chip configuration rather than on an open configuration. Integrating microfluidics and optical trapping have shown promise for various biological and biophysical studies, including single-cell mechanical properties [Cran-McGreehin 2006, Guck 2005, Lincoln 2007, Bellini 2010, Bareil 2007, Remmerbach 2009, Lautenschlager 2011]

In this section we determined the z-axis spring constants (along the beam axis) that aid in quantifying the range of forces for the system. Theoretical spring constants along the z-axis (beam propagation) axis were found to agree well with experimental observations. This suggests the forces imparted on a trapped particle do provide a stable trapping region for holding and manipulating polystyrene beads in water with the three trapping methodologies used. Thus, our designs are effective methods for surveying the range of trapping forces present in our dual-beam system.

In subsequent sections of this thesis, we will continue to use the trap-on-a-chip prototypes, applying their use for biological studies in which we probe the mechanical properties of artificial lipid vesicles.

CHAPTER 3

Refractive Index Measurements of Solutions Using a Fiber-Based Probe

3.1 Introduction

In this section we quantify the refractive index contrast between the interior and exterior solutions used for lipid vesicle trapping experiments. Acquiring accurate readings for the refractive indices of utilized aqueous solutions gives us the ability to estimate the optical forces exerted on stretched vesicles (to be discussed in further detail in Chapter 4). Due to equipment constraints, we set out to design this fiber-based probe system. We then implemented this refractive index meter for measuring the refractive indices of our two different aqueous solutions used in trapping experiments: solubilized D-glucose and poly(ethylene) glycol (PEG, M.W. 8000) in water. The refractive index probe system consists of one diode laser (center λ = 974 nm, continuous-wave, Agere SL980) and standard single-mode fibers (Corning HI980, Fiber Instrument Sales). We adapt this fiber-probe measurement technique from Chang [2002] and Kim [2004], which compares the Fresnel reflection from the tip of the fiber in air (the reference reading) to the decreased signal reflected when the probe is in solution.

Accurate measurements of refractive index are important for determining characteristics of numerous optical materials and solutions, including those in chemical and materials engineering, and across biological disciplines, to name a few. Commercial refractometers (such as Abbe-type) often rely on minimum deviation angle and critical angle measurements for accurate readings [Sainov 2003]. There is an increasing need for rapid and easy methods for measuring in the near-IR range and UV, with reported measurements that often lack data in these wavelengths for solutions of varying solute concentrations [Rheims 1997].

More recently, other optical fiber refractometers have been exploited, including one system that uses an indium-oxide-coated optical fiber core for determining refractive index of solutions [Del Villar 2010]. "Lossy-mode resonances" of the refractometer vary as a function of the external medium's refractive index [Del Villar 2010]. It is likely that tailored coatings for optical fiber tips may allow flexibility in measuring a wide range of refractive indices in biology and chemistry. Other techniques include interferometric techniques, and the minimum deviation method using a hollow prism shaped cell, which has the advantage of being applied over a wide spectral range including ultraviolet to infrared [Daimon 2007].

To validate the accuracy of our devised probe system, we compare our measurements to index-matching solutions of known indices, and also compare our acquired data to published literature sources for pure water. While more published data exists for pure water measured from UV to the near-infrared range, literature sources found do not provide data for solutions at similar low solute concentrations, identical molecular weight for PEG (8000), nor are optical dispersion curves valid in near-IR range

readily available. Refractive index readings are most dependent on wavelength, but readings are also dependent upon parameters such as concentration and temperature. Due to limited data available, we suspect our refractive index measurements for low concentrations of D-glucose and PEG8000 measured with λ = 974 nm may be the first of their kind.

Estimated measurement index readings for our system are precise within +/- 0.002 precision. Other advantages of the fiber-probe technique include its low-cost (aside from the Optical Spectrum Analyzer), optical-fiber-based components, straightforward optical alignment procedure, and stability from day-to-day. Additionally, this system affords the ability to observe changes in refractive index over time.

3.2 Theory of Operation

Reflectivity is the underlying principle of the system. Here, we examine the reflection from air and volume of solution. Our calculations assume normal incidence of the fiber tip into the test volume. The reflectivity is quantified using Fresnel equations, which compute the fraction of light reflected and transmitted at an interface, but also utilizes Snell's law in simplifying the equations. Snell's Law relates the refractive index of the incident medium and propagation angle to the transmitted refracted angle and through a medium with a different refractive index.

The phenomenon of a light wave bending as it passes through a boundary and into a different medium is described by Snell's law, given by:

$$n_i \sin(\theta_i) = n_t \sin(\theta_t) \qquad \text{(Eqn 3.1)}$$

where n_i is the incident refractive index; n_t is the transmitted refractive index; θ_i refers to the incident angle; and θ_t is transmitted angle past the interface boundary. A schematic showing this refraction for a light wave propagating from a medium with a higher refractive index into a medium with a lower refractive index ($n_i > n_t$) is given in Figure 3.1.

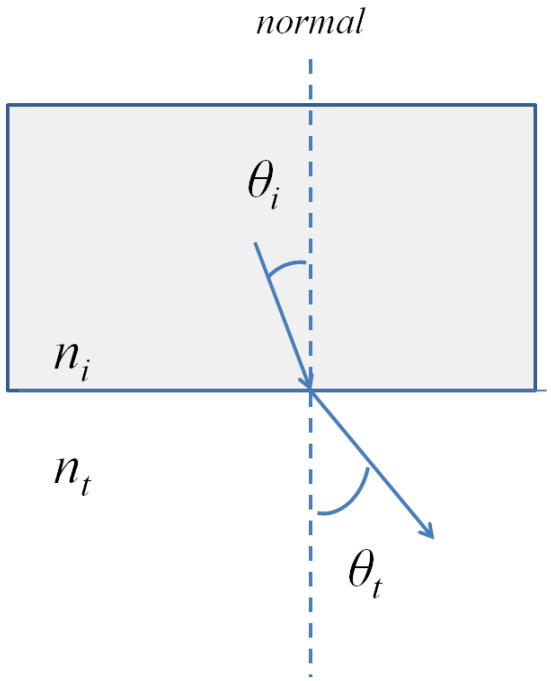

Fig 3.1. Schematic illustrating Snell's Law, considering a propagating light wave travelling initially in a medium of higher refractive index into a medium of lower refractive index, such that ($n_i > n_t$). As shown, the transmitted light wave crosses the normal plane (perpendicular to the surface), and refracts away from that normal. (Illustration drawn by T. Piñón)

One quantifies the reflection from a dielectric medium (e.g. air or aqueous solutions for these experiments) using the Fresnel equations. The fraction of light reflected and transmitted by a flat interface between two media with different refractive indices is expressed as the ratio of the initial electric field reflected over incident. This behavior is dependent upon the direction of the polarization vector (parallel or perpendicular to the surface). When considering the boundary between two media (interface) at which reflection occurs, we may quantify the reflection for both polarizations. For reflection at arbitrary angles, and with notional simplifications using Snell's Law, the Fresnel equations may be expressed as [Hecht 2002]:

$$r_{\perp} = -\frac{\sin(\theta_i - \theta_t)}{\sin(\theta_i + \theta_t)} \qquad \text{(Eqn 3.2)}$$

$$r_{\parallel} = +\frac{\tan(\theta_i - \theta_t)}{\tan(\theta_i + \theta_t)} \qquad \text{(Eqn 3.3)}$$

where $r_{\perp}$ is the perpendicular reflection coefficient; $r_{\parallel}$ is the parallel reflection coefficient. In this thesis, we only consider the case of $\theta_i = 0$, such the incident propagating light wave is perpendicular to the test solution surface (normal incidence). This suggests

$\left[r_{\square}\right] = \left[-r_{\perp}\right]$ at $\theta_i = 0$.

For example, if we consider $r_{\perp}$, after incorporating Snell's Law and some algebraic simplification, we arrive at:

$$r_{\perp}^{\,2} = \left(\frac{n_i \cos\theta_i - n_t \cos\theta_t}{n_i \cos\theta_i + n_t \cos\theta_t} \right)^2 \qquad \text{(Eqn 3.4)}$$

Still assuming $\theta_i = 0$, the ratio of intensity of the reflected wave to the incident wave, *R*, could equivalently, be expressed by:

$$R = \left(\frac{n_t - n_i}{n_t + n_i} \right)^2 \qquad \text{(Eqn 3.5)}$$

Experimentally, we measure the reflection coefficient, *R*, for all tested solutions. Reflected signals are captured in logarithmic scale using an Optical Spectrum Analyzer on a logarithmic scale. By calculating the logarithmic difference of the air reference signal from the captured liquid signals, *R*, is determined.

$$\log_{10} R = \frac{diff}{10} \log_{10} 10 \qquad \text{(Eqn 3.6)}$$

whereby R can then be solved:

$$R = 10^{(difference/10)} \qquad \text{(Eqn 3.7)}$$

"Difference" in Equation 3.7 refers to the logarithmic difference of signals from the air reference signal.

The refractive index of the liquid is then calculated from [Kim 2004]:

$$n_{liq} = n_{fiber} * \left(\frac{1-N}{1+N} \right) \qquad \text{(Eqn 3.8)}$$

where N is related to the ratio of refractive indices of the fiber and air, and R, is given by [Kim 2004]:

$$N = \left(\frac{n_{fiber} - n_{air}}{n_{fiber} + n_{air}} \right) * \left(\frac{1}{\sqrt{R}} \right) \qquad \text{(Eqn 3.9)}$$

Equation 3.9 corrects for the fiber-air interface and partial back reflection from the fiber tip by normalizing the calculated refractive indices for the air signals and in comparison to silica. Considering the measurements are all detected using the same optical source and same optical detector (Optical spectrum analyzer), we may carry out this normalization.

All calculations for this project were automated using a LabVIEW program interfaced with an Optical Spectrum Analyzer (Ando AQ-6315A). 50 averaging measurements are acquired for each test vial, providing an averaged reading over a small time span (just under a minute).

The LabVIEW program also accounts for the refractive index of the optical fiber (constructed of fused silica) by calculating the refractive index of the fiber (n_{fiber}). The refractive index is determined using the Sellmeier formula, with coefficients given at the MellesGriot website [CVI MellesGriot]:

$$n_{fiber} = \left(1 + \frac{B_1 \lambda^2}{\lambda^2 - C_1} + \frac{B_2 \lambda^2}{\lambda^2 - C_2} + \frac{B_3 \lambda^2}{\lambda^2 - C_3} \right)^{1/2} \qquad \text{(Eqn 3.10)}$$

where λ = 0.974 μm; B_1 = 0.6961663; B2 = 0.4079426; B3 = 0.8974794; C1 = 4.67914826E-3; C2 = 1.35120631E-2; C3 = 9.79340025E1.

3.3 Brief Introduction to Measured Solutes

a. Poly(ethylene) glycol (PEG)

Poly(ethylene) glycol (PEG) is a bio-compatible synthetic polymer and is freely soluble in water. It is readily used in biomedical applications, including liposome-based drug therapy making it an attractive compound to study. Here we use high molecular weight PEG 8000, meaning it contains on average 8000 ethylene glycol repeats (see Figure 3.2). In water, PEG is soluble in water from 0°C to about 100°C [Vennemann 1987]. It is worth noting that water plays a role in stabilizing the conformation of PEG, causing the molecules to exist as loose coils [Alessi 2005].

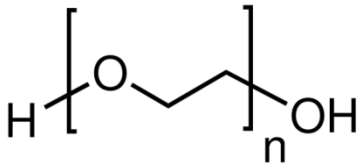

Fig 3.2. Chemical structure of poly(ethylene glycol). (Image from: Sigma Aldrich)

b. D-Glucose

Glucose is a simple monosaccharide and is an essential source of energy for biological organisms. D-glucose is the naturally-found enantiomer of the molecule (referred to as the "right-handed" form), predominantly existing in cyclic form in aqueous solution (see Figure 3.3). In our lipid vesicle trapping studies, we use a concentration of 5 mM D-glucose in water. This concentration is comparable to normal human blood glucose concentration.

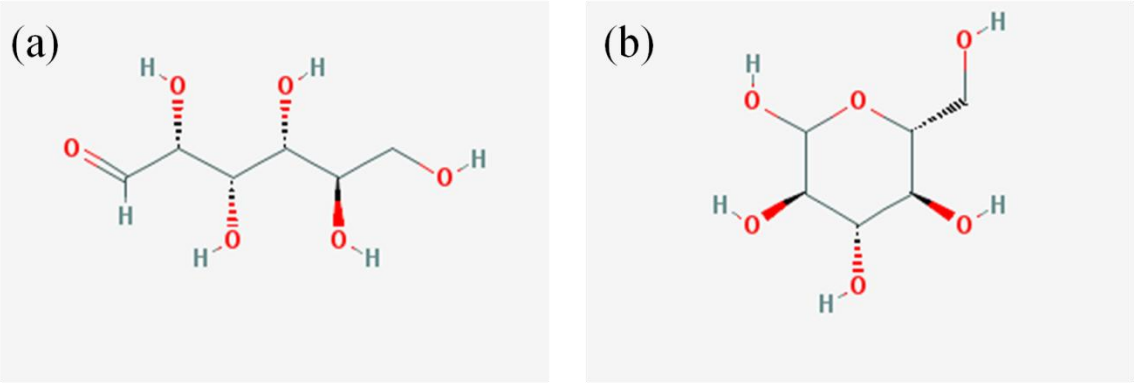

Fig 3.3. (a) Open-chain chemical structure of D-glucose. (b) Cyclic isomer form of D-glucose. In solution, the open-chain form is at equilibrium with the open-chain form, but is most predominant in solution. (Images from: PubChem)

METHODS

3.4 Sample Preparation

In this section we determine the refractive indices of aqueous poly(ethylene) glycol and glucose solutions. Solute masses, depending on desired final solution concentration, were measured using mass balance (Sartorius CP124S) with +/- 0.0001g accuracy. Each solute was carefully massed on weigh paper folded into four squares. After the mass of solute is weighed, the paper is then slightly folded into a funnel which helps in successfully transferring the vast majority of solute from the paper. To achieve desired solution concentration, deionized water (Millipore, resistance of 18 MΩcm) is added to the solute, filling up to the appropriate volume for the needed concentration. After adding water to the solute, the solution is mixed well (high setting) using a vortex machine (VWR Vortex Genie 2). Solutions are then left to sit at least few hours (3-4) which allow full salvation and eliminates residual air bubbles from vortexing.

Serial dilutions of higher solution concentration (e.g. 8 mM) may be incrementally diluted by a desired ratio, allowing refractive index readings to be captured for a narrow window of concentrations. We typically diluted the main 8 mM concentration of solute in water by increments of 10%, such that the following dilutions were 7.2 mM, 6.48 mM, 5.83 mM, and so on, for a total of 11 vials. This range of concentrations is ideal, as it surveys a range of readings above and below the 5 mM concentration of D-glucose and PEG8000 used in trapping experiments. Small centrifuge tubes filled with the test solutions were equilibrated to room temperature before taking measurements, and bottoms of the vials were covered with black electrical tape to minimize possible interference with exterior light sources in the room.

We first employed the refractive index probe system to measure the refractive index of purified Milipore water at room temperature. Subsequently, we measured poly(ethylene) glycol (PEG) M.W. 8000 (Polysciences, Inc.) solubilized in Milipore water, and then, D-glucose also solubilized in pure water. Each solution was filtered through a membrane syringe filter (Millex-GV, 0.22 μm, Durapore membrane) to remove any undesirable particles in the sample. Serial dilutions concentration of PEG 8000 and D-glucose in water were performed, as described in the previous paragraph.

3.5 Fiber-Based Probe for Measuring Solution Refractive Index

In this work, we employ a fiber optics technique to measure the Fresnel reflection at λ = 974 nm from the fiber tip, from which we can extract the refractive index of solutions we use in trapping experiments. The light source is transmitted through single mode optical fibers (Corning HI 980-6 Specialty, Fiber Instrument Sales), with the source fiber connected to an optic coupler (50% coupling ratio, AC Photonics, Inc., Santa Clara, CA) (Figure 3.4). The unused fiber arm from the coupler output is angle-cleaved and dipped in silica matching liquid (n = 1.4587, Cargille Labs) to eliminate back reflection from that fiber. The adjacent output coupler fiber feeds through a polarization controller

(Thorlabs, PLC-900 in-line controller style) before feeding into the test solution vial. Before taking measurements, the polarization is adjusted until the air reference signal is minimized (typically ≈ -5 dBm with our Optical Spectrum Analyzer). It is thought the polarization may drift over time (by a fraction of a dBm), which would affect the calculated *R* (reflection coefficient). Thus, re-adjusting the polarization controller is a good measure.

This initial setting serves as the basis signal for all other solutions to be measured. The probe fiber tip is cleaved with a flat end and inspected in two side-view dimensions with an optical fusion splicer (Fujikura FSM-40S). Typical cleave angles are ~0.3^{o} to 0.7^{o}.

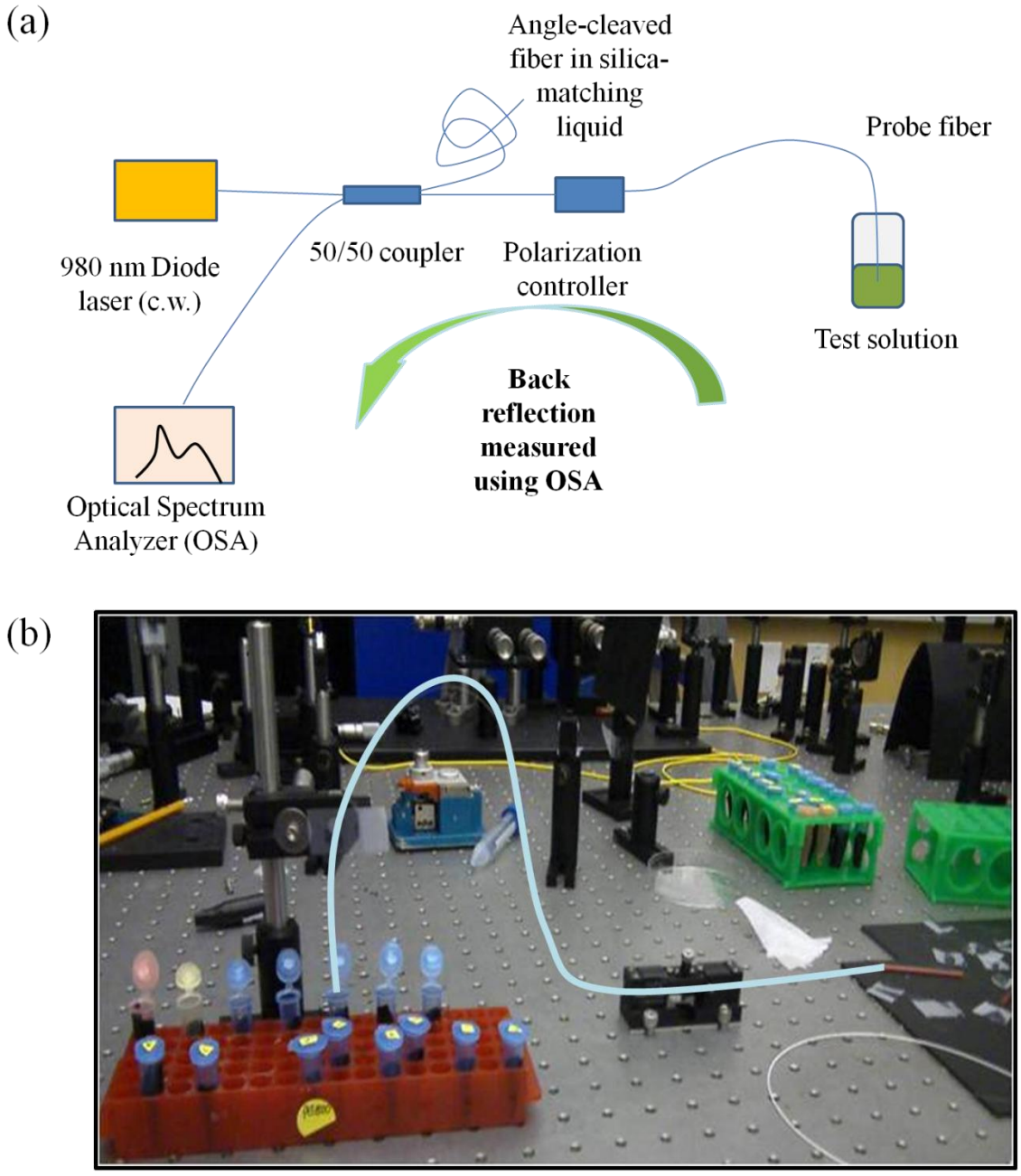

Fig 3.4. (a) Schematic of fiber-based refractive index meter. (Illustration drawn by T. Piñón) (b) Image of experimental set-up of the refractive index meter fiber (light blue) feeding through a polarization controller and into test vials. The fiber is vertically adhered onto an optical post holding a base, allowing the fiber to be lowered (and raised) from each test vial.

From Equation 3.10, one obtains n_{fiber} = 1.4577 at λ = 974 nm. To determine the accuracy of our fiber probe, we measure the refractive indices of refractive index (matching) liquids (Cargille-Sacher Laboratories, Inc.) that serve as our refractive index

standards. As shown in Figure 3.5, we compare our measurements to the known refractive index for a series of eight optical standards. The data shown in Figure 3.5 was captured on two different days, with a total of nine measurements per data set. Also shown are readings for pure water (Millipore, resistivity 18 MΩ cm). Acquired measurements indicate the accuracy of the fiber probe meter is less than ± 0.002.

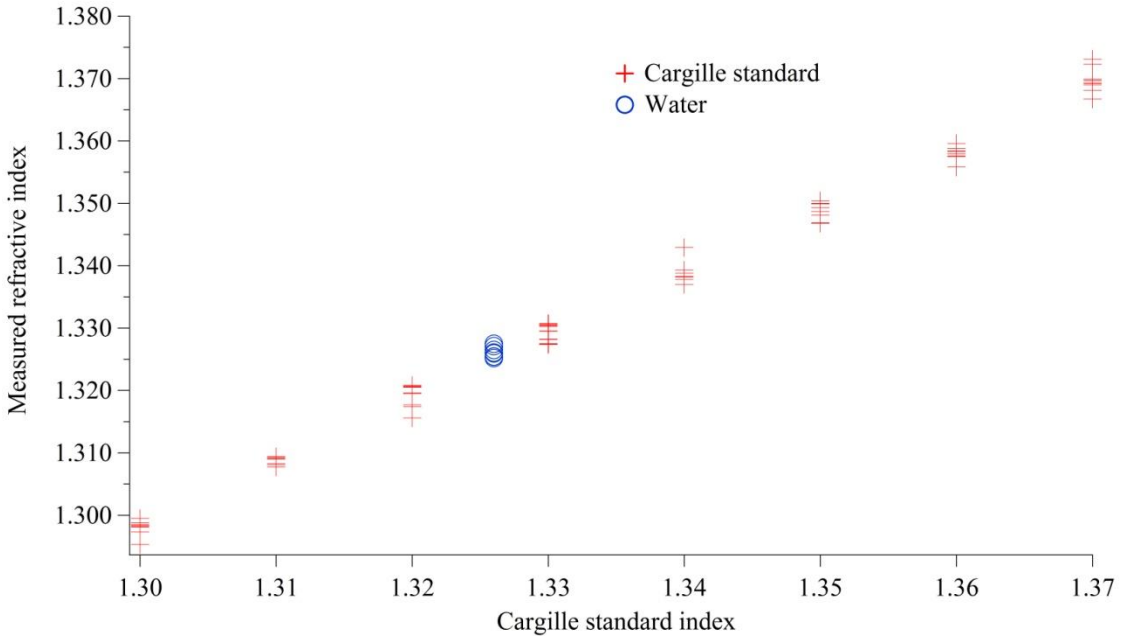

Fig 3.5. Plot showing measured refractive indices of Cargille solution standards (for λ = 980 nm) (red crosses). Also shown is Millipore water (blue circles). Nine readings were taken per data set.

Furthermore, we compare the measured refractive indices of water to published literature values. Several empirical models exist for the index of refraction of water that demonstrate the dependence of wavelength, temperature, and solute concentration on index measurements. While data available for the near-infrared range is limited, some models that fit well with our data are those of McNeil [1977] and Quan and Fry [1995] [Huibers 1997]. Measured values have been compared with each of these models, citing zero average error for wavelengths within the range of 700-1100 nm [Huibers 1997]. Quan and Fry have acquired the wavelength dependence of the refractive index of water across the spectrum from UV to the near-infrared [Huibers 1997].

Following the condensed wavelength-dependent forms of the refractive index of water given by Huibers [1997], we have plotted empirically-formulated dispersion curves with respect to wavelength that were originally formulated by McNeil [1977] and Quan

and Fry [1995] shown in Figure 3.6. These condensed forms assume a temperature of 25°C.

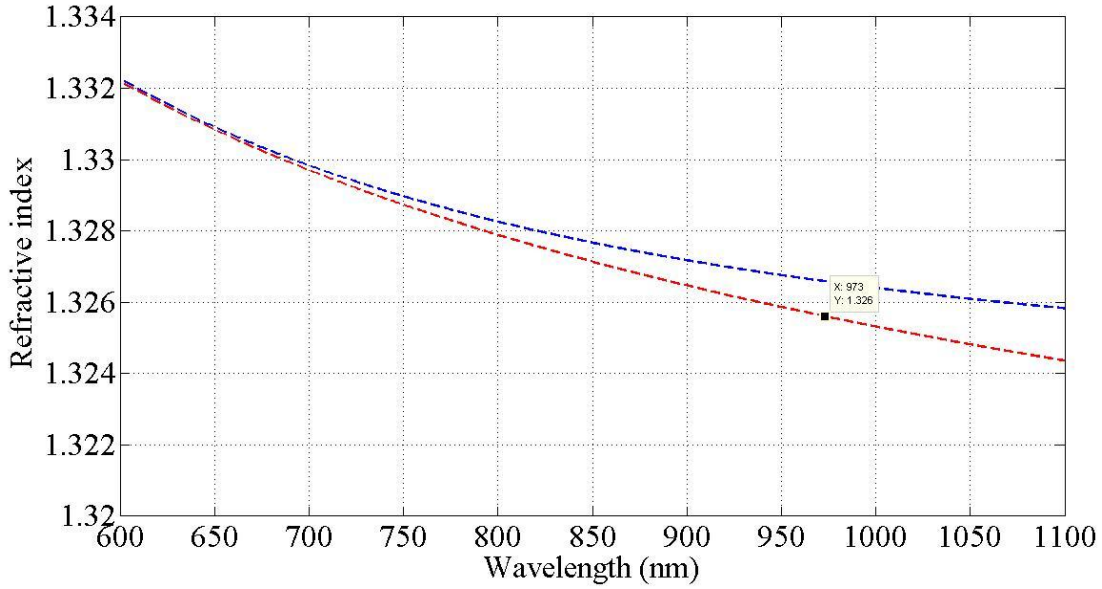

Fig 3.6. Plot exhibiting two empirically-derived dispersion curves for pure water for a range of wavelengths. McNeil [1977] (blue dotted line) and Quan and Fry [1995] (red dotted line). For reference, our trap wavelength (λ = 974 nm). (Matlab plots by T. Piñón)

As observed in Figure 3.6, the index of refraction has an inverse dependence on wavelength. The model of Quan and Fry [1995] have been cited extensively, showing the validity of their formulation for a wider window of wavelengths than the authors originally cited (400nm< λ < 700 nm) [Huibers 1997]. Furthermore, both models shown in Figure 3.6 appear to validate our own data for pure water of $n \approx 1.327 \pm 0.001$ measured with our trap wavelength of 974 nm.

We then apply our fiber-probe system for measuring the refractive indices of two different aqueous solutions: D-glucose solubilized in water and poly(ethylene) glycol solubilized in water. Acquired readings are taken for a range of concentrations that cover the concentrations used in trapping experiments: 5mM PEG 8000 (4% w/v) and 5 mM D-glucose. Figure 3.7 shows a typical acquired optical spectrum for air (reference reading), in addition to pure water, 2.5 mM PEG 8000/water, and 5 mM PEG8000/water.

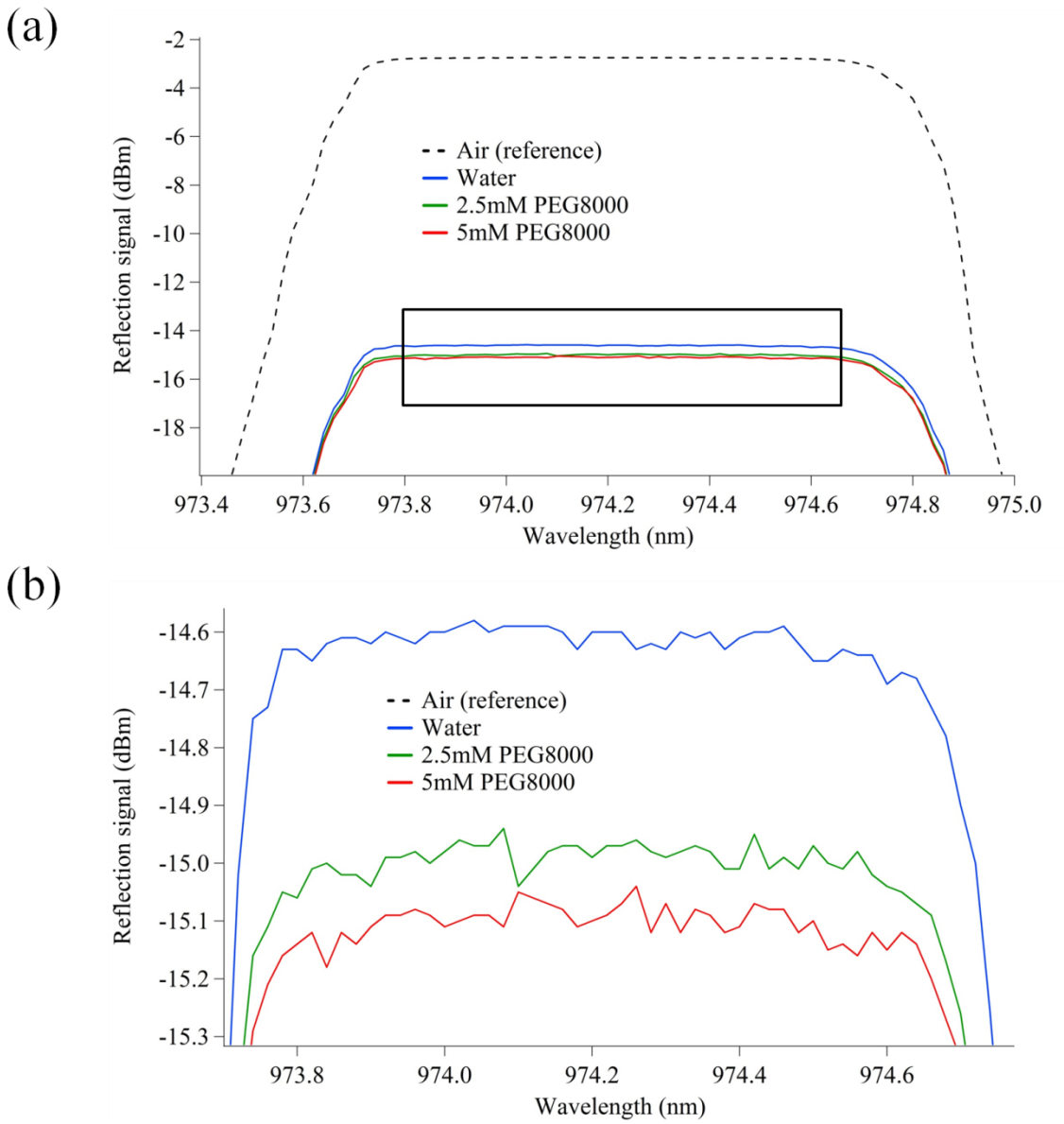

Fig 3.7. Examples of acquired reflection signals captured from an optical spectrum analyzer as a function of wavelength. Only a narrow wavelength window that includes the trapping wavelength of 974 nm is shown. (a) Acquired optical signal of air (reference), Millipore water, aqueous 2.5 mM PEG8000, and aqueous 5 mM PEG8000. (b) Expanded window from (a) highlighting measurements for water, 2.5mM PEG8000, and 5mM PEG8000.

As seen in Figure 3.8, there is a linear trend between measured refractive index and solution concentration of both PEG8000 and D-glucose. However, in the case of

glucose, is expected that higher concentrations of glucose in water will not yield such a linear result, as demonstrated by [Yunus 1988].

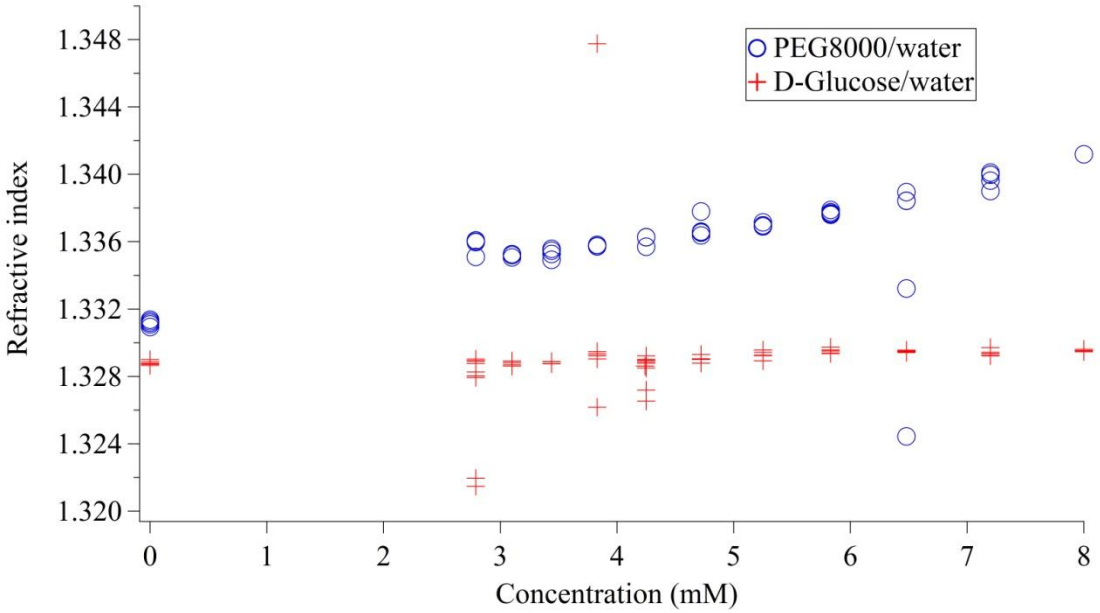

Fig 3.8. Plot of measured refractive index with respect to solute concentration in water. Aqueous solutions of PEG8000 and D-glucose are shown. (Data acquired by Nancy Duque, undergraduate student).

Data points do not reflect the concentration uncertainty, but we estimate it to be ±0.0002. In comparison to published data, the refractive index of glucose was evaluated at high concentrations up to approximately 30 g/100mL (30% w/v) at λ = 632nm [Yunus 1988]. At this single wavelength, nonlinearity was observed for concentrations greater than ~16 g/100mL, but cannot be determined whether this trend is observed at other wavelengths. To date, published optical data for D-glucose in water applicable to our lower solution concentration of 4% (% w/v) measured in the near-infrared range was not available. Similarly, optical data for PEG is limited to Cauchy dispersion constants for the solid-phase polymer with a substantially low percentage of water (~2% water) [Ford 2000].

One limitation of the system is the maximum refractive index we can accurately measure. As shown in Figure 3.9, as the solution refractive index approaches the refractive index of the fiber (n_{fiber} = 1.4577) and using Equations 3.7-3.9, there is some maximum refractive index that can be measured. Logarithmic signal difference is defined as the air reading subtracted from a test solution reading. We assume that acquired readings for higher index solutions (n_{liquid} > 1.4) will have more uncertainty, limiting the

range of indices we can measure with our fiber-based probe. However, the aqueous solutions used for trapping are well below the calculated maximum index reading, so our measurement system is adequate for acquiring readings for indices near ≈ 1.34.

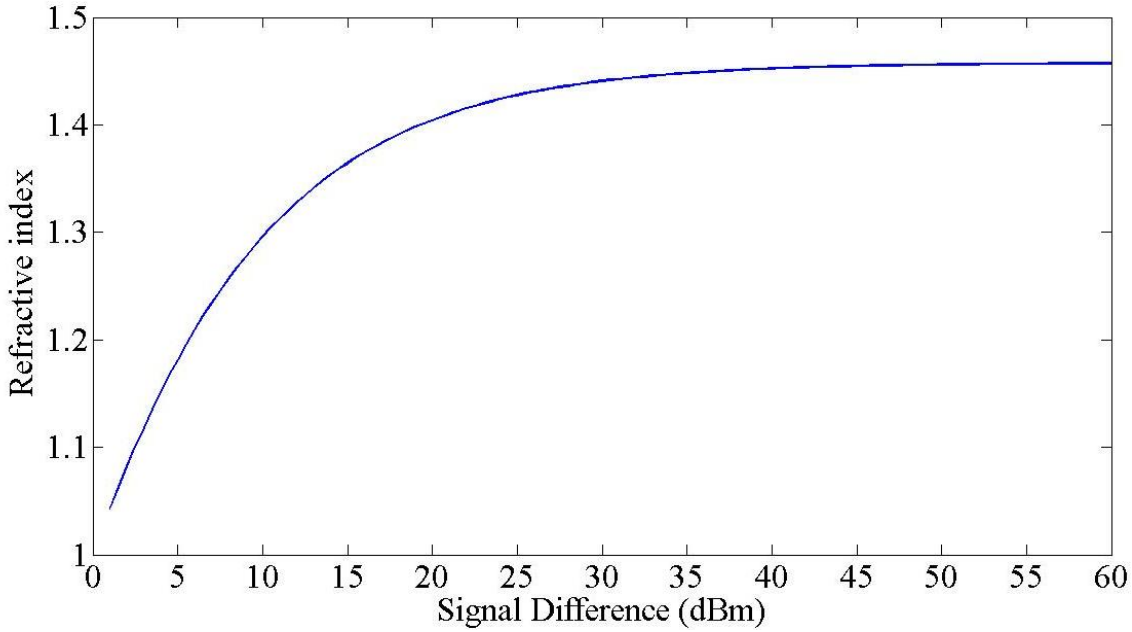

Fig 3.9. Theoretical graph depicting the range of measurable solution refractive indices (n_{liq}) as a function of measured signal difference in dBm (logarithmic decibels). There is a maximum refractive index that may be accurately measured. As n_{liq} approaches that of the fiber probe (n_{fiber} = 1.4577), the uncertainty in measurements will likely increase. (Matlab plot by T. Piñón)

Sources of error include temperature fluctuations and air humidity. Fiber cleave angle could also contribute to measurement errors. While typical fiber cleaves varied from day-to-day measurements (≈ 0.3^o-0.7^o), these slight angles could potentially reduce the magnitude of reflection from the fiber tip. Furthermore, we speculate whether PEG coil conformations could impact refractive index readings.

CONCLUSION

The refractive indices of water, poly(ethylene) glycol/water and D-glucose/water solutions were determined with the Fresnel fiber probe at a wavelength of 974nm. Precision is estimated to less than ± 0.002, and determined values agree well with published literature values for pure water, and exhibit the same degree of accuracy when index-matching liquids specifically for our trap wavelength are measured.

The ease of implementation for this system makes it an attractive (and affordable) technique applicable to various fields of physics, chemical engineering, bioengineering, to name a few. Future studies may more closely determine index resolution for tighter range of solution concentrations, and concentrations with indices closer to the refractive index of silica. We expect this is one limitation of the technique that could restrict the choice of liquid samples to those of indices greater or less than $n \approx 1.4$. Furthermore, possible amplitude drifts due to temperature changes over extended periods of time could be determined, with special attention to thermal effects from the incident probe wavelength.

CHAPTER 4

Fiber Optical Trapping and Stretching of Giant Unilamellar Vesicles

4.1 Introduction

In this section, we demonstrate optical trapping and stretching of lipid vesicles on a compact, plexiglass trapping platform. This is the first time mechanical properties from low optical contrast giant unilamellar (GUVs) mechanical properties have been extracted using a fiber-based dual-beam trap [Pinon 2011, Pinon 2012, Pinon 2012]. Since this first implementation, another research group has also successfully trapped and stretched vesicles using the similar dual-beam trap [Solmaz 2012]. The interesting nature of these works stem from trapping of these low refractive index contrast vesicles in solution, with optical forces that are sufficient enough to even induce vesicle deformation.

Experiments involving exerting tension on vesicles using optical tweezers have shown that light-force interactions can induce shape transformations of the vesicle [Bar-Ziv 1998]. Two probing regimes are discussed in the literature: low-tension and high-tension. In the low-tension regime, applied stress initially reduces thermal fluctuations of the lipid vesicle, causing the vesicle to become tense [Dimova 2002, Dimova 2006]. It is hypothesized that a similar smoothing effect is present for spherical membranes trapped with a dual-beam trap [Solmaz 2012]. In contrast, high tensions cause membrane stretching [Dimova 2002, Dimova 2006], and in the case of dual-beam trapping, the vesicle elongates along the beam axis and contracts in the transverse direction [Solmaz 2012, Pinon 2012].

Here we show stable trapping and show reversible deformation of vesicles with femtonewton trapping forces (an order of magnitude less than trapping polystyrene microspheres in water described in Chapter 2). Similarly to trapped polystyrene microspheres, stable trapping is achieved for lipid vesicles of higher refractive index contrast than the exterior medium. Radiation pressure pushes the vesicle into the center of the trap region between two opposing fibers, and by a combination of reflected and refracted optical rays, the vesicle stretches (elongates) along the beam axis and contracts in the transverse direction [Guck 2001, Ekpenyong 2009]. This trapping technique has applications for probing a variety of soft biomaterials such as biological cells, lipid membranes and protein assemblies.

4.2 Features of Artificial Lipid Vesicle Composition

Artificial lipid vesicles represent an attractive model system for understanding fundamental mechanisms in biological cells. The lipid bilayer provides an important structural role in fundamental biology, forming the boundary of biological cells and organelles. Native biological membranes are comprised of numerous lipid types and other amphiphilic components, including transmembrane proteins, ion channels, and cholesterol.

Here, we focus on the use of phospholipids, a type of lipid comprised of two fatty acid chains, a glycerol unit, a phosphate group, and a hydrophilic head group. The molecular structure of the phospholipid used in this project is DOPC (1,2-dioleoyl-*sn*-glycero-3-phosphocholine) as shown in Figure 4.1.

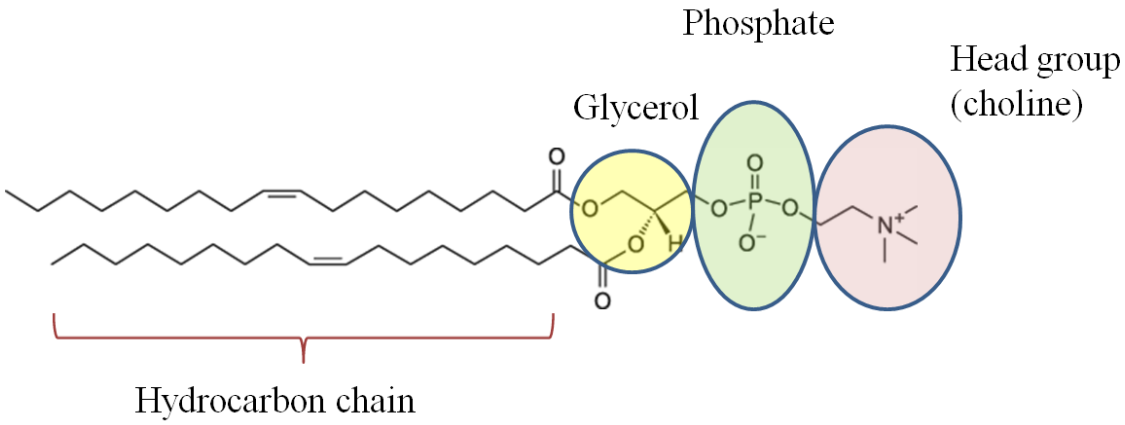

Fig 4.1. Molecular structure of the phospholipid DOPC (1,2-dioleoyl-*sn*-glycero-3-phosphocholine) comprised of two fatty acid "tails" of hydrophobic nature and a "head-group" consisting of a choline head group linked to a glycerol and phosphate group. (Chemical structure modified from Avanti Polar Lipids, Inc.)

We fabricate lipid vesicles comprised of DOPC, and as illustrated in Figure 4.1, the lipid molecule is comprised of two fatty acid tails that each have one degree of unsaturation (one double bond) in the *cis* conformation located at the 9th carbon position from the tail ends. At room temperature, DOPC vesicles are in the fluid (or chain melted) state which gives the hydrocarbon chains flexibility to thermally fluctuate [Hirst 2011].

Lipid vesicles (or liposomes) are phospholipid bilayer sheets that have conformed into closed spheres. Vesicles encapsulate aqueous media in their interior, and are typically suspended in the same media in the exterior. Lipid vesicle formation occurs when phospholipids are dispersed into an aqueous media. The amphiphilic nature of phospholipids leads to a combination of favorable and unfavorable interactions with

water. The resulting conformation is a closed spherical structure that permits the hydrophilic "head-groups" to associate with aqueous media and the hydrophobic hydrocarbon chains to be sheltered from the aqueous media. Large vesicles are non-equilibrium structures, and due to the complexity of interactions at play, it is often difficult to form perfect single bilayer vesicles. The most common structures are multi-layered, multilamellar vesicles.

A bilayer structure is typically 4-6 nm thick, depending on the lipid type, with diameters ranging from nanometers to larger cell-sized ("giant vesicles") of diameters ~10-100 μm with the electroformation process [Angelova 1992] used in this work. The schematic in Figure 4.2 illustrates the fundamental configuration of a lipid vesicle.

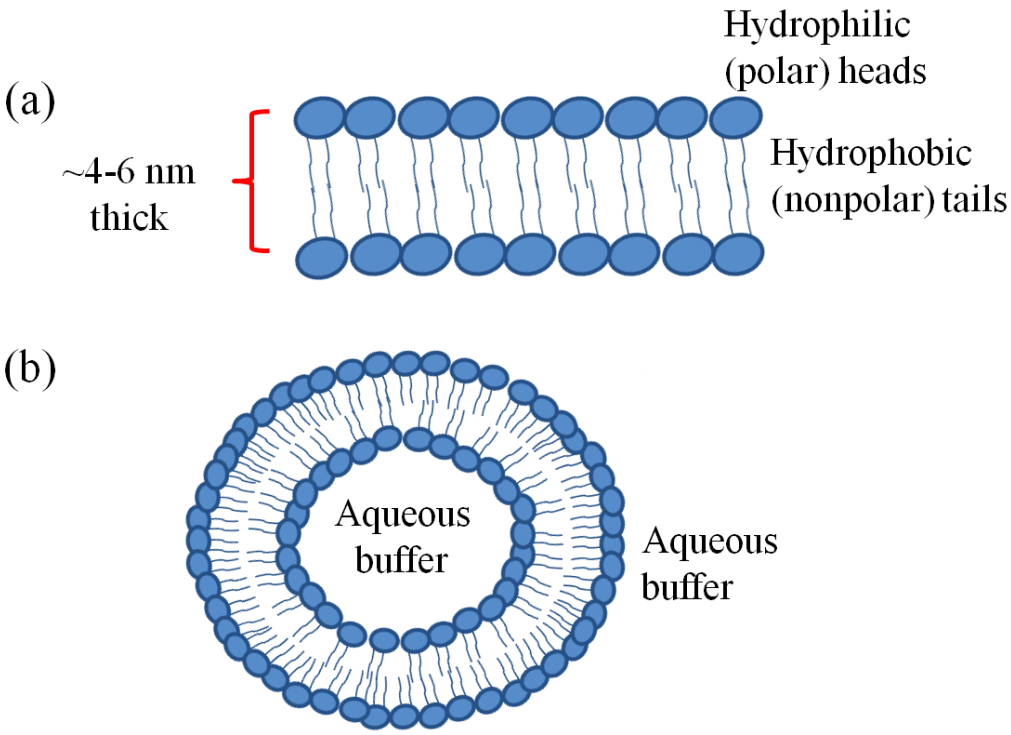

Fig 4.2. (a) Illustration of a lipid bilayer depicting the arrangement of lipid molecules in aqueous solution. In solution, the nonpolar hydrocarbon chain tails orient toward one another, minimizing the contact with water, whereas the polar lipid heads maintain contact with the solution. (b) Cross-sectional representation of a lipid vesicle, comprised of a planar bilayer assembled into a sphere enclosing an aqueous solution. . (Illustrations drawn by T. Piñón)

The fluidity of the lipid bilayer gives vesicles their exceptional flexibility, permitting an amazing variety of shape transitions such as budding [Svetina 2002, Dobereiner 1993, Dobereiner 1995] and tubule formation [Yuan 2008, Hirst 2010, Li

2011]. Numerous shape configurations may be induced by temperature changes, contact mechanical stresses, or, of most interest to this dissertation, due to optical trapping forces. Lipid vesicles are extremely delicate, and determination of the viscoelastic properties of a single bilayer has been carried out using a variety of methods including atomic force microscopy on single cells [Lulevich 2006] and by manipulation of vesicles using micropipette aspiration [Dimova 2006, Rawicz 2000, Needham, *et al.* 2000], in which the membrane is pulled into a pipette using suction. These contact methods are highly localized and often cause artifacts in measurements. Focused-beam optical tweezer systems have also been used to locally probe the elasticity of GUVs [Dimova 2000], correlating the applied force to extension curves [Bendix 2011, Shitamichi 2009, Fygenson1997].

In this project, our artificial vesicles have an optically low-contrast interior solution ratio (5mM PEG8000/water) in comparison to the exterior solution (5 mM D-glucose/water). The ratio of these media refractive indices is defined as $m = n_{interior}/n_{exterior}$. A simple schematic of the desired engineered lipid vesicle is shown in Figure 4.3, with a low contrast ratio of $m \approx 1.005$. The dual-beam trapping experiments with vesicles described in later detail, are unique in that we demonstrate that stable trapping is not only relevant to higher contrast materials.

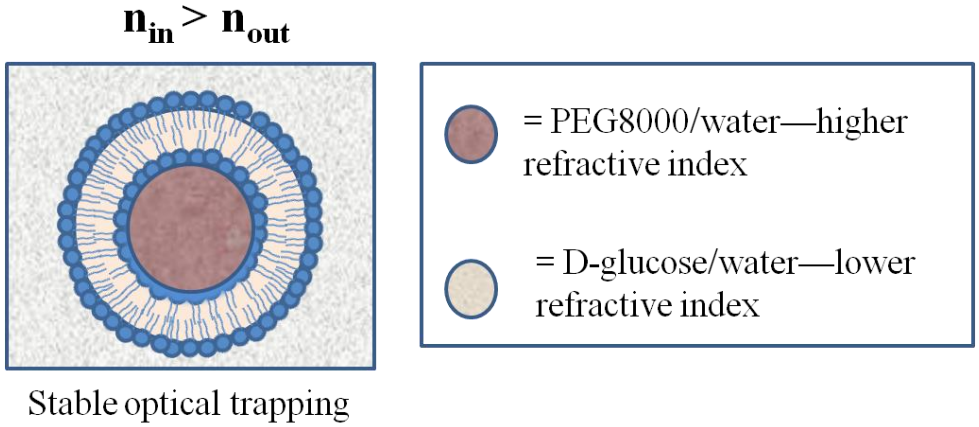

Fig 4.3. Schematic showing the final goal of engineering our lipid vesicles that encapsulate the water-soluble polymer, poly(ethylene) glycol (PEG 8000), and D-glucose-water solution as the exterior media. Despite the low optical contrast ratio between the two solutions, these synthesized vesicles may still be stably trapped. . (Illustration drawn by T. Piñón)

4.3 Trapping System Considerations

a. Temperature gradient within the trapping region

An important consideration for the optical trap design is choosing an appropriate laser wavelength to minimize heating effects to trapped biological particles. [Ebert 2007 and Wetzel 2011]. Due to the high water content of biological cells and the high water content of solutions used in our vesicle trapping experiments, this is an essential factor for us to further consider. Although the two diverging, Gaussian beams of the dual-beam trap exhibit lower light intensity than focused tweezer beams, one must still consider negative radiation heating effects [Ebert 2007, Bar-Ziv 1998]. Ebert, *et al.* devised a method to measure the temperature gradient within a fiber-based dual-beam trap using a combination of temperature sensitive and insensitive fluorophores. Their group found the center of the trap temperature change was $(13 \pm 2)\ ^{o}C/W$ for a trap wavelength of 1064 nm, and temperature scaled linearly with incident power [Ebert 2007]. Wetzel, *et al.* [2011] also quantified the temperature distribution in a fiber optical stretcher, but only tested applied powers of 0.5-1.5 W for a few seconds, yielding temperatures ranging from ≈ 47 to $68^{o}C$.

It appears that the trap wavelength does have a great influence on the maximum temperatures within the trap, with absorption coefficients that depend on wavelength [Ebert 2007, Jonasz 2007]. Looking at the absorption spectrum of water, we can see that our wavelength $\lambda \approx 980$ nm (or $\approx 10,200\ cm^{-1}$) does exhibit moderate absorption at $22^{o}C$ [Jonasz 2007]. For the sake of comparison, other two-beam research groups have carefully selected their trapping wavelengths of: 1064 nm for trapping red blood cells [Bareil 2009], 785 nm for red blood cells and mouse fibroblasts [Guck 2001], and 808 nm for stretching lipid vesicles [Solmaz 2012]. While our trap wavelength of 974 nm does not appear to be the most detrimental of wavelengths, future studies warrant testing to verify the estimated temperature changes [Ebert 2007] of up to $6^{o}C$ for the power range we use.

Additional research studies have evaluated cell viability in traps and have looked at ranges of intensity, wavelength, and time span of exposure that correlate to viability [Neuman 1999]. Viability of *E. coli* bacterial cells in optical tweezers have been investigated in the near-infrared range of $\lambda = 790$-1064 nm with continuous-wave (CW) lasers, with $\lambda = 970$ nm exhibiting the least damage (followed closely by 830 nm) on the cells [Neuman 1999 and Mirsaidov 2008]. Mirsaidov, *et al.* [2008] also conducted viability assays on *E. coli* and find $\lambda = 900$ nm causes the least photodamage. They indicate that cell viability in CW traps depends little on wavelength, but rather depends on peak power, suggesting a detrimental threshold of energy (5 J) for *E. coli* [Mirsaidov 2008].

b. Osmotic balance of solutes

Osmotic pressure balance is an important aspect to consider for fabricating spherical lipid vesicles. It is of critical importance for lipid vesicles to be spherical before

conducting any stretching experiments, mitigating the possibility of higher internal osmotic pressure relative to the external solution that induces vesicle shape stretched conformations (rather than optical forces). Ideally, true osmotic pressures should be measured experimentally in the medium, but due to limited laboratory resources, we have surveyed the literature to determine approximate values for existent osmotic pressures of vesicles used in optical stretching experiments. Before conducting optical trapping experiments, we visually inspect prepared lipid vesicles (5 mM PEG 8000-water interior, 5 mM D-glucose-water exterior) under the microscope to verify the vast majority of vesicles are spherical.

The addition of PEG is known to increase solution osmotic pressure [Arnold 1990]. As reported [Money 1989], the relationship between molarity and osmotic pressure (Π) is not linear for PEG molecular weights of 200 through 10,000, suggesting that PEG does not behave an ideal solute. It is thought that low concentrations, PEG may exist as an extended polymer chain in solution, but forms helical segments at higher concentrations [Money 1989]. Interestingly, low molecular weight PEGs appear to induce a greater Π than higher molecular weights [Money 1989]. Furthermore, PEG osmotic pressure is dependent upon temperature and concentration, with increased pressure with decreasing temperatures (range tested 10-40^{o}C) [Stanley 2003].

The determined osmotic pressure of 5 mM PEG 8000 (4 wt%) was estimated to be $\approx$ 0.25 atm at 23^{o}C, a factor of two greater than 5 mM D-glucose (0.09 wt%), as shown in Figure 4.4. The calculated osmotic pressure for PEG 8000 agrees with the work of [Stanley 2003], where the osmotic pressure at 20^{o}C for 5 wt% was measured to be 0.407 atm.

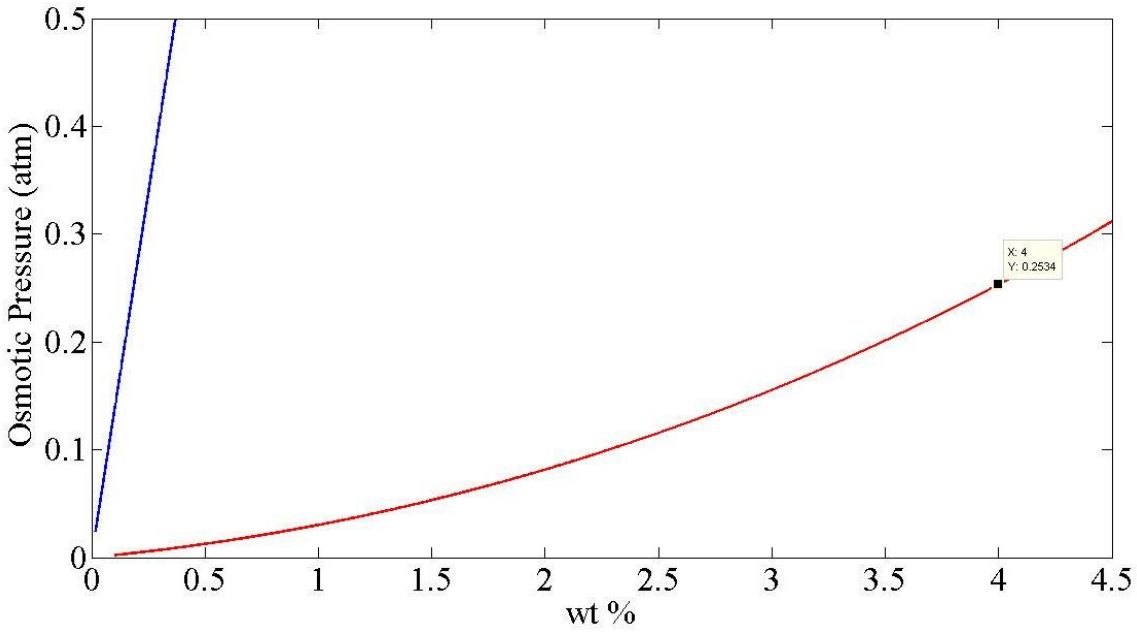

Fig 4.4. Plot showing estimated solution osmotic pressures for D-glucose/water solution (shown in blue), and pressures for PEG8000/water solution (shown in red). This data suggests the internal osmotic pressure of trapped vesicles may be a factor of 2 greater than the exterior osmotic pressure. (Matlab plot by T. Piñón)

4.4 Stretching Theory

For soft materials, optical forces induce an elongation of the particle along the beam axis with two counter-propagating, divergent Gaussian beams [Guck 2001, Guck 2000, Bareil 2006]. This "optical stretcher" technique (shown in Figure 4.5) is used to extract the elasticity of deformable microparticles.

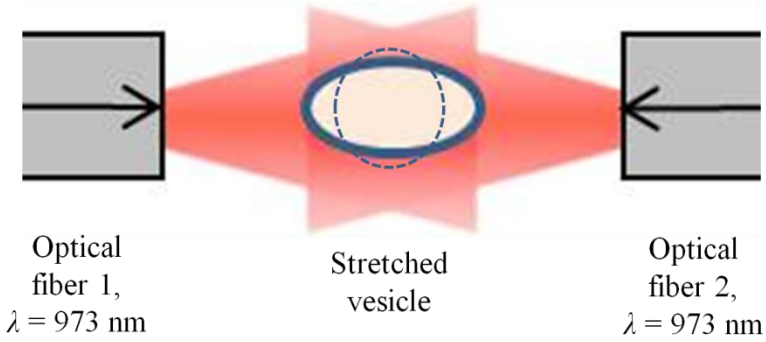

Fig 4.5. Depiction of an optically stretched vesicle in a fiber dual-beam trap. In a well-aligned trap, a stable trapping region exists in the center where both diverging laser beams overlap. At a certain incident light power, an initially spherical vesicle (dotted line) will stretch along the beam axis with higher power (solid line), and will continue to elongate with each power increase. This deformation behavior depends on the elastic strength of the vesicle. Drawing is not to scale. (Illustration drawn by T. Piñón)

The mechanisms at play may be explained with a combination of scattering and gradient forces [Guck 2000]. Transferred momentum to the particle surface induces surface stresses on the entire particle surface [Guck 2000, Bareil 2006, Solmaz 2012]. Following the work of Guck, calculations utilized in this work only consider the scattering forces along the beam axis [Guck 2000]. Incident trap light may be approximated as an infinite number of optical rays hitting the particle surface with energy E and a given momentum p_1, such that $p_1 = n_1E/c$, where n_1 is the refractive index of exterior solution, and c is the speed of light.

For a particle with a higher refractive index (n_2), the majority of light enters the particle due to refraction, with a small portion of light being reflected off the front surface. Light from each beam enters the particle gains momentum due to the particle's higher index of refraction, and loses momentum upon leaving the particle [Guck 2000]. This phenomenon is in agreement with the Abraham proposition for momentum of light in dielectrics [Ashkin 1973]. Likewise, a small portion of light is then reflected off the particle's back (opposite) surface. With a dual-beam trap, the second beam transfers twice the amount of momentum as one beam. This additive force acting on the front and back surfaces is essentially the scattering force along the beam axis [Guck 2000]. In response, light entering the dielectric, soft particle exerts a net outward force at the surface [Ashkin 1973], causing the particle to stretch. This observed stretching behavior is valid, assuming it has a higher refractive index contrast than the exterior solution.

4.5 Calculating On-Axis Stress for Stretched Vesicles

Our numerical calculations apply ray optics (RO) theory [Guck 2000, 2001] to determine on-axis stress imparted on the vesicle from both lasers (incident from left and

right). The RO regime is valid when the diameter of the trapped particle is much greater than the trap wavelength [Guck 2001, Van de Hulst 1981], such that $2\pi\rho/\lambda$ is >> 1.

When considering a divergent laser beam from the fiber hitting the front surface (left side) of the vesicle and for a given distance from the fiber end to vesicle center, the theoretical approach of Guck [2000, 2001] approximates an incident laser beam as a collection of individual rays. The behavior of these rays is dependent upon intensity (I) and momentum (p), and the direction through a given medium may be estimated using the RO approach [Guck 2000, 2001, Rancourt-Grier 2010]. Geometrical relationships are calculated for an incident light ray on the spherical surface at some incident angle, and some resulting angle from a light ray interacting with the back surface (right side) [Bareil 2006]. For an incident ray at an incident angle, α, the refraction angle, β, is governed by Snell's Law [Bareil 2006, Guck 2001] such that:

$$n_1 \sin(\alpha) = n_2 \sin(\beta) \qquad \text{(Eqn 4.1)}$$

As discussed by Bareil, *et al.* and Guck, *et al.* the resultant scattering stress is always perpendicular to the membrane surface regardless of the incident angle or rays that hit the from the outside or inside of the sphere [Bareil 2006 and Guck 2001]. Figure 4.6 shows ray tracings for an incident beam from the left, k, and the corresponding interactions with the "front" (left vesicle surface) and the "back" (right vesicle surface). More detailed geometrical derivations are found in [Guck 2001] as well as complementary work in [Bareil 2006] that express the parallel and perpendicular components of the optical force in terms of Q, the transferred momentum factor for the front and back surfaces.

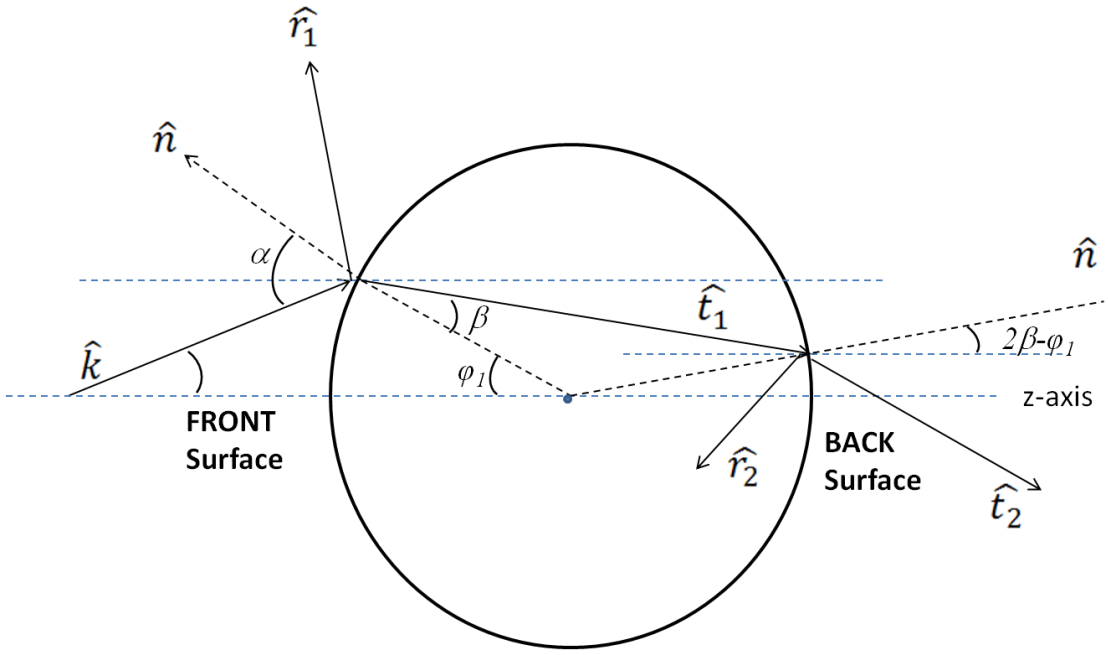

Fig 4.6. Schematic of incident (*k*), reflected (*r*) and transmitted (*t*) ray tracings for one beam (from the left) incident on a spherical object. A ray internally reflected (at some optimal angle) is denoted by $r_{2.}$ (Schematic modified from [Bareil 2006])

The stress exerted on the vesicle surface per unit area is expressed as [Guck 2001]:

$$\sigma_{front/back} = \frac{F}{\Delta A} = \frac{n_1 Q_{front/back}(\alpha) I(\alpha)}{c} \qquad \text{(Eqn 4.2)}$$

where σ is peak stress applied (front or back of vesicle); F is applied force per incident area (A); n_1 is the refractive index of surrounding liquid medium; Q is the radiation pressure efficiency factor related to the amount of transferred momentum; I is light intensity as a function of polar angle, α, relative to the beam axis; c is the speed of light. Again, in this Dissertation, we only consider the stress imparted along the beam axis, which is defined as normal incidence angle ($\alpha = 0^o$).

Following the work of Guck, *et al.* [Guck 2001,Guck 2000,Bareil 2007], we can consider the observed deformation, $\Delta\rho$, to determine vesicle elasticity [Guck 2001]. This model shows the relation between applied stress applied to the membrane and the resulting relative deformation (or strain). We can then determine the value, Eh, (where E is the Young's modulus and h is the membrane thickness), which expresses the rigidity of

the membrane. The vesicle is modeled as a thin, dielectric spherical shell with an initial (unstretched) radius ρ_o. The relative deformation is given by:

$$\frac{\Delta\rho}{\rho_o} = \frac{\rho_o \sigma_o}{Eh} \qquad \text{(Eqn 4.3)}$$

where σ_o is the peak stress along the beam axis [Guck 2001]. Peak stress is a known value, and is calculated using experimental parameters such as power, fiber separation, vesicle radius, and refractive index contrast. This model neglects possible multiple internal reflections within the particle, as later proposed by [Ekpenyong 2009].

This linear membrane theory for deformations of thin shells is valid for small strains <10% [Guck 2001]. Thin-shell modelling for cellular viscelasticity holds for cells without a cortical cytoskeleton, such as red blood cells [Ekpenyong 2009]. This deformation model follows the ray optics approach which is valid for spherical particles much larger than the wavelength of light. The criterion for the ray optics regime is valid when $2\pi\rho/\lambda >> 1$ [Guck 2001 and Van de Hulst 1981]. For our experiments, $2\pi\rho/\lambda \approx 19$-58, which indicates we are using an appropriate optical regime. As further described by Guck, *et al.* [2001], stretching of a membrane requires some amount of energy applied in the polar and meridional directions. These optical strains are derived from thin shell deformation theory, and as shown by Guck, *et al.* [2001], are proportional to the Young's modulus (E).

METHODS

4.6 Giant Lipid Vesicle Preparation

Giant lipid vesicles are prepared using the electroformation method [Angelova 1992]. Lipids were purchased from Avanti Polar lipids (Alabaster, AL). Lipid type DOPC (1,2-dioleoyl-*sn*-glycero-3-phosphocholine) was prepared in chloroform solution to a final lipid concentration of 10 mM.

The vesicle electroformation chamber consists of two conductive glass plates coated with indium tin oxide (ITO) (70-100 Ω/sq. surface resistivity, Sigma Aldrich). A few small droplets of lipid solution are deposited onto both conductive sides of the glass plates. The slides are then dried and kept under vacuum overnight to remove residual chloroform. A greased Teflon spacer ring (2 mm thick) is placed around the dried lipid films on one conductive glass slide, and a hydration solution is then added inside the ring. In this experiment we use 5 mM poly(ethylene) glycol (PEG) M.W. 8000 (Polysciences, Inc.) solubilized in water, giving a concentration of 4% PEG w/v. The solution is then

filtered through a membrane syringe filter (Millex-GV, 0.22 μm, Durapore membrane) to remove most dust particles and other undesirable particulates.

After initial preparations, the small, machined electroformation chamber is clamped together and connected to a function generator (Fluke 8846A) 2.5 V_{pp} (voltage peak-to-peak) at 5 Hz for ~15-21 hrs at 48-50°C (as illustrated in Figure 4.7a). After electroformation, the GUV solution is extracted from the chamber and dialyzed within a regenerated cellulose (RC) membrane (MWCO 15,0000, Spectrum Laboratories) to filter and replace the exterior PEG solution with 5 mM D-glucose/water solution. A schematic demonstrating the dialysis process is shown in Figure 4.7b. Dialysis is conducted with the membrane suspended within a 1 L beaker of the D-glucose/water solution, and is placed in the refrigerator (4 °C) for 5-7 hours.

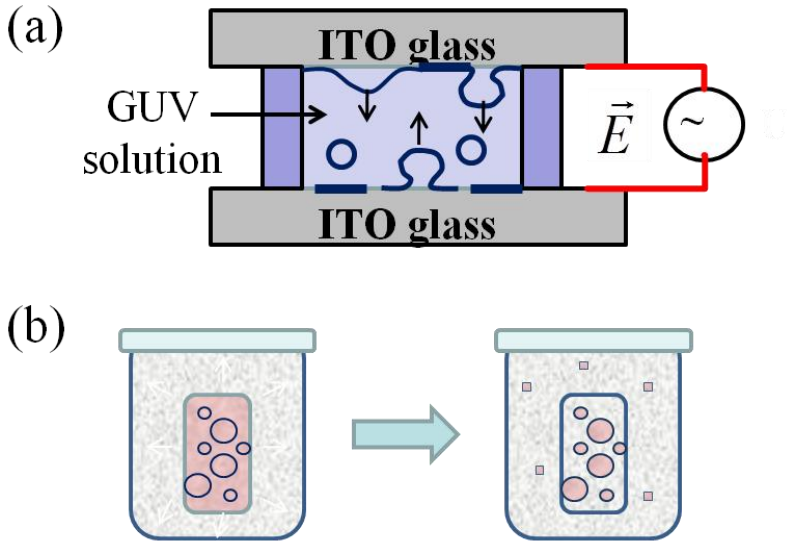

Fig 4.7. (a) Illustration of assembled electroformation chamber. Dried lipid film is deposited onto conductive sides of indium tin oxide (ITO) glass slides. Lipids are then rehydrated with desired buffer (e.g. 5 mM PEG8000/water solution). (b) Membrane dialysis is performed to achieve desired interior and exterior solutions. Exterior solution (e.g. 5 mM D-glucose/water) passes through membrane via diffusion, whereas the vesicles are too large to pass through the membrane. (Illustrations drawn by T. Piñón)

The electroformation technique tends to yield an assortment of unilamellar and multilamellar (multi-layered) vesicles. Multilamellar vesicles have a thicker membrane that is quite obvious during inspection with DIC microscopy. During optical trapping experiments, ideal vesicles can be drawn into the trapping region by gently pipetting fluid near the trap. The open-top chip platform is ideal for doing this. We used use a 1-10 μL pipette set to ≈ 8 μL, which is ideal for producing just enough circulation in the solution,

without creating turbulent flows. Thus, it is possible to perform stretching experiments on selected vesicles.

Trapped GUVs are visualized in real-time using differential interference contrast (DIC) microscopy (Leica DM2500 P, Meyer Instruments) with a water-immersion 63x microscope objective focused in the trapping region. Series of 5 stacked tiff images are acquired with a digital imaging camera (QImaging Retiga EXi FAST 1394) for each new power setting. Vesicles are initially trapped at minimal power of ≈30 mW from each fiber. The power is then increased by increments of 10-20 mW, holding each new power setting for 5-7 seconds before capturing a video. We measure deformation along the beam axis (major axis) of stretched vesicles using image processing software (NIH Image J).

RESULTS

4.7 Electroformed Vesicles

The electroformation process for forming lipid vesicles via an AC current yields optimal vesicle size (~2-20 μm diameter) with the majority of formed vesicles being unilamellar (single bilayer). Longer electroformation times yield larger vesicles, including a broader size distribution overall.

After electroformation of PEG vesicles (before dialysis), large aggregations of vesicles are visible with differential contrast microscopy (DIC) (Figure 4.8). The phenomenon of PEG-induced aggregation is described by [Arnold 1990] that explains the physical nature behind the interaction between PEG and phospholipid membranes. For PEG polymers of molecular weight 8000-1000, the polymer exists as random coil excluded at some distance from the bilayer surface, known as the depletion zone [Kuhl 1996]. When another vesicle approaches, the depletion zones overlap, increasing the free volume available and induces an effective attraction, called the depletion force. This depletion forces drives phopholipid aggregation [Arnold 1990, Kuhl 1996].

Furthermore, I have also observed a sizeable decrease in the number of vesicles per given volume, in comparison to forming vesicles in pure water.

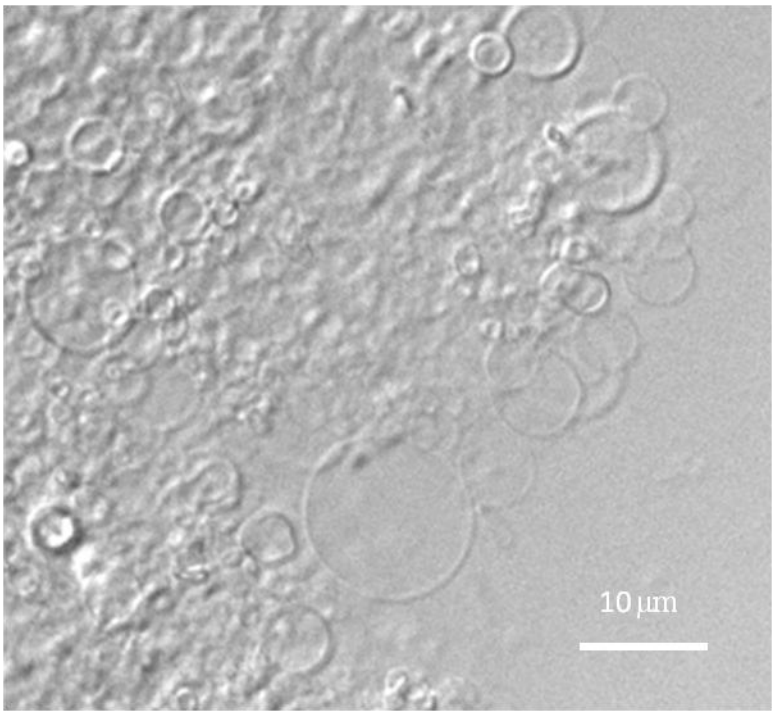

Fig 4.8. DIC microscopy image of PEG vesicles freshly extracted from the electroformation chamber. Large clusters of vesicles are typically observed, with a few individual vesicles in the vicinity.

4.8 Optical Stretching

As previously mentioned, the ratio between the beam radius, ω, at some distance away from the fiber end and the object's radius, ρ, is denoted as the ratio ω/ρ. As discussed in the work of Bareil 2009 and Guck 2001, among a list of factors, one attribute of a stable trap is when ω is larger than the radius, ρ, of the vesicle (or cell). This ratio also serves as a convenient factor for comparing stresses exerted when the fiber separation and vesicle radius is modified.

When deciding upon an ideal fiber core size, we may compare peak stress plots computed using Guck's method [2001] previously described in the section, "Calculating On-Axis Stress for Stretched Vesicles." In Figure 4.9, two fiber core sizes are computed: ω_o = 4.2 μm (a) and = 2.1 μm (b).

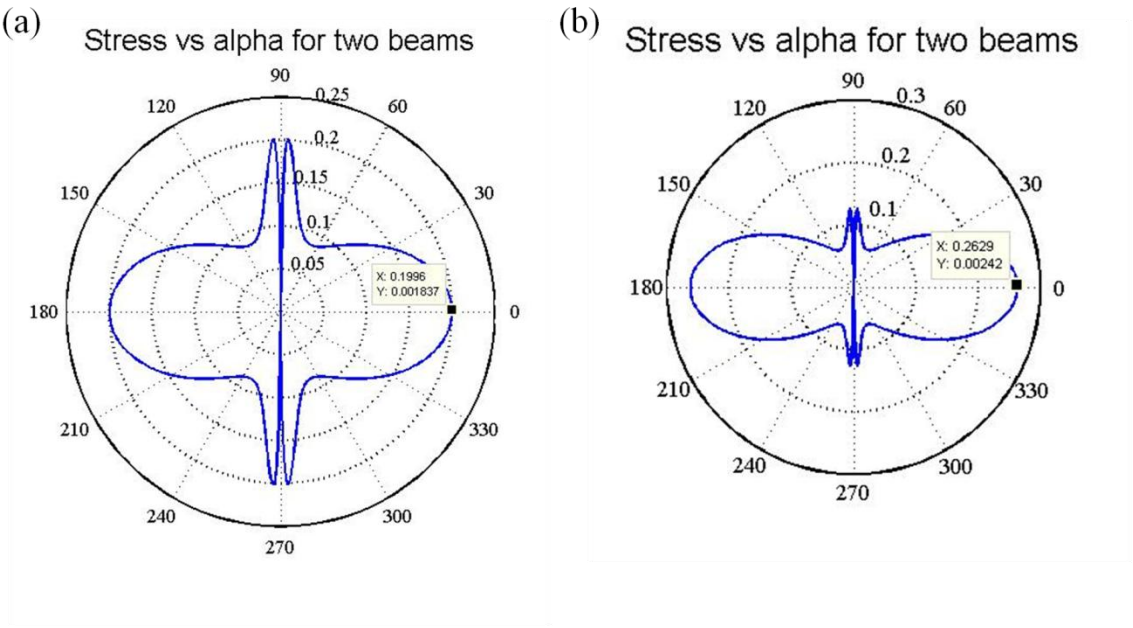

Fig 4.9. Examples of peak stress plot of a trapped 10 μm diameter GUV ($m \approx 1.005$). Incident power of 120 mW, fiber separation of 60 μm. (a) Larger fiber core radius of 4.2 μm ($\omega/\rho = 0.90$) yields an on-axis peak stress of 200 mN/m^2. (b) Smaller fiber core radius of 2.1 μm ($\omega/\rho = 0.79$) yields an on-axis peak stress of 263 mN/m^2. (Matlab plots by T. Piñón)

As observed in Fig 4.9, the differences in exerted peak stress for the smaller core fiber can be rather large (approximately 25% difference). Note in Figure 4.9, large spikes in stress are seen at increased angles from the beam axis, and are mentioned in [Lautenschlaeger 2011]. The normal stress on the membrane surface at these large angles diminishes as polar values approach 90^o (top pole) and 270^o (bottom pole), so these peaks are not physically observable. The magnitude of on-axis peak stress determines whether a vesicle will stretch at a given power. The calculations performed agree with our observations that in general, vesicles exhibit little or no stretching when the larger core fibers were used. We speculate that higher incident powers would then be required to see some of the more prominent deformations shown in Figure 4.10 with the smaller core (ω_0 = 2.1μm, Fiber Instrument Sales) trapping fibers.

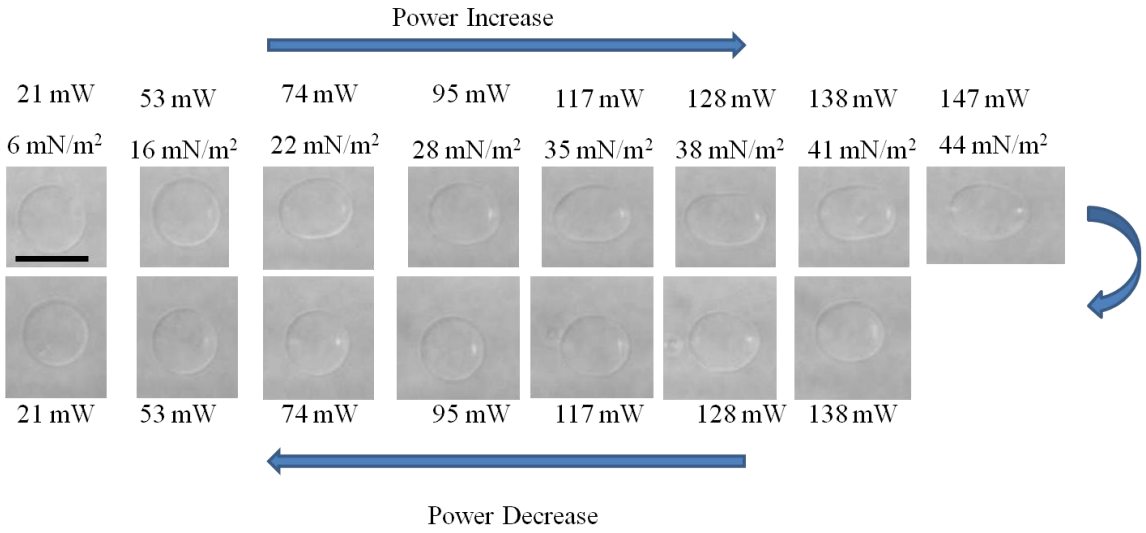

Fig 4.10. Differential interference contrast (DIC) image sequences of one optically stretched unilamellar vesicle cycled through increments of increasing then decreasing incident power. Corresponding peak stress (σ_o) values for each beam are also noted. Vesicle contains 5 mM PEG 8000 (4% PEG w/v) solubilized in water, with exterior solution of 5 mM D-glucose. Scale bar = 10 μm.

An interesting observation is that by continuing to apply stress to the membrane with higher optical powers, we observe nonlinear deformation which is characterized by a transverse indentation along the minor axis of the vesicle (90^o). In Figure 4.11, an example of nonlinear deformation occurring at an approximate applied peak stress of $\sigma_o \approx$ 33 mN/m^2 (power of 100 mW from each beam).

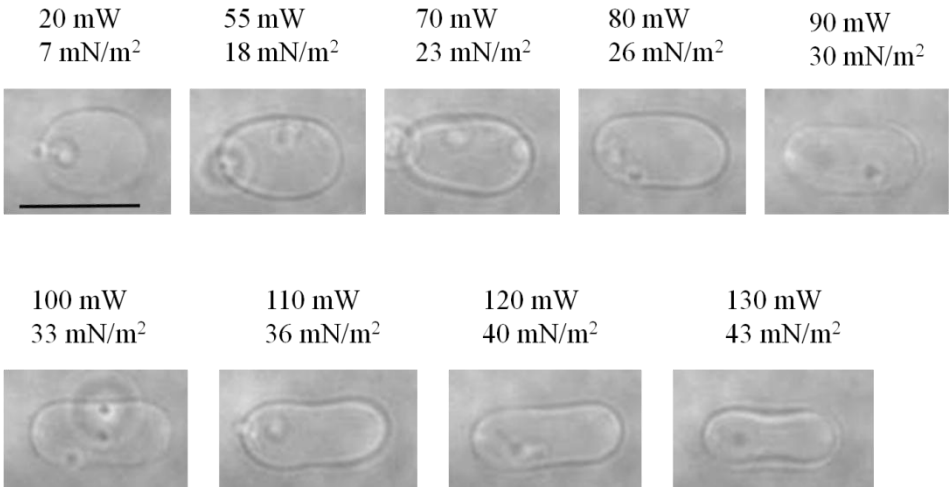

Fig 4.11. A stretched vesicle (ω/ρ = 1.8) demonstrating linear deformation up to σ_o = 33 mN/m^2, then transitions into nonlinear elongation along its major axis. Vesicle contains 5 mM PEG 8000 (4% PEG w/v) solubilized in water, with exterior solution of 5 mM D-glucose. Scale bar = 10 μm.

Figure 4.12 shows relative vesicle deformation along the major axis, and these measured values are plotted as a function of peak stress calculated from Equations 4.2 and 4.3. The horizontal error bars reflect a ±15% relative error which is predominantly due to uncertainty in the laser power in the trapping region. Vertical error bars reflect the statistical variations evident in the measured deformations. Linear fits reflect the range in which we observed linear stretching behavior.

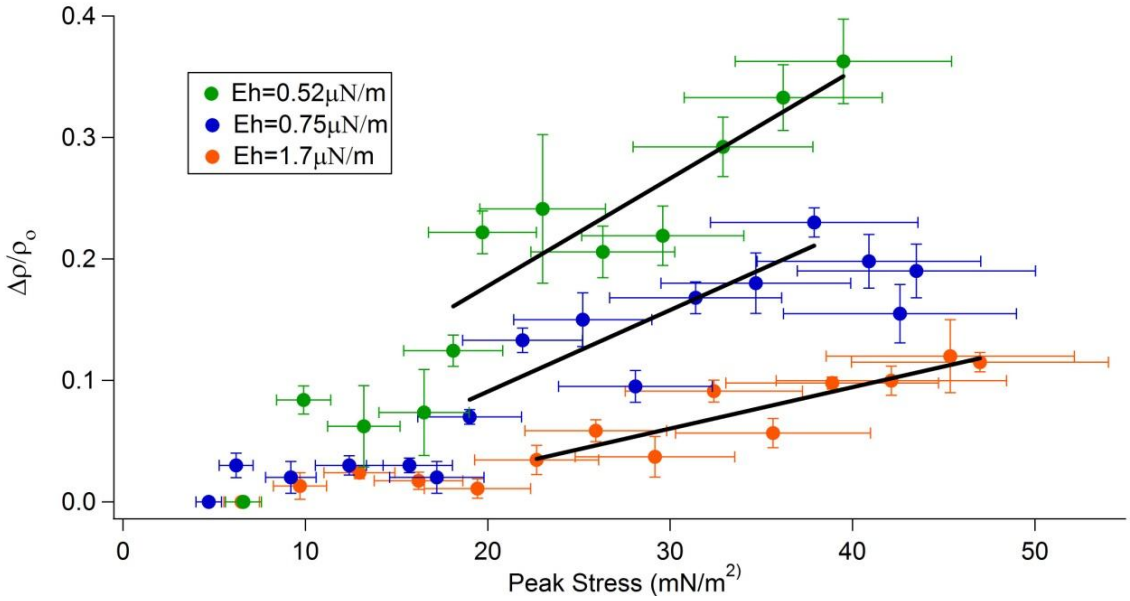

Fig 4.12. Examples of stretching behavior for different unilamellar vesicles. From this graph, we can observe stiffness variations in stretched vesicles. (Green dot) A vesicle of radius (ρ_o) = 4.6 μm yields $Eh \approx 0.52$ μN/m, $\omega/\rho = 1.85$. (Blue dot) A vesicle of radius (ρ_o) = 5.0 μm yields $Eh \approx 0.75$ μN/m, $\omega/\rho = 1.80$; (Orange dot) A vesicle of radius (ρ_o) = 5.8 μm yields $Eh \approx 1.7$ μN/m, $\omega/\rho = 1.49$.

One interesting observation for most stretching trials conducted is larger vesicles (d ≈ 10 μm) appear to exhibit a threshold behavior in which they do not deform until higher peak stresses of $\sigma_o \approx$ 18-47 mN/m^2 are applied. In contrast, smaller vesicles (d < 9 μm) can exhibit stretching as low as $\sigma_o \approx 7$ mN/m^2. Figure 4.13 shows three examples of stretching for three different vesicles whereby they are first trapped at low power (≈ 30-35 mW), then applied trapping power was incrementally increased (solid pink line, "Round 1") by steps of 10mW. After maximum laser power was reached, trapping power was incrementally decreased (solid black line, "Round 2"). Figure 4.13c shows one additional power increase round which was conducted in a similar fashion.

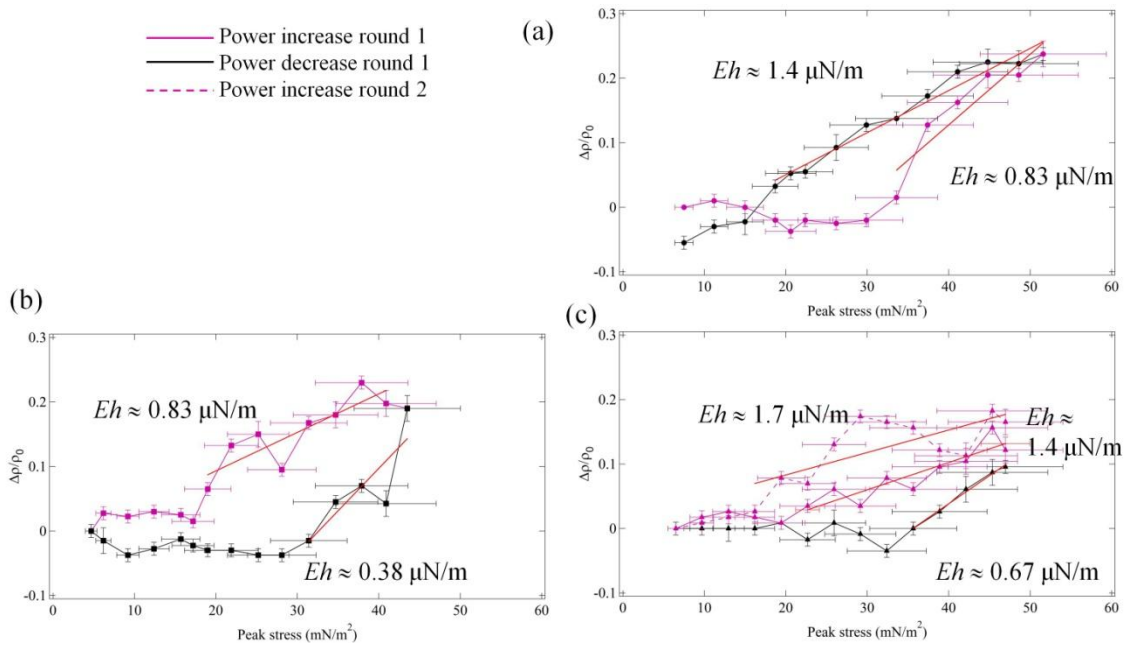

Fig 4.13. Hysteresis curves of three different stretched vesicles. (a) Relative deformation for a vesicle of radius (ρ_o) = 9.1 μm (ω/ρ = 0.9) yields Eh ≈ 0.52 μN/m; (b) Relative deformation for a vesicle of radius (ρ_o) = 5.0 μm (ω/ρ = 1.8) yields Eh ≈ 0.75 μN/m, ω/ρ = 1.80; (c) Relative deformation for a vesicle of radius (ρ_o) = 5.8 μm yields Eh ≈ 1.7 μN/m, ω/ρ = 1.5.

4.9 Comparison of Elastic Moduli to Biological Cells

Although published literature values for elastic moduli of biomembranes are somewhat limited, we can loosely compare our data to the elastic moduli values for red blood cells (RBCs) determined with a similar dual-beam stretcher configuration. Our determined Eh for vesicles is approximately two orders of magnitude less than red blood cells $Eh \approx 39 \pm 14$ μN/m [Guck 2001, Guck 2000] and $Eh \approx 54$ μN/m [Ekpenyong 2009]. Higher tension coefficients for red blood cells may be 4-24 times greater in comparison to vesicles [Popescu 2006], suggesting the spectrin network of the RBC cytoskeleton contributes to this difference. Furthermore, there is an expected increased stiffness for the osmotically swollen spherical RBCs used in these studies [Gompper 2008, Popescu 2006] which may also contribute to the difference.

When comparing the shear modulus of red blood cell membranes, the results often yield different values from dual-beam traps. For example, experiments involving optical tweezing RBCs with attached beads to the membrane, measured values ranged from (2.5 ± 0.4) μN/m [Henon 1999] to 200 μN/m [Sleep 1999]. The rather large discrepancies in values for shear moduli can be attributed to the different load techniques that could incite nonlinear deformations [Guck 2001]. For instance, optical tweezer experiments exert highly localized forces on the membrane.

4.10 Additional Observations of Trapped Vesicles

While setting out to perform more vesicle stretching assays, some additional interesting lipid membrane behavior was observed while a vesicle remained trapped. A series of images follow, which may give insight into future projects involving membrane instabilities such as budding and vesiculation (Figure 4.14).

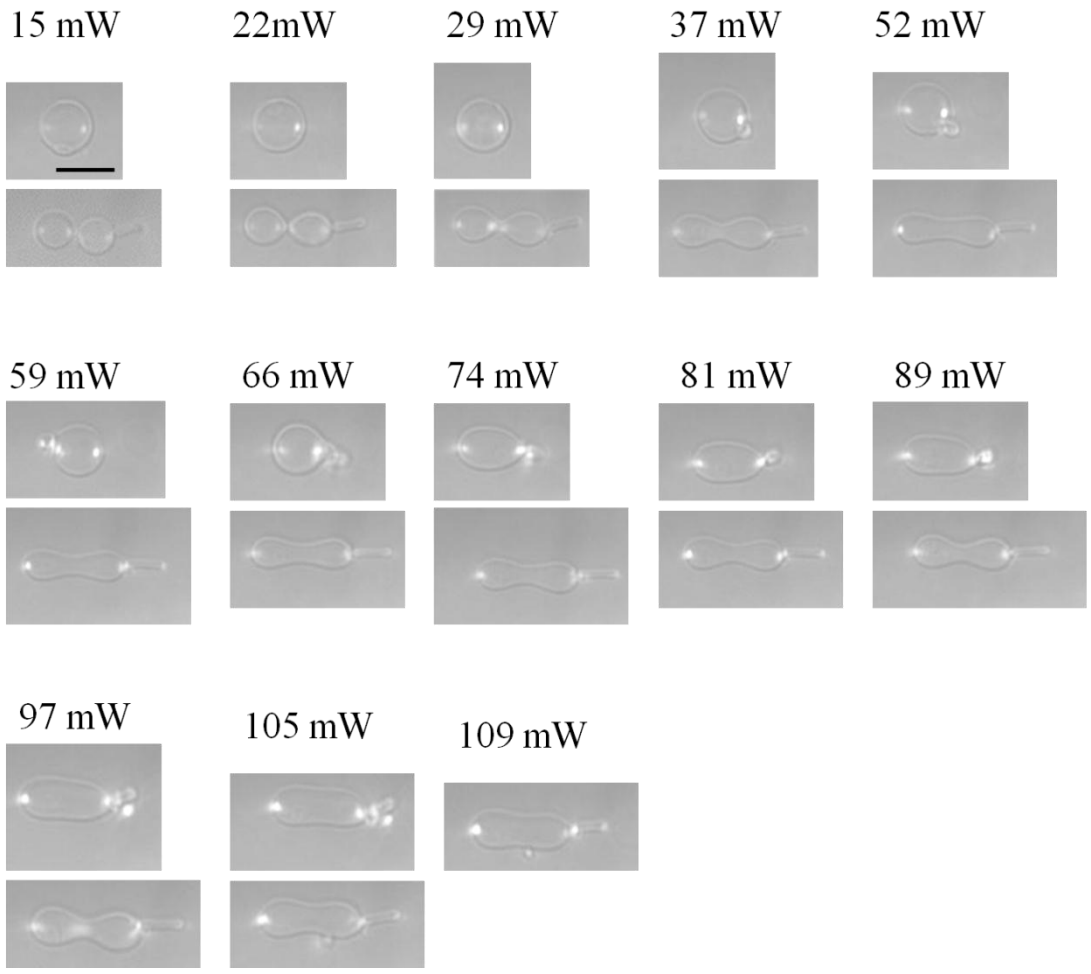

Fig 4.14. DIC images of a single vesicle undergoing one complete stretching cycle consisting of incrementally increasing then decreasing applied trapping power. The power increase series are shown immediately below the denoted powers. The power decrease series are shown below the power increase images for ease of comparison. Interestingly, after continuous elongation with increased powers, the vesicle membrane begins to indent in the center when the power is then decreased. The indentation becomes more pronounced until eventually the vesicle separates into two smaller vesicles (power 22 mW and 15 mW). Scale bar = 7 μm.

Upon closer observation of the initial, unstretched vesicle to the final separation into two vesicles, we compared the initial volume to the final volumes of each smaller vesicle (Figure 4.15). The vesicles were assumed to be spheres. It appears that the volumes were not conserved, but measurement error could be due to the two smaller vesicles not being in focus with one another in the microscope image. If the estimated error due to unfocused image in Figure 4.15b is ≈ 0.5 μm, estimated volumes for left and right vesicle could vary by ± 35 μm^3. The overlapping error range may actually suggest volume conservation, but additional studies would need to be conducted.

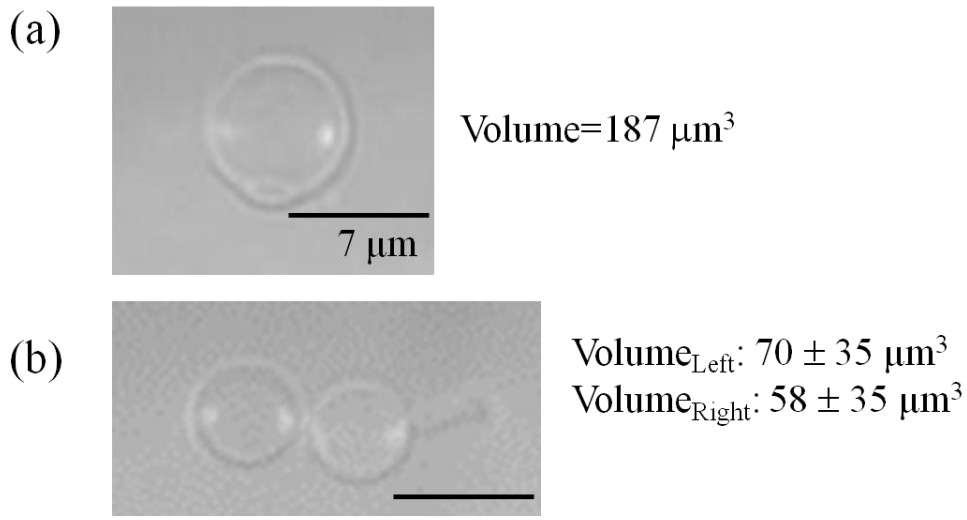

Fig 4.15. A closer observation of the stretched vesicle from Figure 4.14. Here, we compare the initial vesicle volume to the volume of the resulting separated vesicles (left and right).

Also, I have observed what appears to be the pearling instability effect (Figure 4.16), which to my knowledge, has only been observed with membranes surveyed with optical tweezers [Bar-Ziv 1998]. This instability arises from competition between the laser-induced tension and the bilayer bending elasticity [Bar-Ziv 1998].

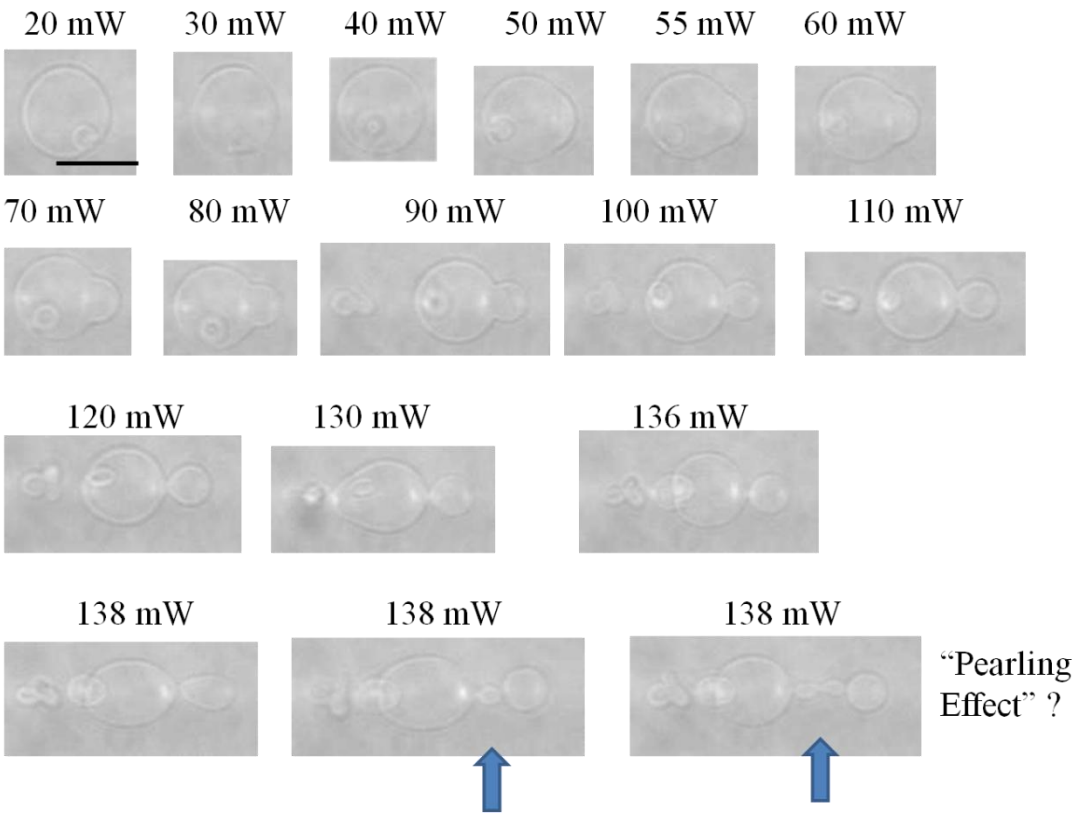

Fig 4.16. A trapped vesicle undergoing budding along the beam axis. The bud fully pinches off from the mother vesicle. At subsequent power increases, a small string of vesicles begins to form and the chain continues to elongate with time and maintaining the same trapping power. Scale bar = 10 μm.

DISCUSSION

The optical stretcher provides a unique and non-invasive method for probing biological cells and lipid vesicles to measure elasticity. We found optical forces conferred to trapped giant vesicles were sufficient for holding and exerting stresses to their surfaces. We assess deformation behavior of unilamellar (single bilayer) and multilamellar (multiple bilayers) with the ray optics approach, relating the measured deformation to exerted peak stresses $\sigma_o \approx$ 7-60 mN/m^2 along the beam axis. Within a linear regime of stretching response, Young's moduli values are proportional to the rigidity of the lipid membrane. Interestingly, we also observe that larger vesicles deform at greater threshold peak stresses.

Limitations of this model used for the dual-beam stretcher are the omission of multiple internal reflections within the stretched particle. Ekpenyong, *et al.*[2009] have further developed Guck's ray optics model with algorithms that account for focusing by the spherical interface of biological materials. Interestingly, modeling internal reflections

within a cell impart increased optical stress in localized regions of the membrane, which may account for the dramatic stretching we observe in our vesicle trapping experiments [Ekpenyong 2009]. A second limitation of the ray optics model is the need for careful selection of fiber separation and particle size. In comparison to the ray optics model, the cosine-squared distribution model is an accurate approximation for fiber separations 150 to 300 μm and cell radii of 3-6 μm [Ekpenyong 2009]. For larger cells, the cosine-squared model can underestimate cellular elasticity by 10-40%, whereas the ray optics approach would more accurately portray the optical stress profile [Ekpenyong 2009].

Stress calculations are dependent upon the geometry of a trapped particle. For soft bioparticles that deform under radiation forces in the dual-beam trap, nonspherical models more accurately simulate light scattering. Of special note, the research of Sosa-Martinez and Gutierrez-Vega [2009] explores the behavior of axial and transverse forces on a spheroidal dielectric trapped in a dual-beam configuration. Our observations of spherical vesicle deformation into an approximate spheroid suggests we must refine our current model and consider multiple reflections that give rise to several force vectors acting on the front and back vesicle surfaces [Solmaz 2012].

Our additional observations pertaining to the threshold stress required before linear vesicle stretching occurs appears to complement results of other research groups. We hypothesize this phenomenon is due to thermal undulations present in the low-tension regime that require "smoothing out" with slightly higher trap power before actual stretching begins. Micropipette aspiration experiments have explored the "low-tension regime" in which pipette pressurization first reduces thermal bending fluctuations of the fluid phase lipid membrane, causing the vesicle to initially become tense [Rawicz 2000, Dimova 2006]. Then with considerably more applied pressure, membrane stretching occurs [Rawicz 2000, Dimova 2002]. The concept of bending rigidity initially resisting vesicle deformation [Evans 1987] has implications for damping bending fluctuations with a fiber-based dual-beam trap, as demonstrated by the Malmstadt and Povinelli group [Solmaz 2012]. Their results suggest they are in the low stress regime as opposed to the higher stresses we apply to observe vesicle stretching ("area dilation" of lipid molecules) [Solmaz 2012]. Additionally, our stretching results also indicate the presence of a transition from linear to nonlinear stretching at increased trapping powers.

In our experiments, upon iterations of trapping power increase, then power decrease, vesicle behavior did show evidence of hysteresis. Further experimental runs will need to determine if the apparent hysteresis could be an artifact of misaligned trapping beams, or if the presence of membrane fluctuations necessitates a trapped vesicle to be gently pre-stretched before conducting the full range of stretching. Similar to discussions found in older published literature pertaining to micropipetting of vesicle membranes, we hypothesize that subvisible thermal fluctuations of the vesicle are initially smoothed in the low tension regime, followed by a higher tension regime of stretching [Rawicz 2000, Dimova 2002, Dimova 2006]. Pre-stressing of vesicles may ensure that small protrusions of the bilayer surface are smoothed out [Rawicz 2000].

Indeed, evidence of thermal fluctuation reduction has also been observed with subjecting vesicles to tension from optical tweezing [Bar-Ziv 1995] and dual-beam trapping, in which damping bending fluctuations (rather than stretching) is observed [Solmaz 2012]. For this reason, we suspect pre-stretching vesicles could make the elongation and contraction runs more equivalent to one another. This would diminish the asymmetric stretching behavior and irreversible energetic transformations that suggest the deformation is not elastic.

The presence of hysteretic behavior observed in biology appears to be controversial. No applicable literature was found that specifically pertained to the absence/presence of hysteresis of lipid vesicles probed with a dual-beam trap. Even so, there is limited information about purely optical methods (as opposed to AFM measurements) that investigate hysteresis in biological cells. Guck, *et al.* [2001] investigated the elasticity of fibroblast cells with the dual-beam optical stretcher, but the cells did not exhibit any hysteresis when stretched. However, another research group conducting optical tweezing experiments with RBCs found that hysteretic shape behavior only appeared when a cell is trapped for several minutes at high power, causing an eventual deleterious effect on cell elasticity [Henon 1999]. Yet a different configuration of tether-based optical tweezing of fibroblasts at low tension showed almost no hysteresis, suggesting the cells behave largely elastically [Nawaz 2012]. It is speculated whether the validity of this ideal elastic behavior breaks down in part with higher stretching. Other questions that remain unanswered are whether incident thermal effects from the trap beams over time could drive membrane hysteresis, and whether the observations hold true of other research groups that investigate cell elasticity rather than vesicles.

The fluid-like state quality of the phospholipid bilayer may give rise to viscoelastic behavior that varies with rate of applied load. It is of interest to conduct time-dependent vesicle stretching studies to determine if stretching behavior changes depending on the rate at which we apply optical stress. The viscosity differences between the interior and exterior vesicle solutions, and the nature of solubilized PEG 8000 polymer could give rise to asymmetric membrane stretching behavior. If so, these studies could provide insight for the observed hysteresis response with stress loading and unloading cycles.

In general, lipid bilayers are predominantly viscous (i.e. Newtonian) [Tasso 2013] since they are coupled to viscous fluids such as water. However, rheology experiments that probe lipid membrane mechanical properties are not without debate, with some recent results suggesting membrane viscoelasticity is not significant [Tasso 2013, Harland 2010]. Earlier experiments reveal viscoelastic [Levine 2002] and linear viscoelastic behavior of vesicles [deHaas 1997]. Nevertheless, it is speculated whether the role of the bilayer separating two fluids of differing viscosities [Levine 2002] such as PEG8000 and D-glucose aqueous solutions used in our experiments aids in driving the macroscopic plastic deformations we observe. The role of lipid membrane viscosity is an

interesting aspect that may explain the transition from linear vesicle stretching into the regime of distinct vesicle budding seen at the highest stretching powers.

In regards to temperature gradients within the trap, we anticipate there is minimal to moderate influence due to temperature on the lipid bilayer. The mechanical properties of lipid bilayers have a strong dependence on temperature. Although our trapping experiments are well within the liquid phase for DOPC vesicles, slight temperature increases could cause trapped vesicles to become softer when stretched (decreased Young's modulus). Our vesicles are comprised of DOPC lipid which has a liquid-to-gel phase transition at -20^{o}C.

One future direction of this project is to characterize the temperature profile near the trapping region. The methods of Ebert, *et al.* [2007] are attractive means for us to experimentally determine temperature gradients surrounding the trapping region, and have some basis for comparison. Ebert, *et al.* [2007] devised a method to measure the temperature distribution profiles in real-time within a fiber-based dual-beam trap using a combination of temperature sensitive Rhodamine B dye and the temperature insensitive fluorophore, Rhodamine 110, for the reference reading. Here, the dependence of fluorescence on temperature is utilized to calculate ratios of intensity profiles obtained using a confocal laser-scanning microscope [Ebert 2007]. The use of a thermal imaging camera could also be of interest to us.

Another aspect to consider is the effect of lamellarity on measured Young's moduli. We expect unilamellar vesicles will yield lower Young's moduli in comparison to multilamellar vesicles due to the response of multiple bilayers undergoing stress.

CONCLUSION

In this chapter we demonstrate successful optical trapping and stretching lipid vesicles on a simple, compact plexiglass trapping platform. We show, for the first time, trapping of low-contrast ($m \approx 1.005$) lipid vesicles in solution. Our trapping design affords a non-contact, non-invasive technique for surveying the range of linear and non-linear elastic regimes with low contrast lipid membranes. Contrary to other techniques, the versatile dual-fiber trapping design provides a controlled, purely optical method for applying femtonewton-range forces over an extended membrane surface. These studies provide a foundation for exploring the forces required for various membrane conformational changes relevant to cellular processes such as vesiculation and budding

APPENDIX

I. Mie scattering coefficient program (Mätzler 2002, with minor modifications by Tessa Piñón)

#a) This program utilizes a_n, b_n, c_n, and d_n to calculate scattering coefficient values

```
%Mie scattering coefficient program calculations are from Christian Matzler's "MATLAB
%Functions for Mie Scattering and Absorption" paper-Research Report no.
%2002-08. June 2002.

%I have done minor modifications to Mätzler's original code to fit the
%parameters of our experiment


function result = tessamie_abcd6um(m, x)

%For 6.0 um diameter polystyrene microsphere
r = 3.0E-6;
x = (2*pi*r*1.33)/980E-9;
m = 1.59/1.33;

%Statement below satisfies requirement for an and bn mie coefficients: that
%they are 0 for x = 0 and are continuous functions of x. They are 0 for
%m=1 and continuous functions of m [Van de Hulst p.136].


%if x==0                % To avoid a singularity at x=0
   %result=[0 0 0 0 0 1.5];
   % This is the normal situation

nmax=round(2+x+4*x.^(1/3));  %Termination for n value [Bohren & Huffman]
n=(1:nmax);
nu = (n+0.5); %denotes half-integral order
z=m.*x; %given argument
m2=m.*m;

%Spherical Bessel functions defined-(Bohren & Huffman, p. 86)
sqx= sqrt(0.5*pi./x); sqz= sqrt(0.5*pi./z);
```

```
bx = besselj(nu, x).*sqx;
bz = besselj(nu, z).*sqz;
yx = bessely(nu, x).*sqx;

hx = bx+i*yx;

b1x=[sin(x)/x, bx(1:nmax-1)];
b1z=[sin(z)/z, bz(1:nmax-1)];

y1x=[-cos(x)/x, yx(1:nmax-1)];

h1x= b1x+i*y1x;

ax = x.*b1x-n.*bx;
az = z.*b1z-n.*bz;

ahx= x.*h1x-n.*hx;

an = (m2.*bz.*ax-bx.*az)./(m2.*bz.*ahx-hx.*az);
bn = (bz.*ax-bx.*az)./(bz.*ahx-hx.*az);
cn = (bx.*ahx-hx.*ax)./(bz.*ahx-hx.*az);
dn = m.*(bx.*ahx-hx.*ax)./(m2.*bz.*ahx-hx.*az);
result=[an; bn; cn; dn];

   n1=nmax-1;
   n=(1:nmax);cn=2*n+1; c1n=n.*(n+2)./(n+1); c2n=cn./n./(n+1);
   x2=x.*x;
   f=tessamie_ab6um(m,x);          %an = first row, bn = second row
   anp=(real(f(1,:))); anpp=(imag(f(1,:)));
   bnp=(real(f(2,:))); bnpp=(imag(f(2,:)));
   g1(1:4,nmax)=[0; 0; 0; 0]; % displaced numbers used for
   g1(1,1:n1)=anp(2:nmax);    % [asymmetry parameter, Bohren & Huffmaan, p. 120]
   g1(2,1:n1)=anpp(2:nmax);
   g1(3,1:n1)=bnp(2:nmax);
   g1(4,1:n1)=bnpp(2:nmax);

   % Extinction Coefficient
   dn=cn.*(anp+bnp);
   q=sum(dn);
   qext=2*q/x2;

   % Scattering Coefficient
   en=cn.*(anp.*anp+anpp.*anpp+bnp.*bnp+bnpp.*bnpp);
   q=sum(en);
```

```
qsca=2*q/x2;
qabs=qext-qsca;

% Backscattering -- [Bohren & Huffman, p. 122]
fn=(f(1,:)-f(2,:)).*cn;
gn=(-1).^n;
f(3,:)=fn.*gn;
q=sum(f(3,:));
qb=q*q'/x2;

asy1=c1n.*(anp.*g1(1,:)+anpp.*g1(2,:)+bnp.*g1(3,:)+bnpp.*g1(4,:));
asy2=c2n.*(anp.*bnp+anpp.*bnpp);
asy=4/x2*sum(asy1+asy2)/qsca;
qratio=qb/qsca;


qpr = qext-(asy*qsca);


Table = [qext',  qsca',        qabs',                    qb',    asy'      qratio    qpr'];
disp('')
disp('For 6.0um diameter dielectric polystyrene microsphere')
disp('    Qext      Qsca      Qabs    Qb   <cos(theta)> Qb/Qsca    Qpr')
disp('')
disp(Table)
disp('')



#b)

function result = tessamie_ab6um(m,x)

% Computes a matrix of Mie Coefficients, an, bn,
% of orders n=1 to nmax, for given complex refractive-index
% ratio m=m'+im'' and size parameter x=k0*a where k0= wave number in ambient
% medium for spheres of radius a;
% Eq. (4.88) of Bohren and Huffman (1983)
% using the recurrence relation (4.89) for Dn on p. 127 and
% starting conditions as described in Appendix A.
% C. Mätzler, July 2002

r = 3.0E-6;
x = (2*pi*r*1.33)/980E-9;
m = 1.59/1.33;
```

```
z=m.*x;
nmax=round(2+x+4*x.^(1/3));
nmx=round(max(nmax,abs(z))+16);

n=(1:nmax); nu = (n+0.5);

sx=sqrt(0.5*pi*x);

px=sx.*besselj(nu,x);
p1x=[sin(x), px(1:nmax-1)];


chx=-sx.*bessely(nu,x);

ch1x=[cos(x), chx(1:nmax-1)];

gsx=px-i*chx; gs1x=p1x-i*ch1x;

dnx(nmx)=0+0i;

for j=nmx:-1:2      % Computation of Dn(z) according to (4.89) of Bohren
& Huffman (1983)
   dnx(j-1)=j./z-1/(dnx(j)+j./z);
end;
dn=dnx(n);          % Dn(z), n=1 to nmax
da=dn./m+n./x;
db=m.*dn+n./x;

an=(da.*px-p1x)./(da.*gsx-gs1x);
bn=(db.*px-p1x)./(db.*gsx-gs1x);

result=[an; bn];
```

II. MATLAB spring constant program. Program based from Constable (1993).

```
%This program calculates the spring constant "k" (theoretical) for a
%trapped 10um diameter polystyrene microsphere in water. This program
%is based from Constable's (1993) article--Eq. 2.

%Qpr value calculated using Mätzler's Mie scattering coefficient MATLAB
%program (separate from this code)


%For 10.0 um diameter polystyrene microspheres
a = (2*(5.0E-6)^2)/3E8; %Incident cross-sectional area
q = 0.2013; %Qpr
w = 5E-6;   %Gaussian beam waist
n = 980E-9; %Laser wavelength
d = (pi*(w)^2)/n;


%Output power (W) of counter-propagating beams
p1 = 69E-3; %Left beam
p2 = 45E-3; %Right beam

s = 77E-6;  %Fiber separation

k1 = (16*(pi^2)*a*s);
k2 = (p1*q*(w^2))/((n^2)*((s^2)+(4*(d^2)))^2);
k3 = (p2*q*(w^2))/((n^2)*((s^2)+(4*(d^2)))^2);
k = k1*(k2+k3) %Theoretical spring constant
```

III. MATLAB Scattering Force Program. Program based from Constable (1993).

```
%This program calculates the net scattering force on a trapped 10um
% sphere in water. This program is based from Constable's (1993)
%article--Eqn. 1.

%Qpr value calculated using Matzler's Mie scattering coefficent MATLAB
%program (separate from this code)

%For 10.0 um diameter polystyrene microsphere
a = (2*(5.0E-6)^2)/3E8; %Incident cross-sectional area
q = 0.2013; %Qpr (radiation pressure coefficient)
w = 5E-6; %Gaussian beam waist
n = 980E-9; %Laser wavelength
d = (pi*(w)^2)/n;

s = 77.0E-6;

%Output power (W) of counter-propagating beams
p1 = 69E-3; %Left beam
p2 = 45E-3; %Right beam

z = 37E-6; %Displacement of microsphere relative to trap center

f1 = ((a*p1*q)/(w^2))/(1+((d^-2)*((s/2)+z)^2)); %Left scattering force
f2 = ((a*p2*q)/(w^2))/(1+((d^-2)*((s/2)-z)^2)); %Right scattering force
```

```
f = f1

f = f2

f = f1-f2 %Net scattering force
```

IV. Code computes exerted stress on a stretched spherical particle. Code is based from [Guck 2005, Bareil 2006].

```
%Guck trial
clear all;
close all;

onebeam=0;

eps=0.000001;
n1=1.3289;
n2=1.3369;
n=n2/n1;
p=80E-3; %power in W from each beam

guvdiam=10E-6;
rho=guvdiam/2;

sep=60E-6; %fiber separation in meters
z=sep/2;

w0 = 2.1E-6; %beam radius from fiber
wn=974E-9; %trap wavelength

 alpha=eps-pi/2:0.01:pi/2;
beta =asin(sin(alpha)/n);
```

```
%r =rho.*sin(alpha-asin(rho.*sin(alpha)./z)); %jay's expression


w=w0.*sqrt(1+(z*wn/(pi*n1*(w0)^2))^2);


beamtoparticlesize=w/rho


Qfrontx=1+(R(alpha,beta).*cos(2*alpha))-n*(1-R(alpha,beta)).*cos(alpha-beta);

%Qfronty=R(alpha,beta).*sin(2.*alpha)+(n*(1-R(alpha,beta)).*sin(alpha-beta));

Qfronty=-R(alpha,beta).*sin(2.*alpha)+(n*(1-R(alpha,beta)).*sin(alpha-beta));


Qbackx=(1-R(alpha,beta)).*(n.*cos(alpha-beta)+  (n.*R(beta,alpha).*cos((3*beta)-alpha)-
(1-R(beta,alpha)).*(cos((2.*alpha)-(2.*beta)))));

%Qbacky=(1-R(alpha,beta)).*(-n.*sin(alpha-beta)+(n.*R(beta,alpha).*sin((3.*beta)-
alpha)-(1-R(beta,alpha)).*sin((2.*alpha)-(2.*beta))));

Qbacky=(1-R(alpha,beta)).*(-n.*sin(alpha-beta)+(n.*R(beta,alpha).*sin((3.*beta)-
alpha)+(1-R(beta,alpha)).*sin((2.*alpha)-(2.*beta))));


Qbackmag=sqrt((Qbackx.^2)+(Qbacky.^2));

Qfrontmag=sqrt((Qfrontx.^2)+(Qfronty.^2));


Qtot=Qfrontmag+Qbackmag;


PHIfront=atan(Qfronty./Qfrontx);%phi1

PHIback=atan(Qbacky./Qbackx); %(2*beta)-phi1


r=rho*sin(alpha-asin(rho*sin(alpha)/z));


inten=(2.*p)./(pi.*(w.^2)).*exp(-2.*((r./w).^2));
```

```
stressfront=(n1.*Qfrontmag.*inten)./c;
stressback =(n1.*Qbackmag.*inten)./c;

figure(1)
if onebeam==0
    figure(1)
    polar(alpha+pi,stressfront+stressback)
    title('Stress vs alpha for two beams: GUV','FontSize',20)

    hold
    polar(alpha,stressback+stressfront)
else
    polar(alpha,stressback)
    title('Stress vs alpha for one beam','FontSize',20)

    hold
    polar(alpha,-stressfront)
end

%plot(r,exp((-2.*(rho^2).*(sin(PHIfront)).^2)./(w^2)))
```

REFERENCES

A-Hassan, E., W.F. Heinz, M.D. Antonik, N.P. D'Costa, S. Nageswaran, C-A Schoenenberger, and J.H. Hoh. 1998. Relative microelastic mapping of living cells by atomic force microscopy. *Biophysical Journal* 74 (3) (03/01): 1564-78.

Alessi, M. L., A.I. Norman, S.E. Knowlton, D.L. Ho, and S.C. Greer. 2005. Helical and coil conformations of poly(ethylene glycol) in isobutyric acid and water. *Macromolecules* 38 (22): 9333-40.

Allard, F. C. 1990. Fiber-optic splices, connectors, and couplers. In *Fiber optics handbook.*, eds. P. Morra, E. Vezzoni, 3.12McGraw-Hill Publishing Company.

Angelova, M. I., S. Soleau, Ph. Meleard, J.F. Faucon, and P. Bothorel. 1992. Preparation of giant vesicles by external AC electric fields. kinetics and applications. *Progress in Colloid & Polymer Science* 89 : 127-31.

Arnold, K., O. Zschoernig, D. Bartherl, and W. Herold. 1990. Exclusion of poly(ethylene glycol) from liposome surfaces. *Biochimica Et Biophysica Acta* 1022 : 303-10.

Ashkin, A. 1970. Atomic-beam deflection by resonance-radiation pressure. *Physical Review Letters* 25 (19): 1321-4.

Ashkin, A., and J.M. Dziedzic. 1973. Radiation pressure on a free liquid surface. *Physical Review Letters* 30 (4): 139-42.

Ashkin, A., J.M. Dziedzic, J.E. Bjorkholm, and S. Chu. 1986. Observation of a single-beam gradient force optical trap for dielectric particles. *Optics Letters* 11 (5): 288-90.

Ashkin, A. 1970. Acceleration and trapping of particles by radiation pressure. *Physical Review Letters* 24 (4): 156-9.

Ashkin, A., J.M. Dziedzic, and T. Yamane. 1987. Optical trapping and manipulation of single cells using infrared laser beams. *Nature* 330 (6150) (Dec 24-31): 769-71.

Avanti Polar Lipids, Inc. DOPC [cited 01/26/2013]. Available from http://avantilipids.com/index.php?option=com_content&view=article&id=231&Itemid=207&catnumber=850375

Bareil, P. B., and Y. Sheng. 2006. Local stress distribution on the surface of a spherical cell in an optical stretcher. *Optics Express* 14 (25): 12503-9.

Bareil, P. B., Y. Sheng, and A.E. Chiou. 2009. Theoretical prediction for cell deformation in the optical traps. Paper presented at SPIE Proceedings 7400, Optical Trapping and Optical Micromanipulation VI, San Diego, CA.

Bareil, P. B., Y. Sheng, Y-Q Chen, and A. Chiou. 2007. Calculation of spherical red blood cell deformation in a dual-beam optical stretcher. *Optics Express* 15 (24): 16029-34.

Barth, H. G. 1984. Modern methods of particle size analysis, vol. 73. In , eds. P. J. Elving, J.D. Winefordner and I.M. Kolthoff. Hoboken, NJ: John Wiley & Sons, Inc.

Bar-Ziv, R., T. Frisch, and E. Moses. 1995. Entropic expulsion in vesicles. *Physical Review Letters* 75 (19): 3481-4.

Bar-Ziv, R., E. Moses, and P. Nelson. 1998. Dynamic excitations in membranes induced by optical tweezers. *Biophysical Journal* 75 (1) (7): 294-320.

Baumgart, T., S. Das, W.W. Webb, and J.T. Jenkins. 2005. Membrane elasticity in giant vesicles with fluid phase coexistence. *Biophysical Journal* 89 (2): 1067-80.

Bellini, N., K.C. Nishnubhatla, F. Bragheri, L. Ferrara, P. Minzioni, R. Ramponi, I. Cristiani, and R. Osellame. 2010. Femtosecond laser fabricated monolithic chip for optical trapping and stretching of single cells. *Optics Express* 18 (5): 4679-88.

Bendix, P. M., and L.B. Oddershede. 2011. Expanding the optical trapping range of lipid vesicles to the nanoscale. *Nano Letters* 11 (12): 5431-7.

Black, B. J., and S.K. Mohanty. 2012. Fiber-optic spanner. *Optics Letters* 37 (24): 5030-2.

Blair, D., and E. Dufresne. The matlab particle tracking code repository. 2008 [cited 01/23 2013]. Available from http://physics.georgetown.edu/matlab/ (accessed 11/1/2009).

Bohren, C. F., and D.R. Huffman. 1998. *Absorption and scattering of light by small particles*. New York: Wiley.

Burns, J. A., P.L. Lamy, and S. Soter. 1979. Radiation forces on small particles in the solar system. *Icarus* 40 : 1-48.

Chang, K. -A, H. Lim, and C.B. Su. 2002. A fibre optic fresnel ratio meter for measurements of solute concentration and refractive index change in fluids. *Meas. Sci. Technol.* 13 : 1962-5.

Cherney, D. P., T.E. Bridges, and J.M. Harris. 2004. Optical trapping of unilamellar phospholipid vesicles: Investigation of the effect of optical forces on the lipid membrane shape by confocal-raman microscopy. *Analytical Chemistry* 76 (17) (09/01): 4920-8, http://dx.doi.org/10.1021/ac0492620.

Constable, A., J. Kim, J. Mervis, F. Zarinetchi, and M. Prentiss. 1993. Demonstration of a fiber-optical light-force trap. *Optics Letters* 18 (21): 1867-9, http://ol.osa.org/abstract.cfm?URI=ol-18-21-1867.

Cran-McGreehin, S., T.F. Krauss, and K. Dholakia. 2006. Integrated monolithic optical manipulation. *Lab on a Chip* 6 (9): 1122-4.

CVI MellesGriot. Dispersion equations for optical materials, appendix. [cited 01/23 2013]. Available from http://www.cvimellesgriot.com/products/Documents/Catalog/Dispersion_Equations.pdf.

Daimon, M., and A. Masumura. 2007. Measurement of the refractive index of distilled water from the near-infrared region to the ultraviolet region. *Applied Optics* 46 (18): 3811-20.

De Haas, K.H., C. Blom, D. van den Ende, M.H.G. Duits, B. Haveman, and J. Mellema. *Langmuir* 13 (25):6658-6668.

Del Villar, I., C.R. Zamarreno, M. Hernaez, F.J. Arregui, and I.R. Matias. 2010. Lossy mode resonance generation with indium-tin-oxide-coated optical fibers for sensing applications. *Journal of Lightwave Technology* 28 (1): 111-7.

Dimova, R., B. Pouligny, and C. Dietrich. 2000. Pretransitional effects in dimyristoylphosphatidylcholine vesicle membranes: Optical dynamometry study. *Biophysical Journal* 79 (1): 340-56.

Dimova, R., and R Lipowsky. 2012. Lipid membranes in contact with aqueous phases of polymer solutions. *Soft Matter* 8 : 6409-15.

Dimova, R., S. Aranda, N. Bezlyepkina, V. Nikolov, K.A. Riske, and R. Lipowsky. 2006; 2006. A practical guide to giant vesicles. probing the membrane nanoregime via optical microscopy. *Journal of Physics: Condensed Matter* 18 (28): S1151-76.

Dimova, R., U. Seifert, B. Pouligny, S. Forster, and H.-G. Dobereiner. 2002. Hyperviscous diblock copolymer vesicles. *Eur.Phys.J.E* 7 (3) (mar,): 241-50, 10.1140/epje/i200101032; http://dx.doi.org/10.1140/epje/i200101032.

Dobereiner, H. -G, E. Evans, M. Kraus, U. Seifert, and and M. Wortis. 1997. Mapping vesicle shapes into a phase diagram: A comparison of experiment and theory. *Physical Review E* 55 (4): 4458-74.

Dobereiner, H. -G, J. Kas, D. Noppl, I. Sprenger, and E. Sackmann. 1993. Budding and fission of vesicles. *Biophysical Journal* 65 (4): 1396-403.

Dopico, Alex M. 2007. *Methods in membrane lipids*. Totowa, N.J.: Humana Press.

Ebert, S., K. Travis, B. Lincoln, and J. Guck. 2007. Fluorescence ratio thermometry in a microfluidic dual-beam laser trap. *Optics Express* 15 (23): 15493-9.

Ekpenyong, A. E., C.L. Posey, J.L. Chaput, A.K. Burkart, M.M. Marquardt, T.J. Smith, and M.G. Nichols. 2009. Determination of cell elasticity through hybrid ray optics and continuum mechanics modeling of cell deformation in the optical stretcher. *Applied Optics* 48 (32): 6344-54.

Eriksson, E., K. Sott, F. Lundqvist, M. Sveningsson, J. Scrimgeour, D. Hanstorp, M. Goksor, and A. Graneli. 2010. A microfluidic device for reversible environmental changes around single cells using optical tweezers for cell selection and positioning. *Lab on a Chip* 10 (5): 617-25.

Evans, E., and D. Needham. 1987. Physical properties of surfactant bilayer membranes: Thermal transitions, elasticity, rigidity, cohesion, and colloidal interactions. *J. Phys. Chem* 91 (16): 4219-28.

Fowles, G. R., and G.L. Cassidy. 2005. *Analytical mechanics*. 5th ed. Belmont, CA: Brooks/Cole.

Fygenson, D. K., J.F. Marko, and A. Libchaber. 1997. Mechanics of microtubule-based membrane extension. *Physical Review Letters* 79 (22): 4497-500.

Gompper G. and M. Schick. 2008. *Soft Matter: Lipid Bilayers and Red Blood Cells*, Vol. 4. Weinheim: Wiley-VCH. p. 206-210.

Gordon, R., M. Kawano, J.T. Blakely, and D. Sinton. 2008. Optohydrodynamic theory of particles in a dual-beam optical trap. *Physical Review B* 77 (24): 245125-1-5.

Grover, S. C., A.G. Skirtach, R.C. Gauthier, and C.P. Grover. 2001. Automated single-cell sorting system based on optical trapping. *Journal of Biomedical Optics* 6 (1) (Jan): 14-22.

Guck, J., S. Schinkinger, B. Lincoln, F. Wottawah, S. Ebert, M. Romeyke, D. Lenz, H.M. Erickson, R. Ananthakrishnan, D. Mitchell, J. Kas, S. Ulvick, and C. Bilby. 2005. Optical deformability as an inherent cell marker for testing malignant transformation and metastatic competence. *Biophysical Journal* 88 (5): 3689.

Guck, J., R. Ananthakrishnan, H. Mahmood, T.J. Moon, C.C. Cunningham, and J. Kas. 2001. The optical stretcher: A novel laser tool to micromanipulate cells. *Biophysical Journal* 81 (2): 767-84.

Guck, J., R. Ananthakrishnan, T.J. Moon, C.C. Cunningham, and J. Kas. 2000. Optical deformability of soft biological dielectrics. *Physical Review Letters* 84 (23): 5451-4.

Harland, C.W., M.J. Bradley, and R. Parthasarathy. 2010. Phospholipid bilayers are viscoelastic. *PNAS* 107 (45): 19146-19150.

Haswell, E. S., R. Phillips, and D.C. Rees. 2011. Mechanosensitive channels: What can they do and how do they do it? *Structure* 19 (10): 1356-69.

Hecht, E. 2002. *Optics*. 4th ed. San Francisco: Pearson Addison Wesley.

Henon, S., G. Lenormand, A. Richert, and F. Gallet. 1999. A new determination of the shear modulus of the human erythrocyte membrane using optical tweezers. *Biophysical Journal* 76 (2): 1145-51.

Hirst, L. S., P. Uppamoochikkal, and C. Lor. 2011. Phase separation and critical phenomena in biomimetic ternary lipid mixtures. *Liquid Crystals* 38 (11-12): 1735-47.

Huibers, P. D. T. 1997. Models for the wavelength dependence of the index of refraction of water. *Applied Optics* 36 (16): 3785-7.

Ichikawa, M., and K. Yoshikawa. 2001. Optical transport of a single cell-sized liposome. *Applied Physics Letters* 79 (27): 4598-600.

Irvine, W. M. 1965. Light scattering by spherical particles: Radiation pressure, asymmetry factor, and extinction cross section. *Journal of the Optical Society of America* 55 (1): 16-21.

Jess, P. R. T., V. Garces-Chavez, A.C. Riches, C.S. Herrington, and K. Dholakia. 2007. Simultaneous raman micro-spectroscopy of optically trapped and stacked cells. *Journal of Raman Spectroscopy* 38 (9): 1082-8.

Jess, P. R. T., V. Garces-Chavez, D. Smith, M. Mazilu, L. Paterson, A. Riches, C.S. Herrington, W. Sibbett, and K. Dholakia. 2006. Dual beam fibre trap for raman micro-spectroscopy of single cells. *Optics Express* 14 (12): 5779-91.

Jonasz, M., and G.R. Fournier. 2007. Light scattering by particles in water: Theoretical and experimental foundations. Amsterdam: Elsevier, Inc.

Kawano, M., J.T. Blakely, R. Gordon, and D. Sinton. 2008. Theory of dielectric micro-sphere dynamics in a dual-beam optical trap *Optics Express* 16 (13) (Jun 23): 9306-17.

Kim, C. -B, and C.B. Su. 2004. Measurement of the refractive index of liquids at 1.3 and 1.5 microns using a fibre optic fresnel ratio meter. *Meas. Sci. and Technol.* 15 : 1683-6.

Kreysing, M. K., T. Kiebling, A. Fritsch, C. Dietrich, J.R. Guck, and J.A. Kas. 2008. The optical cell rotator. *Optics Express* 16 (21): 16984-92.

Kuhl, T., Y. Guo, J.L. Alderfer, A.D. Berman, D. Leckband, J. Israelachvili, and S.W. Hui. 1996. Direct measurement of polyethylene glycol induced depletion attraction between lipid bilayers. *Langmuir* 12 (12): 3003-14.

Lautenschlager, F. 2011. Cell compliance: Cytoskeletal origin and importance for cellular function. Doctor of Philosophy., University of Cambridge.

Lautenschlager, F., S. Paschke, S. Schinkinger, A. Bruel, M. Beil, and J. Guck. 2009. The regulatory role of cell mechanics for migration of differentiating myeloid cells. *Pnas* 106 (37): 15696-701.

Lee, B. K., and T. H. Kwon. 2010. A novel monolithic fabrication method for a plastic microfluidic chip with liquid interconnecting ports. *J. Micromech. Microeng.* 20 : 105004-1-11.

Lee, H. J., E.L. Peterson, R. Phillips, W.S. Klug, and P.A. Wiggins. 2008. Membrane shape as a reporter for applied forces. *Pnas* 105 (49) (12-09): 19253-7, http://www.pnas.org.

Levine, A.J. and F.C. MacKintosh. 2002. Dynamics of viscoelastic membranes. *Phys Rev E*. 66: 061606-1-13.

Li, Y., R. Lipowsky, and R. Dimova. 2011. Membrane nanotubes induced by aqueous phase separation and stabilized by spontaneous curvature. *Pnas* 108 (12): 4731-6.

Lincoln, B., F. Wottawah, S. Schinkinger, S. Ebert, and J. Guck. 2007. High-throughput rheological measurements with an optical stretcher. In *Cell mechanics.*, eds. Y-L Wang, D.E. Discher. Vol. 83, 397-423Academic Press.

Lincoln, B., S. Schinkinger, K. Travis, F. Wottawah, S. Ebert, F. Sauer, and J. Guck. 2007. Reconfigurable microfluidic integration of a dual-beam laser trap with biomedical applications *Biomedical Microdevices* 9 (5) (Oct): 703-10.

Lincoln, B., H.M. Erickson, S. Schinkinger, F. Wottawah, D. Mitchell, S. Ulvick, C. Bilby, and J. Guck. 2004. Deformability-based flow cytometery. *Cytometry Part A* 59 (2): 203-9.

Lipowsky, R. 1991. The conformation of membranes. *Nature* 349 : 475-81.

Luisi, P. L. 2000. Why giant vesicles? In *Giant vesicles.*, eds. P. L. Luisi, P. Walde, 3-6. Chichester; New York: John Wiley & Sons.

Lulevich, V., T. Zink, H.Y. Chen, F.T. Liu, and G.Y. Liu. 2006. Cell mechanics using atomic force microscopy-based single-cell compression. *Langmuir* 22 (19): 8151-5.

Markvoort, A. J., R.A. van Santen, and P.A.J. Hilbers. 2006. Vesicle shapes from molecular dynamics simulations. *J. Phys. Chem. B.* 110 (45): 22780-5.

Matzler, C. 2002. MATLAB functions for mie scattering and absorption. *IAP Research Report, Institut Fur Angewandte Physik, Universitaat Bern* 2002-08 & -11, .

McMahon, H. T., and J.L. Gallop. 2005. Membrane curvature and mechanisms of dynamic cell membrane remodelling. *Nature* 438 : 590-6.

McNeil, G. T. 1977. Metrical fundamentals of underwater lens system. *Optical Engineering* 16 (2): 128-39.

Menger, F. M., and J.S. Keiper. 1998. Giant vesicles: Micromanipulation of membrane bilayers. *Advanced Materials* 10 (11): 888-90.

Miao, L., U. Seifert, M. Wortis, and H.-G. Dobereiner. 1994. Budding transitions of fluid-bilayer vesicles: The effect of area-difference elasticity. *Physical Review E* 49 (6): 5389-410.

Mirsaidov, U., W. Timp, K. Timp, M. Mir, P. Matsudaira, and G. Timp. 2008. Optimal optical trap for bacterial viability. *Physical Review E* 78 (2 Pt 1): 021910-1-7.

Money, NP. 1989. Osmotic pressure of aqueous polyethylene glycols. *Plant Physiol.* 91 : 766-9.

Nawaz, S., P. Sanchez, K. Bodensiek, S. Li, M. Simons, and I.A.T. Schaap. 2012. Cell visco-elasticity measured with AFM and optical trapping at sub-micrometer deformations. *Plos One* 7 (9): 1-9.

Needham, D., D. Zhelev, and H-G Dobereiner. 2000. Physical properties. In *Giant vesicles.*, eds. P. L. Luisi, P. Walde, 101-149. Chichester; New York: John Wiley & Sons.

Neuman, K. C., E.H. Chadd, G.F. Liou, K. Bergman, and S.M. Block. 1999. Characterization of photodamage to *escherichia coli* in optical traps. *Biophysical Journal* 77 (5): 2856-63.

Phillips, R., T. Ursell, P. Wiggins, and P. Sens. 2009. Emerging roles for lipids in shaping membrane-protein function. *Nature* 459 : 379-85.

Pinon, T. 2009. Dual-beam optical fiber trapping platform for biophotonics applications. Master of Science., University of California, Merced.

Pinon, T., L.S. Hirst, and J.E. Sharping. 2012. Optical trapping and stretching of lipid vesicles. Paper presented at CLEO: Applications and Technology, Optical Society of America (OSA) Technical Digest (Online), Cellular Imaging & Therapy (ATh1M), San Jose, CA.

Pinon, T. M., A.R. Castelli, J.E. Sharping, and L.S. Hirst. 2012, in revision. A fiber-optic trap-on-a-chip platform for probing low refractive index contrast biomaterials. *Applied Optics*.

Pinon, T. M., L.S. Hirst, and J.E. Sharping. 2011. Fiber-based dual-beam optical trapping system for studying lipid vesicle mechanics. Paper presented at Optical Society of America, Trapping techniques and applications II (OTTuB), Monterey, CA.

Polysciences Inc. Poly(ethylene glycol) MW8000; pharma grade data sheet. [cited 02/25/2013]. Available from http://www.polysciences.com/Catalog/Department/Product/98/categoryId__289/PageIndex__2/productId__857/.

Popescu, G., T. Ikeda, K. Goda, C.A. Best-Popescu, M.Laposata, S. Manley, R.R. Dasari, K. Badizadegan, and M.S. Feld. 2006. Optical measurement of cell membrane tension. *Physical Review Letters* 97 (21): 218101-1-3.

PubChem. Glucose [cited 01/26/2013]. Available from http://pubchem.ncbi.nlm.nih.gov/summary/summary.cgi?cid=5793&loc=ec_rcs

Quan, X., and E.S. Fry. 1995. Empirical equation for the index of refraction of seawater. *Applied Optics* 34 (18): 3477-80.

Rancourt-Grenier, S., M.-T. Wei, J.-J. Bai, A. Chiou, P.P. Bareil, P.-L. Duval, and Y. Sheng. 2010. Dynamic deformation of red blood cell in dual-trap optical tweezers. *Optics Express* 18 (10): 10462-72.

Rawicz, W., K.C. Olbrich, T. McIntosh, D. Needham, and E. Evans. 2000. Effect of chain length and unsaturation on elasticity of lipid bilayers. *Biophysical Journal* 79 (1): 328-39.

Reeves, D., T. Ursell, P. Sens, J. Kondev, and R. Phillips. 2008. Membrane mechanics as a probe of ion-channel gating mechanisms. *Phys Rev E Stat Nonlin Soft Matter Phys* 78 (4 Pt 1): 041901-1-22.

Remmerbach, T. W., F. Wottawah, J. Dietrich, B. Lincoln, C. Wittekind, and J. Guck. 2009. Oral cancer diagnosis by mechanical phenotyping. *Cancer Res* 69 (5): 1728-32.

Rheims, J., J. Koser, and T. Wriedt. 1997. Refractive-index measurements in the near-IR using an abbe refractomater. *Meas. Sci. Technol.* 8 : 601-5.

Sainov, S., Y. Sarov, and S. Kurtev. 2003. Wide-spectral-range laser refractometer. *Applied Optics* 42 (13): 2327-8.

Seifert, U. 1997. Configurations of fluid membranes and vesicles. In *Advances in physics.* 46th ed., 13-137.

Sens, P., L. Johannes, and P. Bassereau. 2008. Biophysical approaches to protein-induced membrane deformations in trafficking. *Current Opinion in Cell Biology* 20 (4) (8): 476-82.

Shah, G. A. 1991. Asymmetry parameter and efficiency for radiation pressure and scattering of electromagnetic radiation by a very large dielectric sphere. In *Astrophysics and space science.* Vol. 178, 251-260Kluwer Academic Publishers.

Shitamichi Y., M. Ichikawa, and Y. Kimura. 2009. Mechanical properties of giant liposome studied using optical tweezers. *Chem. Phys. Lett.* 479 (4-6): 274-8.

Sidick, E., S.D. Collins, and A. Knoesen. 1997. Trapping forces in a multiple-beam fiber-optic trap. *Applied Optics* 36 (25): 6423-33.

Sigma Aldrich. Polyethylene glycol solution [cited 01/26 2013]. Available from: http://www.sigmaaldrich.com/catalog/product/sigma/76293?lang=en&region=US.

Skelton, S. E., M. Sergides, G. Memoli, O.M. Marago, and P.H. Jones. 2012. Optical squeezing of microbubbles: Ray optics and mie scattering calculations. Paper presented at Proc. SPIE: Optical Trapping and Optical Micromanipulation IX, 84581F, San Diego, CA.

Skelton, S.E.;M. Sergides;G. Memoli;O.M. Marago;P.H. Jones. 2012. Trapping and deformation of microbubbles in a dual-beam fibre-optic trap. *Journal of Optics* 14 (7): 1-10.

Sleep, J., D. Wilson, R. Simmons, and W. Gratzer. 1999. Elasticity of the red cell membrane and its relation to hemolytic disorders: An optical tweezers study. *Biophysical Journal* 77 (6): 3085-95.

Solmaz, M. E., R. Biswas, S. Sankhagowit, J.R. Thompson, C.A. Mejia, N. Malmstadt, and M.L. Povinelli. 2012. Optical stretching of giant unilamellar vesicles with an integrated dual-beam optical trap. *Biomedical Optics Express* 3 (10): 2419-27.

Sosa-Martinez, H. and J.C. Gutierrez-Vega. 2009. Optical forces on a Mie spheroidal particle arbitrarily oriented in a counterpropagating trap. *J. Opt. Soc. Am. B.* 26(11): 2109-2116.

Stanley, C. B., and H.H. Strey. 2003. Measuring osmotic pressure of poly(ethylene glycol) solutions by sedimentation equilibrium ultracentrifugation. *Macromolecules* 36 (18): 6888-93.

Svetina, S., and B. Zeks. 2002. Shape behavior of lipid vesicles as the basis of some cellular processes. *The Anatomical Record* 268 (3): 215-25.

Tasso, I.V. and G.C. Buscaglia. 2013. A finite element method for viscous membranes. *Comput. Methods Appl. Mech. Eng* 255:226-237.

Thomas, M. E. 2006. Optical propagation in linear media: Atmospheric gases and particles, solid-state components, and water, eds. J. R. Apel, K. Moorjani. New York, New York: Oxford University Press, Inc.

Titushkin, I., and M. Cho. 2007. Modulation of cellular mechanics during osteogenic differentiation of human mesenchymal stem cells. *Biophysical Journal* 93 (10): 3693-702.

Van de Hulst, H. C. 1981. *Light scattering by small particles*. Mineola, NY: Dover.

Vennemann, N., M.D. Lechner, and R.C. Oberthur. 1987. Thermodynamics and conformation of polyoxyethylene in aqueous solution under high pressure: 1. small-angle neutron scattering and densitometric measurements at room temperature. *Polymer* 28 (10): 1738-48.

Voet, D., J.G. Voet, and C.W. Pratt. 2006. *Fundamentals of biochemistry : Life at the molecular level*. New York: Wiley.

Wetzel, F., S. Ronicke, K. Muller, M. Gyger, D. Rose, M. Zink, and J. Kas. 2011. Single cell viability and impact of heating by laser absorption. *Eur. Biophys J* 40 (9): 1109-14.

Yuan, J., S.M. Hira, G.F. Strouse, and L.S. Hirst. 2008. Lipid bilayer discs and banded tubules: Photoinduced lipid sorting in ternary mixtures. *J. Am. Chem. Soc.* 130 (6): 2067-72.

Yunus, W. M., and A.B. Rahman. 1988. Refractive index of solutions at high concentrations. *Applied Optics* 27 (16): 3341-3.